146 pages

IN-43

IN-14301

JPL PUBLICATION 86-10



# Shuttle Imaging Radar Views the Earth From Challenger: The SIR-B Experiment

J. P. Ford
J. B. Cimino
B. Holt
M. R. Ruzek

March 15, 1986

NASA
National Aeronautics and
Space Administration

Jet Propulsion Laboratory
California Institute of Technology
Pasadena, California

# Shuttle Imaging Radar Views the Earth from Challenger: the SIR-B Experiment

***Overleaf: Hand-held photograph of the Space Shuttle Challenger's payload bay, taken in orbit by the crew of Mission 41-G; hardware elements of the SIR-B experiment are in the foreground.***

*Two crew members, Kathryn Sullivan (A SIR-B coinvestigator) and David Leestma are shown at the end of the bay as they performed an experiment during extra-vehicular activity (EVA). During that EVA, the astronauts made certain there was no physical impediment to proper deployment and latching of the SIR-B antenna. The SIR-B components that appear in this photograph are identified in Figure 5.*

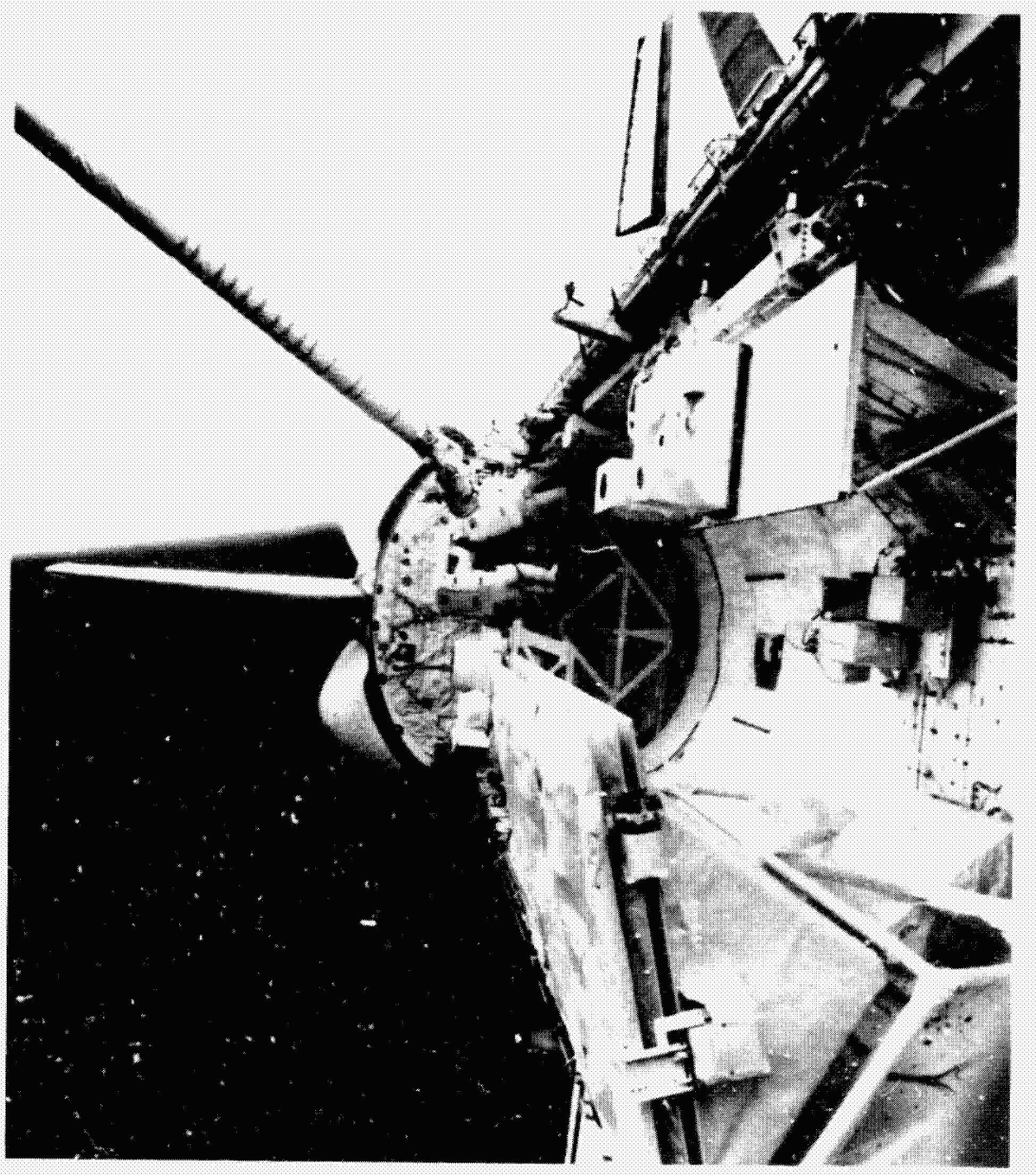

JPL PUBLICATION 86-10

# Shuttle Imaging Radar Views the Earth From Challenger: The SIR-B Experiment

J. P. Ford
J. B. Cimino
B. Holt
M. R. Ruzek

March 15, 1986

National Aeronautics and
Space Administration

**Jet Propulsion Laboratory**
California Institute of Technology
Pasadena, California

The research described in this publication was carried out by the Jet Propulsion Laboratory, California Institute of Technology, under contract with the National Aeronautics and Space Administration.

# Foreword

On October 5, 1984, the second Shuttle Imaging Radar, SIR-B, was launched into orbit aboard the Space Shuttle Challenger. SIR-B is the third step in an evolving NASA program to use spaceborne imaging radar techniques for Earth and planetary exploration. Previous spaceborne imaging radar missions by SIR-A (1981) and Seasat SAR (1978) were equipped with fixed imaging geometries. The principal difference between SIR-B and these two radars was the ability of SIR-B to image selected Earth targets at a number of different incidence angles and to acquire the data in a digital format. Mechanical tilting of the SIR-B antenna provided the means to obtain such multiple-incidence-angle coverage on successive days of the mission.

Approximately 7 hours of digitally recorded data were acquired by SIR-B over about 6.5 million $km^2$ of the Earth's surface. Multiple-incidence-angle coverage of tropical terrains, mountainous regions, and vegetated lowlands were obtained for the first time. This represents a pioneering use of spaceborne radar systems for Earth observations. It is enabling investigators to study the relations between radar backscatter and incidence angle quantitatively through a range of different terrain types and surface covers. SIR-B stereoscopic radar measurements have provided an experimental basis for all-weather topographic mapping from space that is commensurate in accuracy with existing photogrammetric techniques.

Investigations of the SIR-B data include studies in the areas of geology and cartography, hydrology, vegetation, and oceanography. Applications of the data to such studies are illustrated in this atlas of 40 selected SIR-B images. The images are accompanied by diverse types of interpretive information that include multiple SIR-B coverage, computer-generated perspective views, sketch maps and diagrams, or corresponding coverage obtained by remote sensors using different wavelengths at different times.

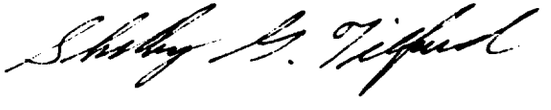

Shelby G. Tilford
Director
Earth Science and Applications Division
Office of Space Science and Applications, NASA

# Acknowledgments

The authors acknowledge the numerous people who contributed to the SIR-B experiment and who helped in the preparation of this atlas. Thanks are expressed to E. Caro, B. Huneycutt, and others of the engineering team that successfully developed and flew the SIR-B sensor. We acknowledge H. Harris, M. Bergam, and their mission design team, and S. Wall and members of the JPL mission operations team. Digital data processing was provided by J. Curlander and his group. We are grateful to C. LeVine who processed the color images and A. Holmes who assisted in providing us with SIR-B image products. Special thanks are expressed to the editor, D. Fulton, and to M. F. Buehler, R. Chandler, T. Kiriyama, and members of the Documentation Section. Assistance provided by numerous individuals including many SIR-B Science Team members in analyzing and interpreting the images is individually acknowledged where appropriate at the scene captions. Particular thanks are expressed for the support of NASA Headquarters, and specially to S. Tilford (Director, Earth Science and Applications Division), M. Settle (Program Scientist on OSTA-3), and R. Monson (Program Manager).

# Abstract

In October 1984, SIR-B obtained digital image data of about 6.5 million $km^2$ of the Earth's surface. The coverage is mostly of selected experimental test sites located between latitudes 60 deg north and 60 deg south. Programmed adjustments made to the look angle of the steerable radar antenna and to the flight attitude of the shuttle during the mission permitted collection of multiple-incidence-angle coverage or extended mapping coverage as required for the experiments. The SIR-B images included here are representative of the coverage obtained for scientific studies in geology, cartography, hydrology, vegetation cover, and oceanography. The relations between radar backscatter and incidence angle for discriminating various types of surfaces, and the use of multiple-incidence-angle SIR-B images for stereo measurement and viewing, are illustrated with examples. Interpretation of the images is facilitated by corresponding images or photographs obtained by different sensors, or by sketch maps or diagrams.

PRECEDING PAGE BLANK-NOT FILMED

# Contents



PRECEDING PAGE BLANK NOT FILMED

# I. Introduction

The Shuttle Imaging Radar B (SIR-B) was launched into orbit aboard the Space Shuttle Challenger on October 5, 1984. SIR-B acquired digital radar image coverage of varied terrains and ocean surfaces through—for the first time—a range of different incidence angles. Approximately 7 h of digital data covering about 6.5 million km$^2$ of the Earth's surface were obtained between latitudes 60 deg north and 60 deg south. The coverage is shown in Figure 1.

SIR-B is the third experiment in NASA's evolving series of spaceborne imaging radar studies. The experiments are part of a continuing program to develop the scientific capability and technology necessary for a spaceborne multifrequency multipolarization radar with variable imaging geometry, a radar that will fly an extended 10-year mission on the polar platform component of a space station called the Earth Observing System (EOS).

The program began in June 1978 with the launch of Seasat. This free-flying Earth-orbiting satellite included a synthetic-aperture radar (SAR) system. The SAR was designed specifically to image the ocean from a nearly polar orbit (Beal et al., 1981; Fu and Holt, 1982; Vesecky and Stewart, 1982). It operated at L-band (23.5-cm wavelength) with horizontal parallel polarization and a fixed look angle of 20 deg. This look angle was chosen to provide the highest sensitivity to subtle changes of slope on the ocean's surface. The swath width was 100 km and the spatial resolution was 25 m. Significant coverage of land surfaces was obtained as well (Elachi, 1980; Ford et al., 1980).

Seasat failed unexpectedly in October 1978 after a short lifetime of about 3-1/3 months. Nevertheless, Seasat provided the first synoptic radar images of the Earth's surface. It was a technological success, and the radar images provided a new means of studying and observing the Earth's surface.

Space-shuttle orbiters provided a new platform for advanced imaging radar systems. These radars could be built more economically than satellites and flown on short proof-of-concept missions, then returned to Earth for upgrading to more technologically advanced systems.

In 1981, SIR-A was launched aboard the second shuttle flight (Cimino and Elachi, 1982; Elachi et al., 1982; Ford et al., 1983). Much of SIR-A was built from Seasat SAR spare parts; for this reason, SIR-A also operated at L-band with horizontal parallel polarization, but the look angle was fixed at 47 deg. SIR-A obtained data with a swath width of 50 km and a spatial resolution of 40 m. The data were recorded optically on board the shuttle.

The main objective of the SIR-A experiment was to further our understanding of radar signatures of land features. A look angle of 47 deg was selected because this angle provides increased sensitivity to surface roughness and decreased sensitivity to topography. A notable result of the experiment was the imaging of buried river channels in the hyperarid regions of southwest Egypt (McCauley et al., 1982; Elachi et al., 1984). The channels are buried by 1 to 3 m of sand and are not visible on optical images or from the ground.

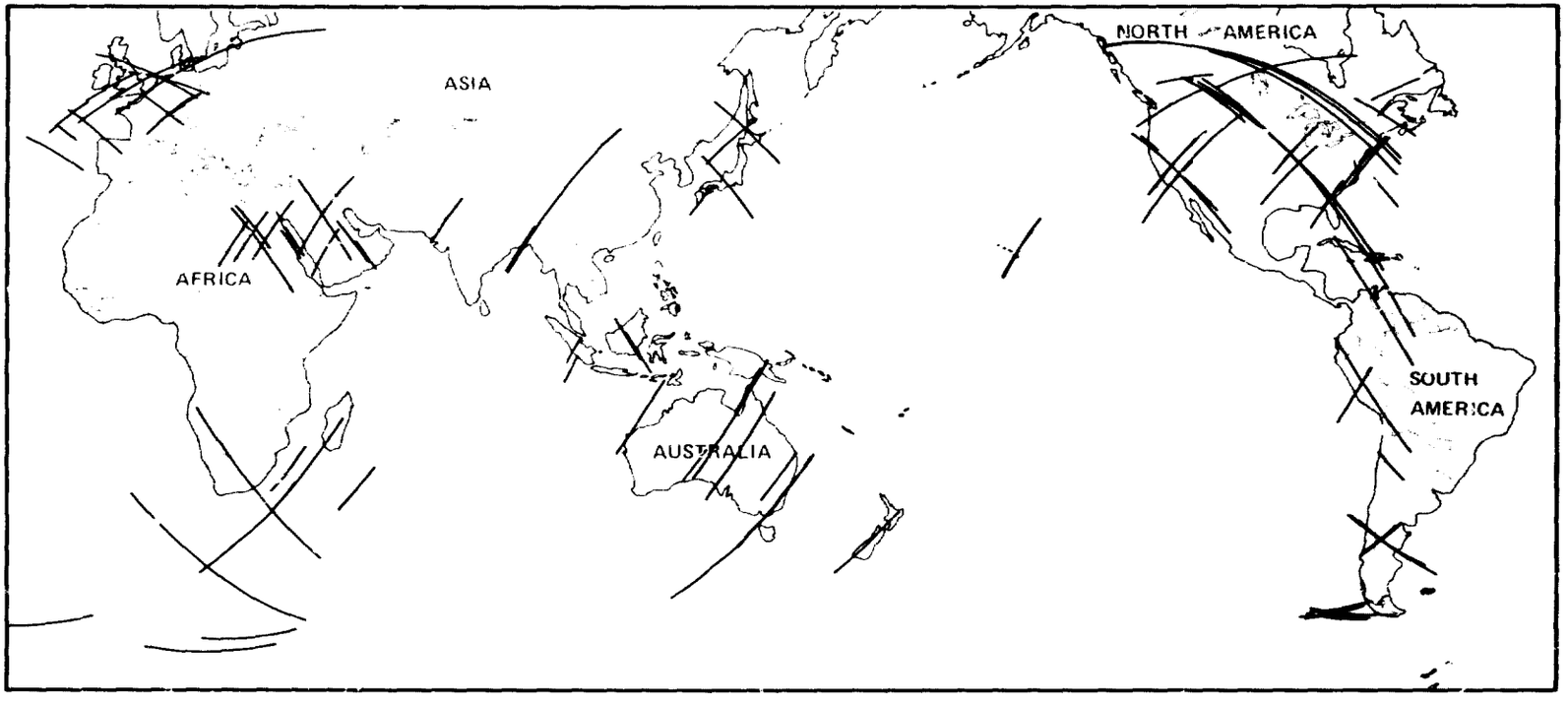


**Figure 1. Areas of SIR-B digital data coverage**

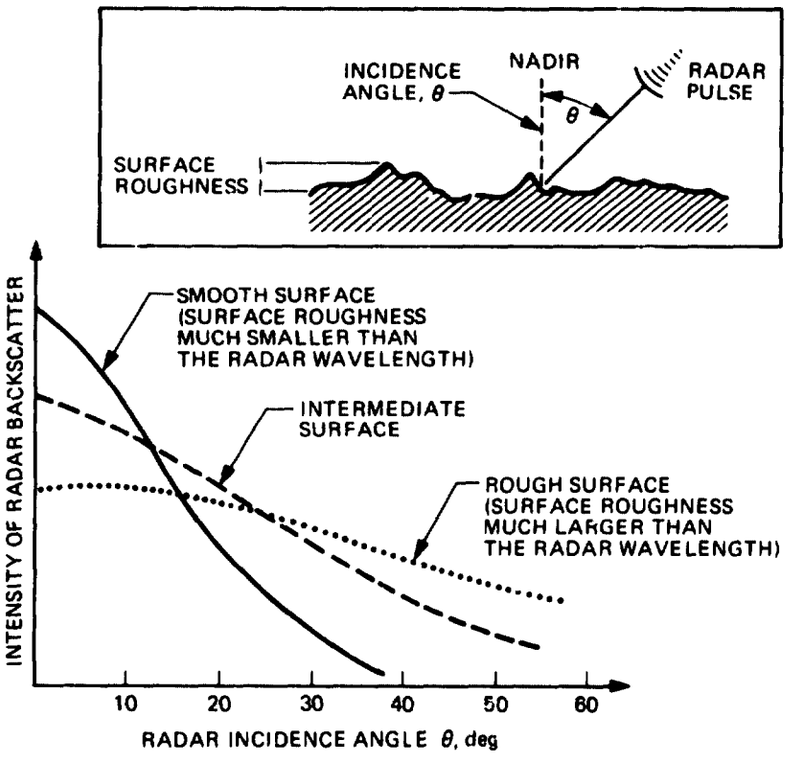


**Figure 2. Radar backscatter as a function of incidence angle**

A comparison of images acquired over the same area by Seasat SAR and by SIR-A shows that backscatter intensity is a function of local incidence angle. In general, backscatter is controlled by topography at lower incidence angles and by small-scale surface roughness at larger incidence angles (Figure 2). The rate at which radar backscatter decreases with increasing incidence angle is governed primarily by the roughness characteristics of the surface. Surfaces that are smooth relative to the wavelength of the radar produce a steep backscatter curve, while surfaces that are relatively rough produce a flatter curve. At incidence angles greater than 30 deg, a rough surface produces a stronger radar return than a smooth surface. This indicates that the backscatter characteristics of different natural surfaces might be used to discriminate different types of terrain (Figure 3).

Spaceborne imaging radars provide perspectives of the Earth's surface that are unique in geoscientific studies (Elachi et al., 1982; Carver et al., 1985). In addition to the radar's ability to penetrate dry surface cover (Blom et al., 1983) and tenuous vegetation layers (Engheta and Elachi, 1982), Seasat SAR and SIR-A data have been particularly useful in structural and morphological mapping because of the strong sensitivity of the radar backscatter to changes in surface slope or roughness (for examples, see Ford, 1980 and 1984; Sabins et al., 1980; Elachi et al., 1981; Sabins, 1983; Wadge and Dixon, 1984).

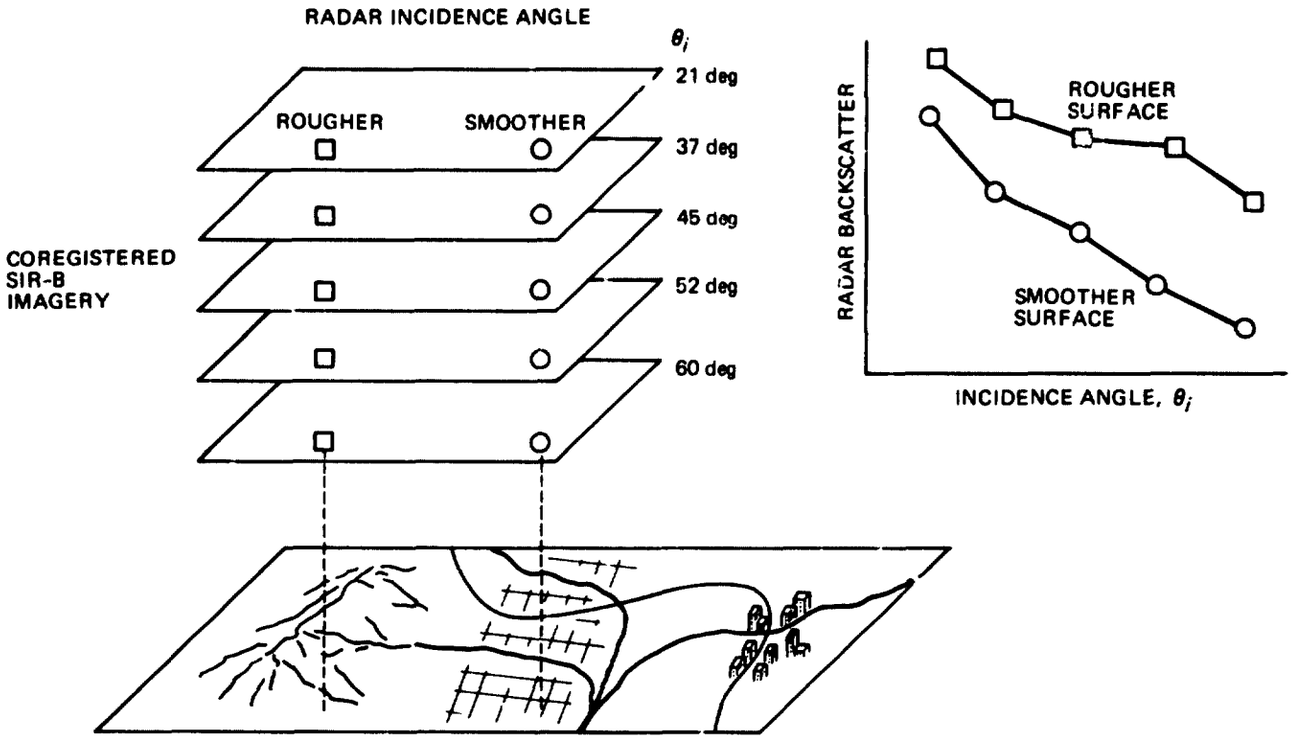


**Figure 3. Surface characterization using backscatter as a function of incidence angle**

# II. SIR-B: The System and the Experiment

Quantifying the backscatter-vs-incidence-angle response of various surfaces was the purpose of the SIR-B experiment (SIR-B Science Plan, 1982; Cimino and Elachi, 1982). Accordingly, the SIR-B antenna was designed for mechanical tilt in one-degree increments over a 15- to 60-deg range of look angles.

To acquire multiple-angle imagery with an orbiting radar, a very specific orbit altitude and orbit drift are necessary. SIR-B was flown in a nominally circular orbit at an inclination of 57 deg. On mission day 3, a 225-km altitude was attained. Because this altitude was slightly above that needed for an exact one-day repeat cycle, the required westward drift was produced. On each successive day, the shuttle flew progressively farther from a specific target, and a larger look angle was required to view the target (Figure 4). The pattern varied with the latitude and longitude of the target relative to the orbit node. This 225-km altitude was maintained to provide multiple-angle imaging capability for the duration of the mission. To obtain images on either side of the shuttle's nadir track, the shuttle was flown in different attitudes.

The orbital drift was also used for stereoscopic imaging. Furthermore, by changing the incidence angle only slightly from day to day, the drifting orbit allowed collection of laterally contiguous images that could be mosaicked to cover a large area for mapping purposes.

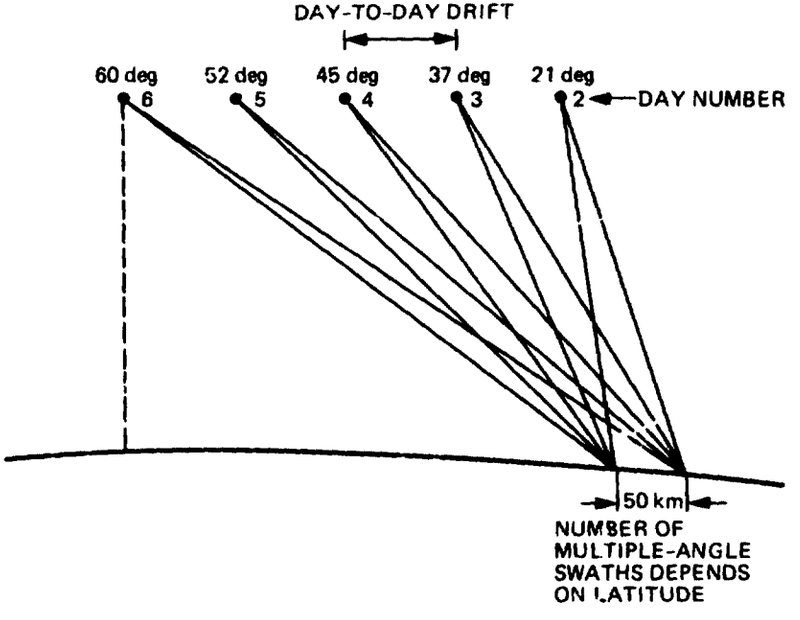


**Figure 4. Orbit drift and multiple-incidence-angle viewing capability**

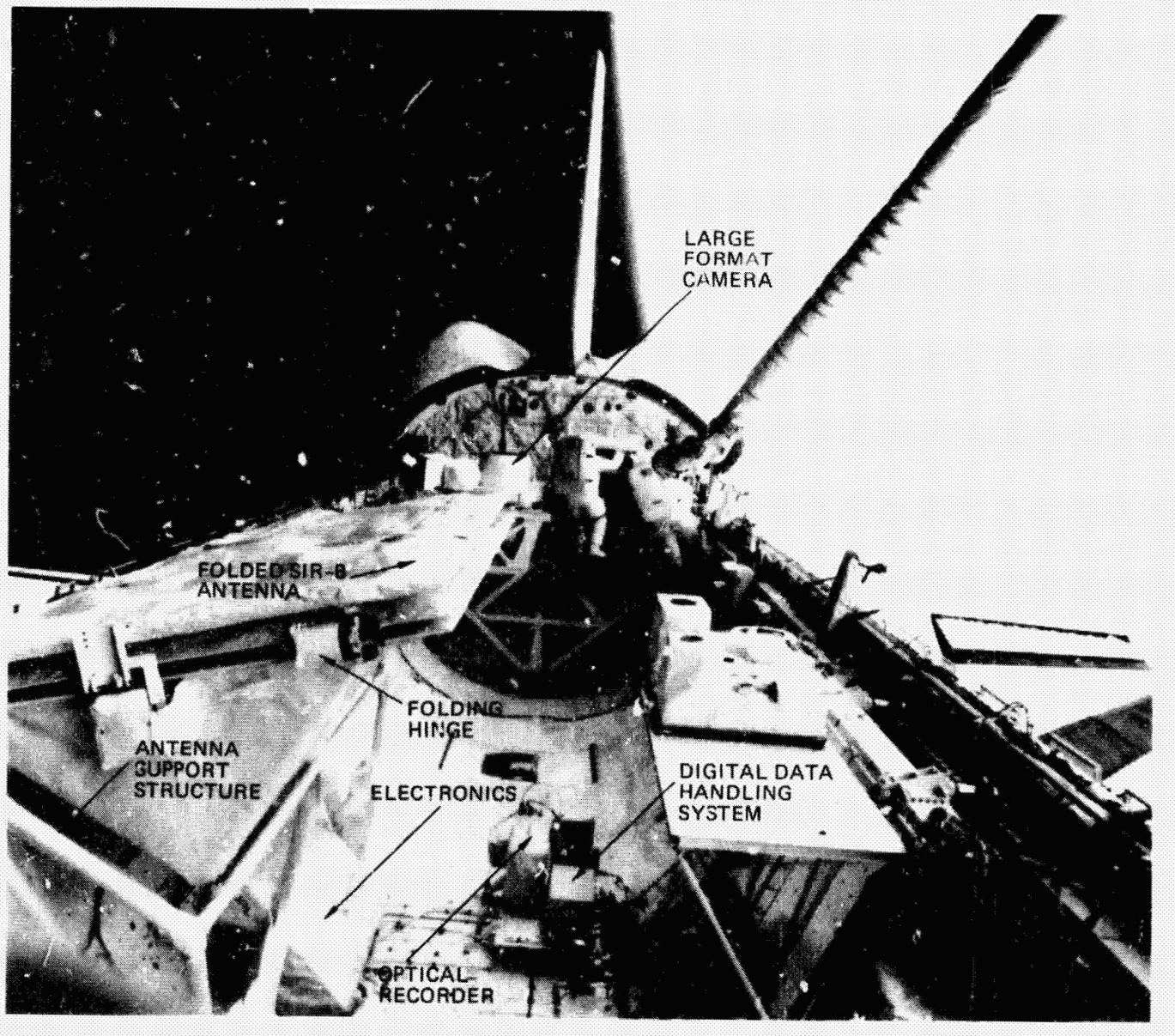


Figure 5. Components of the SIR-B system

Other features of SIR-B included a folding antenna, increased bandwidth, and a digital data system (see Figure 5). The folding antenna provided room in the shuttle payload bay for a deployable satellite—the Earth Radiation Budget Satellite (ERBS), which was lofted into orbit from the shuttle on the first day of the mission. The increased bandwidth improved range resolution by a factor of two. At a 47-deg look angle, resolution improved from 40 m on SIR-A to 20 m on SIR-B.

The digital data capability allowed transmission of data through a Digital Data Handling System (DDHS) on board the shuttle to the Tracking and Data Relay System Satellite (TDRSS) for relay to the ground receiving station at White Sands, New Mexico; these data were transmitted at a rate of 46 Mbits/s. Alternatively, the data were stored on a 30-Mbits/s recorder mounted on the Challenger flight deck for later transmission through the TDRSS to the ground receiving station. The data were then sent via DOMSAT to Goddard Space Flight Center where they were recorded and transmitted to JPL for processing. This digital capability allowed, for the first time, quantitative analytical studies of the illumination effects in radar backscatter. The digital system also provided a dynamic range and spatial resolution that were improved over those of SIR-A.

Two additional features enhanced the flexibility of the SIR-B system and improved the final image product. First, the number of bits per sample was selectable between 3 and 6. Inasmuch as the downlinked data rate was limited to 46 Mbits/s (TDRSS real-time transmission) or 30 Mbits/s (onboard recording), it was possible to select fewer bits per sample to increase the swath width of the image or, alternatively, to select more bits per sample for increased dynamic range with reduced swath width. SIR-B also had an internal radiometric calibrator to allow calibration of data over selected areas. The technical parameters of the SIR-B system are listed and compared with those of the SIR-A and Seasat SAR systems in Table 1.

SIR-B investigations by a team of 43 investigators (Table 2) include studies in the areas of geology, hydrology, vegetation, oceanography, and stereo mapping, as well as investigations on the characteristics of the radar system itself (*The SIR-B Science Investigations Plan*, 1984). Among the investigations are 13 from foreign countries that include Australia, Canada, England, Germany, The Netherlands, New Zealand, and Sweden. Many of the experiments were carried out overseas by U.S. investigators in collaboration with foreign researchers. Collaborative data analyses of this nature were conducted in Argentina, Bangladesh, Botswana, Brazil, Egypt, India, Indonesia, Peru, Saudi Arabia, and Turkey. Two investigations were performed on foreign oceans—one off the coasts of southeast Africa and southwest Chile, and the other in the Southern Ocean. During the mission, members of the SIR-B Science Team were positioned around the world on ships, airplanes, and farms, and in deserts and jungles to collect ground-truth data in support of their experiments.

Technical problems that developed during the mission prevented acquisition of the full image coverage that had been planned. The shuttle's communications antenna, which served to transmit digital data to the TDRSS, lost its drive mechanism; this made it impossible to track the satellite. The problem was partially remedied by disconnecting the pointing control and locking the communications antenna in a fixed position. With the antenna locked, the shuttle was maneuvered into a TDRSS tracking attitude to allow transmission of the digital data to the ground. This new mode of operation required alternate transmission of stored data followed by return of the shuttle to the required attitude for acquisition and onboard digital recording of a further increment of radar data. Under these circumstances, the coverage that could be obtained during the mission was significantly reduced.

Further problems were arcing and power loss in the feed line to the imaging radar antenna. Because of the dynamic range available in the digital data system, it was possible in many instances to boost the gain and partially compensate for this loss of power. In spite of these problems, a large number of SIR-B targets were imaged successfully, and sufficient data were obtained to demonstrate the value of the multiple-angle imaging capability.

**Table 1. Technical parameters of Seasat SAR, SIR-A, and SIR-B**

| Parameter | Seasat SAR | SIR-A | SIR-B |
|---|---|---|---|
| Mission | | | |
| Date | 6/27/78 | 11/12/81 | 10/5/84 |
| Duration | 3-1/3 mo | 2 | 8 days |
| Carrier (mission) | Seasat | Columbia (STS-2) | Challenger (41-G) |
| Orbit | | | |
| Altitude, km | 795 | 259 | 360, 235, and 225 |
| Inclination, deg | 108 | 38 | 57 |
| Radar | | | |
| Frequency, GHz | 1.275 | 1.278 | 1.282 |
| Wavelength, cm | 23.5 | 23.5 | 23.5 |
| System bandwidth, MHz | 19 | 6 | 12 |
| Transmit pulse length, μs | 33.4 | 30.4 | 30.4 |
| Pulse repetition frequency, Hz | 1463–1640 | 1464–1824 | 1248–1824 |
| Transmitted peak power, W | 1000 | 1000 | 1000 |
| Time bandwidth product | 634 | 182 | 364 |
| Polarization | HH | HH | HH |
| Antenna | | | |
| Dimensions, m | 10.74 × 2.16 | 9.4 × 2.16 | 10.74 × 2.16 |
| Look angle, deg | 20 ± 3, fixed | 47 ± 3, fixed | 15–60, mechanically steerable |
| Incidence angle, deg | 23 ± 3 | 50 ± 3 | (15–64) ± 3 |
| Swathwidth, km | 100 | 50 | 20–50 |
| Resolution, m (azimuth × range) | 25 × 25 | 40 × 40 | 25 × (17–58) |
| Data | | | |
| Recording | ground station: digital | onboard: optical | onboard: optical and digital<br>TDRS: digital |
| Signal processing | optical and digital | optical | optical and digital |
| Looks | 4 | 6 | 4 |
| Digital data rate | 110 Mbps (A/D on ground) | – | 30 and 46 Mbps (A/D onboard) |
| Volume, h | 42 (digital) | 8 (optical) | 7 (digital) |
| Coverage (million $km^2$) | 100 | 10 | 6.5 |

**Table 2. SIR-B Science Team members and their investigations**

| Name and affiliation | Investigation |
|---|---|
| **C. Elachi**, SIR-B Team Leader and Principal Investigator<br>Jet Propulsion Laboratory,<br>California Institute of Technology<br>Pasadena, California | |
| **T. Allan**<br>Institute of Oceanographic Sciences<br>Surrey, United Kingdom | "The Interpretation of SIR-B Imagery of Surface Waves and Other Oceanographic Features Using In-Situ, Meteorological Satellite, and Infrared Satellite Data" |
| **W. Alpers**<br>Max-Planck-Institut and Universität Hamburg<br>Federal Republic of Germany | "SAR Imaging Mechanisms of Ocean Surface Waves" |
| **E. P. W. Attema**<br>Delft University of Technology<br>Delft, Netherlands | "ROVE Calibration and Inverse Scattering Experiment" |
| **R. C. Beal**<br>The Johns Hopkins Applied Physics Laboratory<br>Laurel, Maryland | "The Spatial Evolution of the Directional Wave Spectrum in the Southern Ocean: Its Relation to Extreme Waves in the Agulhas Current" |
| **G. L. Berlin**<br>U.S. Geological Survey<br>Flagstaff, Arizona | "Application of SIR-B Data for Groundwater Exploration in the Arabian Shield and Sand-Drift Monitoring in the An Nafud and Al Jafurah Fringe Areas, Kingdom of Saudi Arabia" |
| **A. L. Bloom**<br>Cornell University<br>Ithaca, New York | "Tectonic, Volcanic, and Climatic Geomorphology Study of the Sierras Pampeanas Andes, Northwestern Argentina" |
| **M. L. Bryan**<br>Jet Propulsion Laboratory<br>Pasadena, California | "Deforestation, Floodplain Dynamics, and Carbon Biogeochemistry in the Amazon Basin" |
| **N. L. Bryans**<br>Defence Research Centre Salisbury<br>Adelaide, Australia | "Investigations Involving Corner-Reflector Arrays, Signal Processing, and Oceanographic Studies" |
| **F. Carsey**<br>Jet Propulsion Laboratory<br>Pasadena, California | "Southern Ocean Sea-Ice Morphology and Kinematics" |
| **M. A. Collins**<br>Department of Scientific and Industrial Research<br>Lower Hutt, New Zealand | "New Zealand SIR-B Science Investigations" |

**Table 2 (contd)**

| Name and affiliation | Investigation |
|---|---|
| **T. H. Dixon**<br>Jet Propulsion Laboratory<br>Pasadena, California | "SIR-B Analysis of the Precambrian Shield of Sudan and Egypt: Penetration Studies and Subsurface Mapping" |
| **T. G. Farr**<br>Jet Propulsion Laboratory<br>Pasadena, California | "Quantitative Use of Multiincidence-Angle SAR for Geologic Mapping" |
| **J. P. Ford**<br>Jet Propulsion Laboratory<br>Pasadena, California | "Geologic Mapping of Indonesian Rain Forest With Analysis of Multiple SIR-B Incidence Angles" |
| **N. Fugono**<br>Radio Research Laboratories<br>Tokyo, Japan | "Remote Sensing of Rice Fields and Sea Pollution by SIR-B" |
| **D. Garofalo**<br>Earth Satellite Corporation<br>Chevy Chase, Maryland | "Evaluation of SIR-B Data for Identifying Rainfall Event Occurrence and Intensity" |
| **R. M. Goldstein**<br>Jet Propulsion Laboratory<br>Pasadena, California | "SIR-B Interferometric Topography" |
| **A. L. Gray**<br>Canada Centre for Remote Sensing<br>Ottawa, Canada | "Use of SIR-B Multiincidence-Angle Imagery to Study Iceberg Detectability and Offshore Ocean Feature Extraction" |
| **J. W. Head III**<br>Brown University<br>Providence, Rhode Island | "Geological, Structural, and Geomorphological Analyses From SIR-B" |
| **D. N. Held**<br>Jet Propulsion Laboratory<br>Pasadena, California | "Amplitude Calibration Experiment for SIR-B" |
| **R. M. Hoffer**<br>Purdue University<br>West Lafayette, Indiana | "Microwave and Optical Remote Sensing of Forest Vegetation" |
| **F. R. Honey**<br>Commonwealth Scientific and Industrial Research Organization<br>Wembley, Australia | "Evaluation of SIR-B Imagery for Geologic and Geomorphic Mapping, Hydrology, and Oceanography in Australia" |

**Table 2 (contd)**

| Name and affiliation | Investigation |
|---|---|
| **M. L. Imhoff**<br>Goddard Space Flight Center<br>Greenbelt, Maryland | "The Use of Digital Spaceborne SAR Data for the Delineation of Surface Features Indicative of Malaria Vector Breeding Habits" |
| **W. H. Johnson**<br>University of Illinois<br>Urbana, Illinois | "Interlobate Comparison of Glacial-Depositional Style as Evidenced by Small-Relief Glacial Landscape Features in Illinois, Indiana, and Ohio, Utilizing SIR-B" |
| **V. H. Kaupp**<br>University of Arkansas<br>Fayetteville, Arkansas | "Evaluation of the L-Band Scattering Characteristics of Volcanic Terrain in Aid of Lithologic Identification, Assessment of SIR-B Calibration, and Development of Planetary Geomorphic Analogs" |
| **G. E. Keyte**<br>Royal Aircraft Establishment<br>Farnborough, United Kingdom | "The Investigation of Selected Oceanographic Applications of Spaceborne Synthetic-Aperture Radar" |
| **M. Kobrick**<br>Jet Propulsion Laboratory<br>Pasadena, California | "SIR-B Cartography and Stereo Topographic Mapping" |
| **B. N. Koopmans**<br>International Institute for Aerial Survey and Earth Sciences<br>Enschede, Netherlands | "Monitoring of the Tidal Dynamics of the Dutch Waddensea by SIR-B" |
| **P. D. Lowman, Jr.**<br>Goddard Space Flight Center<br>Greenbelt, Maryland | "Structural Investigation of the Canadian Shield by Orbital Radar and Landsat"<br>"Structural Investigation of the Grenville Province by Radar and Other Imaging and Nonimaging Sensors" |
| **R. K. Moore**<br>University of Kansas Center for Research, Inc.<br>Lawrence, Kansas | "Studies of Coastal Mesoscale Winds Using SIR-B"<br>"Information for Space-Radar Designers: Required Dynamic Range vs Resolution and Antenna Calibration Using the Amazon Rain Forest" |
| **J. F. Paris**<br>Jet Propulsion Laboratory<br>Pasadena, California | "Development and Evaluation of Techniques for Using Combined Microwave and Optical Image Data for Vegetation Studies" |
| **J. T. Parr**<br>The Analytic Sciences Corporation<br>Reading, Massachusetts | "Investigation of SIR-B Images for Lithologic Mapping" |
| **H. K. Ramapriyan**<br>Goddard Space Flight Center<br>Greenbelt, Maryland | "Automatic Terrain Elevation Mapping and Registration" |

**Table 2 (contd)**

| Name and affiliation | Investigation |
|---|---|
| **J. A. Richards**<br>University of New South Wales<br>Kensington, Australia | "Australian Multiexperimental Assessment of SIR-B (AMAS)" |
| **G. G. Schaber**<br>U.S. Geological Survey<br>Flagstaff, Arizona | "Application and Calibration of the Subsurface Mapping Capability of SIR-B in Desert Regions" |
| **A. J. Sieber**<br>Deutsche Forschungs– und Versuchsanstalt für Luft– und Raumfahrt<br>Federal Republic of Germany | "German Radar Observation Shuttle Experiment (ROSE)" |
| **D. S. Simonett**<br>University of California<br>Santa Barbara, California | "The Extension of an Invertible Coniferous Forest Canopy Reflectance Model Using SIR-B and Landsat Data" |
| **E. P. Szuszczewicz**<br>Naval Research Laboratory<br>Washington, D.C. | "An Investigation of Ionospheric Irregularity Effects on SIR-B Image Processing and Information Extraction" |
| **J. V. Taranik**<br>University of Nevada<br>Reno, Nevada | "Analysis of SIR-B Radar Illumination Geometry for Depth of Penetration and Surface Feature and Vegetation Detection, Nevada and California" |
| **M. N. Toksoz**<br>Massachusetts Institute of Technology<br>Cambridge, Massachusetts | "Delineation of Major Geologic Structures in Turkey Using SIR-B Data" |
| **F. T. Ulaby**<br>University of Kansas Center for Research, Inc.<br>Lawrence, Kansas | "Evaluation of the Radar Response to Land Surfaces and Volumes: Examination of Theoretical Models, Target Statistics, and Applications" |
| **E. Ulriksen**<br>Lund University of Technology<br>Lund, Sweden | "Ground Truth for SIR-B Images Obtained by SIR System 8 Impulse Radar" |
| **J. R. Wang**<br>Goddard Space Flight Center<br>Greenbelt, Maryland | "Remote Sensing of Soil Moisture" |
| **R. S. Winokur**<br>Office of Naval Research<br>Arlington, Virginia | "SAR Internal Wave Signature Experiment" |

# III. Interpretation of SIR-B Images

The SIR-B images in this atlas are accompanied by interpretive information that includes sketch maps, diagrams, corresponding images, photographs, and text. In many cases, SIR-B investigators, coinvestigators, and other researchers have verified the interpretation of the images with on-site field studies undertaken before, during, or after the mission. The geographic locations of the scenes are shown in Figure 6. The images are grouped under "Nonrenewable Resources," "Renewable Resources," and "Oceanography." A glossary of technical terms and acronyms relative to the content of this atlas is given in Appendix A. With few exceptions, the SIR-B image of each scene is placed to the left of a corresponding illustration, and oriented so the radar illumination direction is from top to bottom. In this fashion, shadows on the images fall toward the observer and topography does not appear inverted. Serial numbers or other image-identification labels are provided in the "Index of Images" (Appendix B).

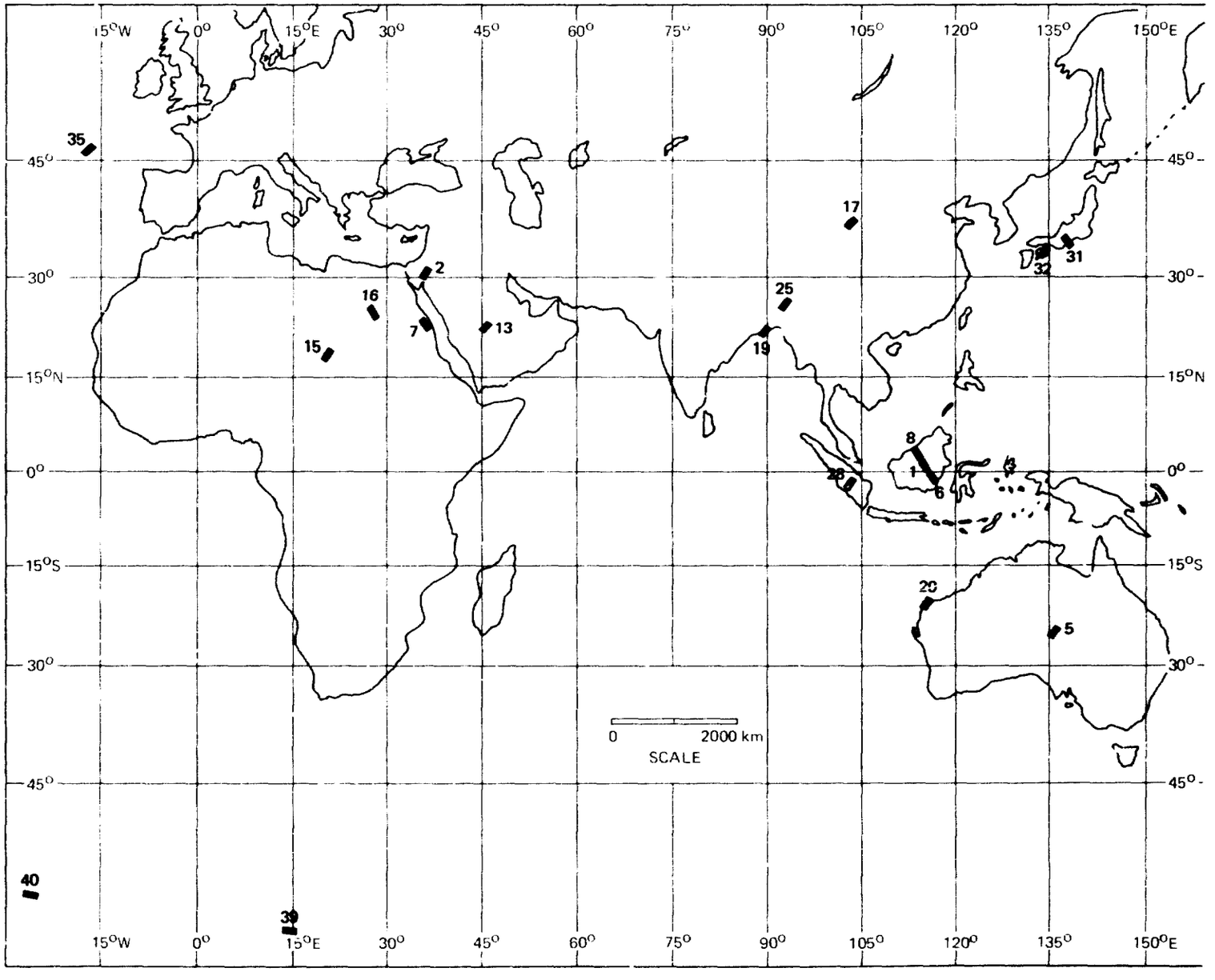
15°W
0°
15°E
30°
45°
60°
75°
90°
105°
120°
135°
150°E
45°
30°
15°N
0°
15°S
30°
45°
35
2
16
7
13
15
17
25
19
31
32
8
1
6
20
5
40
39
0
2000 km
SCALE

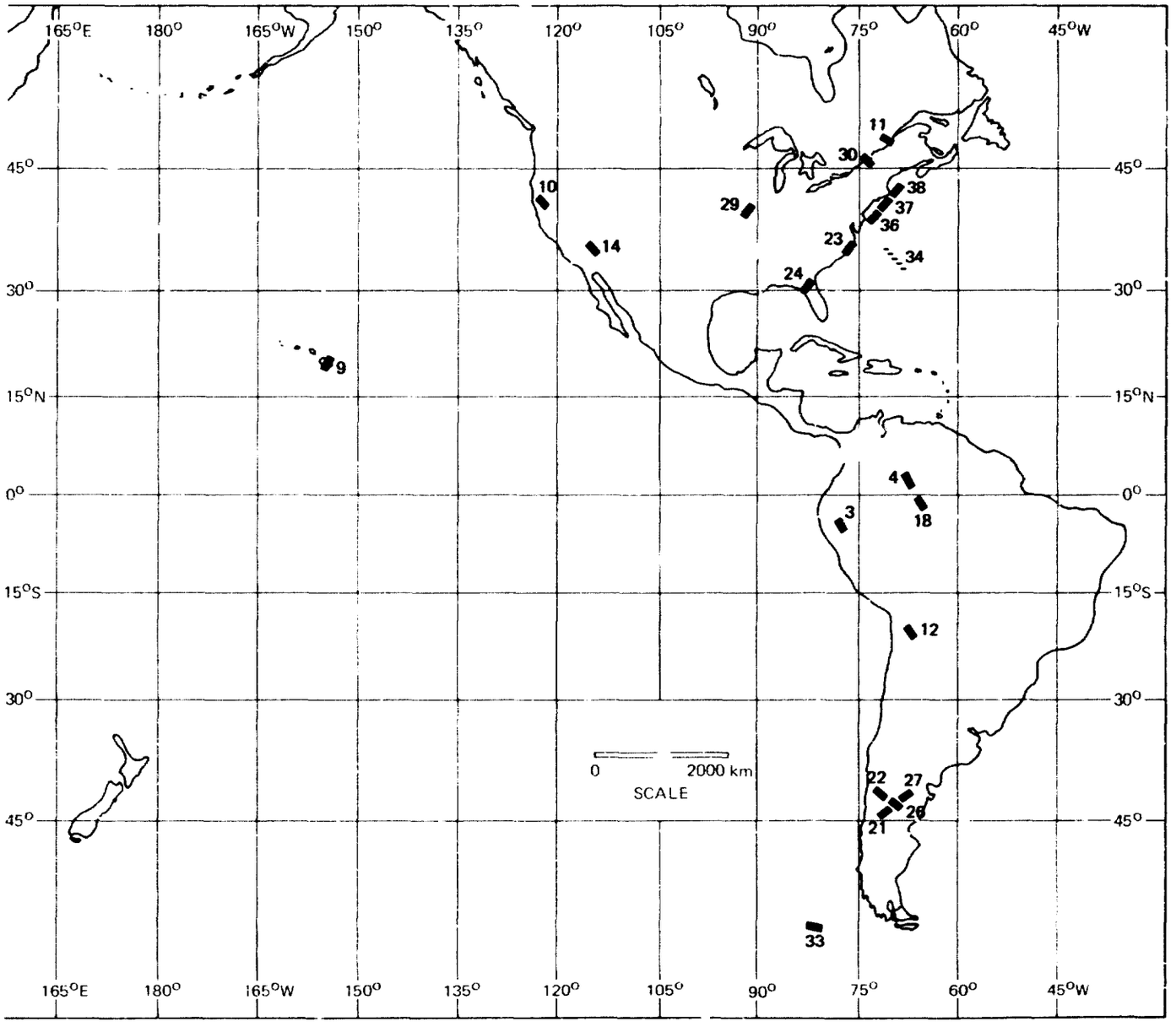


**Figure 6. Geographic locations of SIR-B images**

# A. Nonrenewable Resources

Experiments were designed to assess the capability of multiple-incidence-angle SAR data for lithologic mapping and delineating geologic boundaries of various types. The ability of SIR-B to image targets at different incidence angles on successive days was ideal for a stereo-mapping experiment. Quantifying radar signatures as a function of imaging geometry is of particular interest for geologic mapping in tropical rain forests and for understanding radar penetration relative to surface aridity.

The SIR-B images in this section were obtained at incidence angles from 26 deg to 64 deg. They cover a variety of geologic terrains and environments and provide an opportunity to compare radar backscatter from different surfaces.

## (i) Folded and Layered Structures

**Page intentionally left blank**

## 1. Interior Plateau, Central Kalimantan, Indonesia

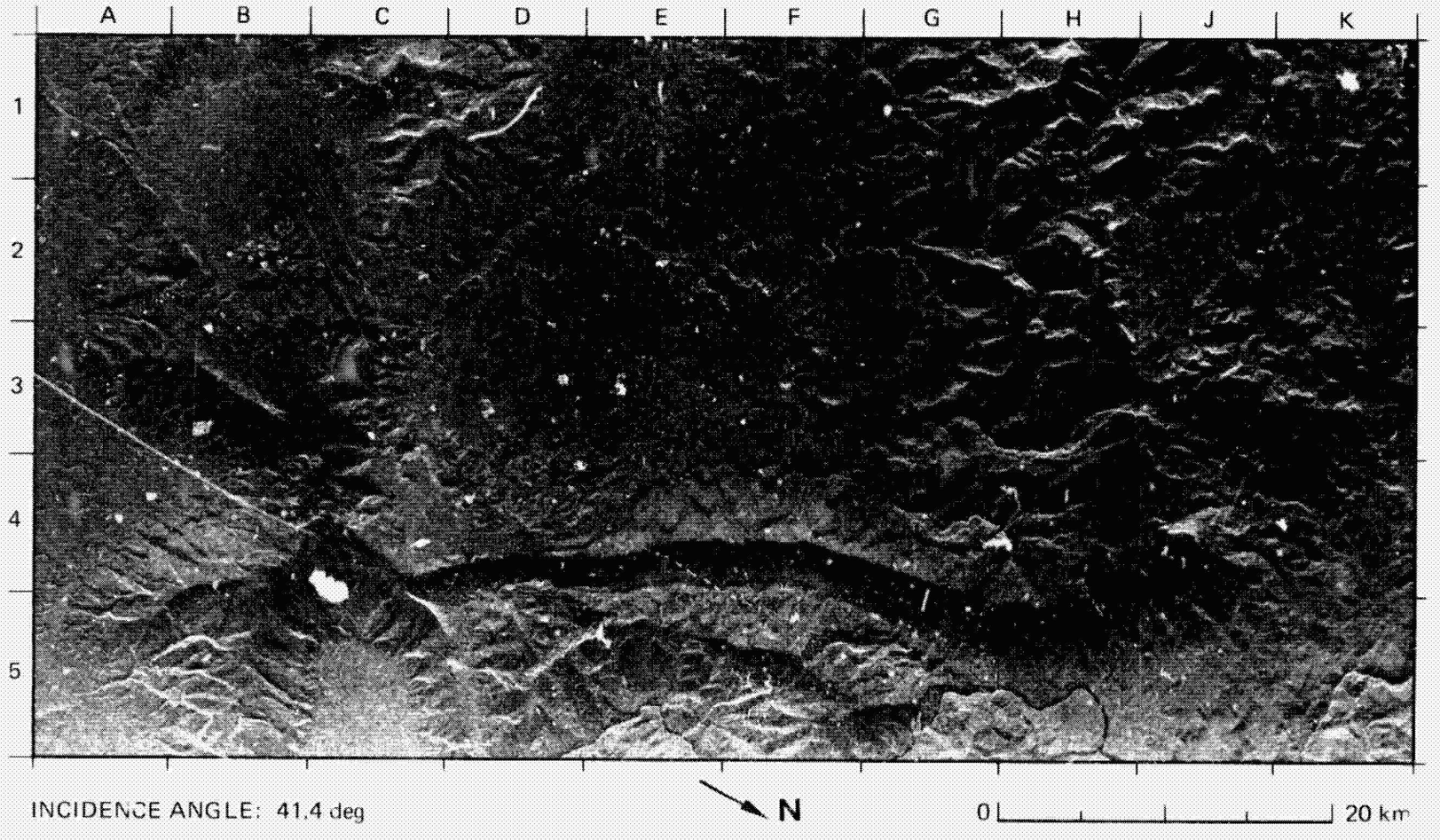

This scene in Central Kalimantan covers the eastern portion of a remote interior plateau and adjacent segments of the Mahakam River valley. The region is densely forested, sparsely inhabited, and largely unmapped. The mean annual rainfall exceeds 4000 mm. Because of the perennial cloud cover, it has not been possible to obtain photographs or optical images for mapping.

The plateau is flanked to the north and east by the Mahakam River and to the southeast by the Ratah River. The surface of the plateau, however, is drained to the southwest by the Murung River and its tributaries, which eventually join the waters of the great Barito River in Central Kalimantan.

The east margin of the plateau extends for 55 km along a steep escarpment from Mr. Batuatau (J4) at about 1650 m to Mt. Tukankole (C4) at about 1000 m elevation. The relief from the north margin of the plateau to the Mahakam River at H5 is approximately 1200 m; relief data for the plateau in general are poorly known, however. Smaller escarpments at higher levels on the plateau are seen from D2 to D4 and from F2 to F3.

The plateau is underlain by Paleogene clastic sedimentary rocks deposited in the Upper Mahakam Basin. Despite very thick forest cover, the dip and strike of the layered rocks beneath the plateau are readily perceived. The dark band along the escarpment from C4 to J4 is a radar shadow cast by thick, extremely steep-sided rim rock. Alternating dark- and light-gray bands in the canyons along the north margin of the plateau from H1 to H4 represent erosion surfaces at different angles of repose—the result of differential resistance of the underlying rocks. The dark bands represent steep slopes formed of the more resistant rocks. The lighter bands denote more gentle slopes formed by weaker rocks.

The outlines of dip slopes and the attitudes of antidip slopes at the southeast margin of the plateau (C3 to C4) reveal a pattern of broadly symmetrical synclines and anticlines. The folds show divergent axes that radiate from the vicinity of Mount Tukankole. The axis of the syncline through the plateau plunges to the southwest and extends considerably beyond the limits of this scene.

The plateau is located between Neogene volcanic terrains in the Mahakam River valley to the north (K1 to K5), and the Ratah River valley to the south, several kilometers beyond the margin of this scene. Each of the volcanic terrains is characterized by numerous small, closely spaced cones. Alluvial gold, presumably derived from the volcanic rocks, is produced in the Mahakam River valley at Longpahangai, beyond the image margin at K4.

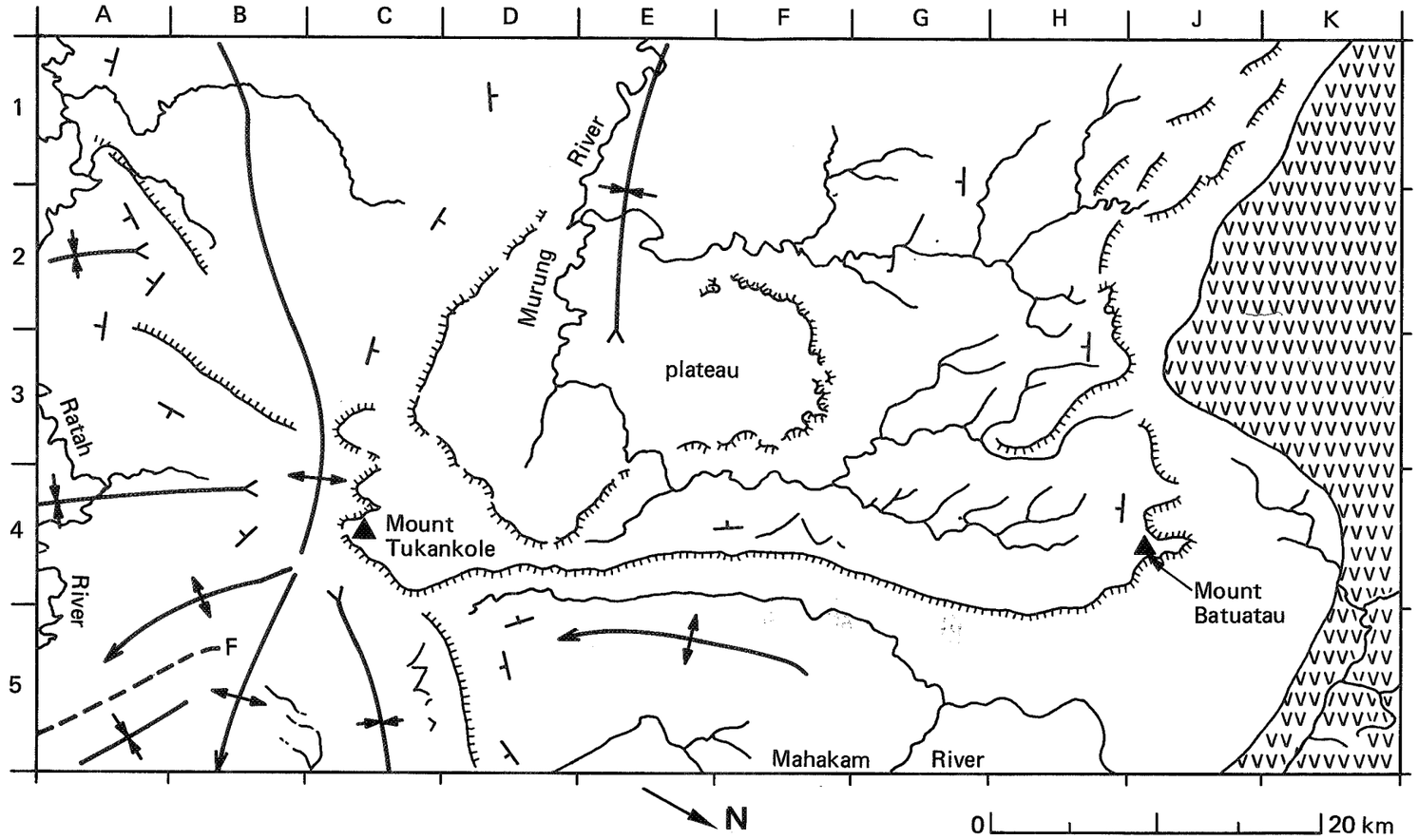


dip and strike of layered rocks

F fault

synclinal axis, with plunge direction

escarpment

anticlinal axis, with plunge direction

volcanic terrain

1 FOLDOUT FRAME

2 FOLDOUT FRAME

## 2. Dead Sea Rift Zone, Southern Israel

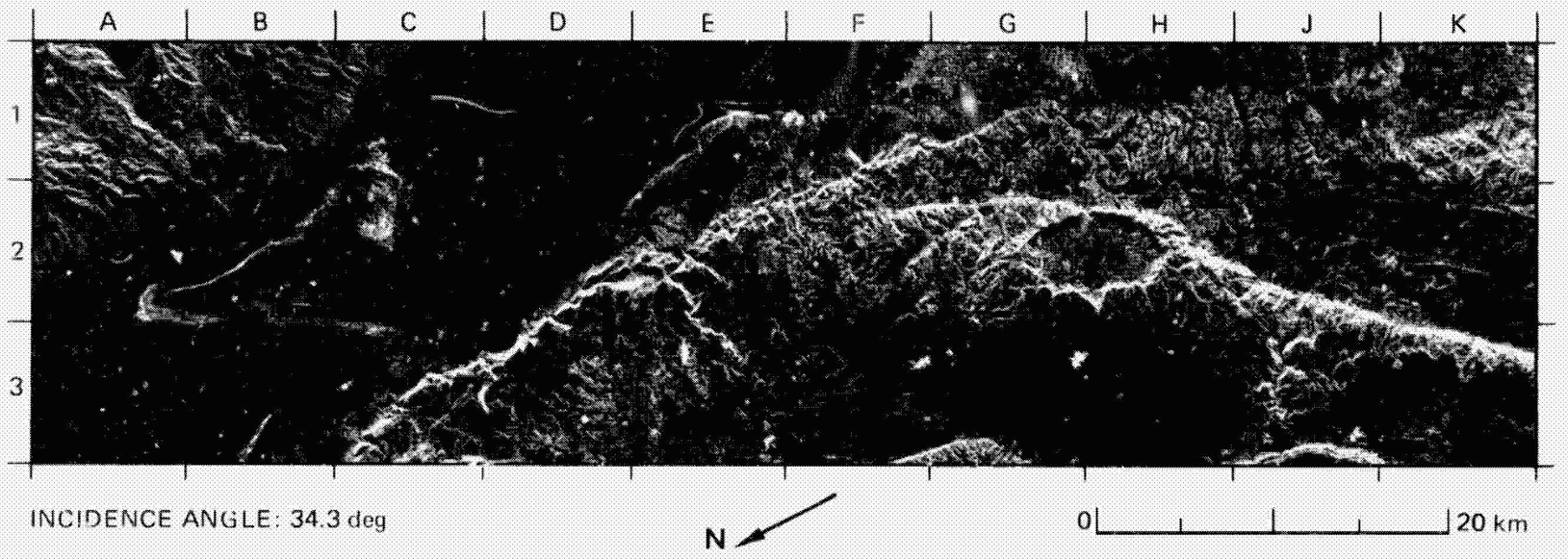




The Dead Sea Rift Zone forms a long linear trough that extends from the Red Sea to Turkey. Its linearity and depth (the bottom of the Dead Sea is 1302 feet below sea level) result from north- and northeast-trending transform faults. These faults accommodate the relative movements and rotations of the Arabian Plate and the microplates of Sinai and the Eastern Mediterranean. Relations between the rift zone, the present suture of the Red Sea, and the Late Precambrian suture line of northeast Sudan are shown on the regional sketch map. Recent geodynamic studies suggest that Precambrian sutures, such as that in northeast Sudan (Image 7), were the antecedents of transform faults that controlled the fragmentation of the Nubian/Arabian Shield and the opening of the Red Sea. It is perhaps significant that this suture in Sudan parallels the Dead Sea Rift Zone.

The sketch map drawn from the SIR-B image shows the transform faults that appear on the image in A1, from A2 to B1, and from C3 to H1. Complementary east-northeast-striking faults of the "Riedel-Shear" type transect the folded platform sediments and form steep scarps—the result of differential uplift. Such a scarp is pronounced on the image from F2 to K3. The eroded dome at G2/H2 clearly shows the dip and strike of bedding structures. Both the dome and the associated basin to the northwest (dark on the image from G3 to J3) are elongated parallel to the fault scarp.

Most of the area covered by the SIR-B image is underlain by limestone and sandy limestone of Upper Cretaceous and Paleocene age. Older rocks are exposed in the eroded dome (G2/H2) and younger fine-grained Neogene terrigenous debris fills the basin at G3 to J3. A small area of karst is visible in K3. The rock types are obscured by strong dissection at the steep margins of the rift zone. Terraces are evident at the margin of the Dead Sea (for example from A2 through B3/C3). The southern part of the Dead Sea has been dammed, and large evaporation pans in the area from C2/D2 to C1 through F1 have been established to produce potash-rich salts.

(The caption, figure, and sketch map were adapted from information provided by courtesy of Dr. Geoff Lawrence, Hunting Geology and Geophysics, Ltd.)

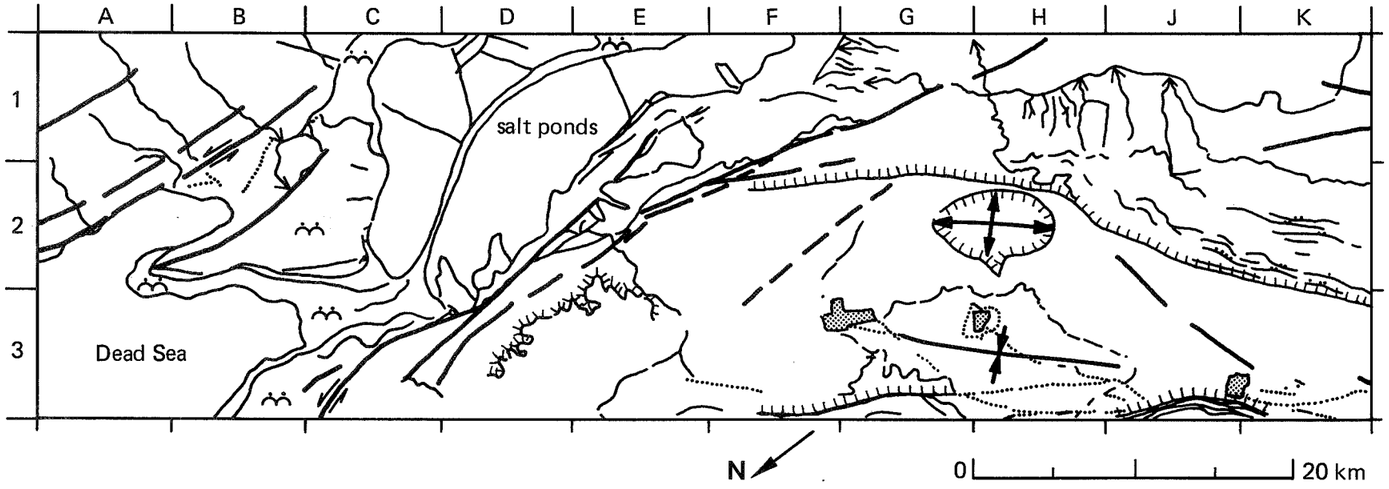


fault, arrows show direction of movement

dome

basin

holocene and recent alluvium

scarp

drainage channel; arrow indicates direction of flow

habitation

road

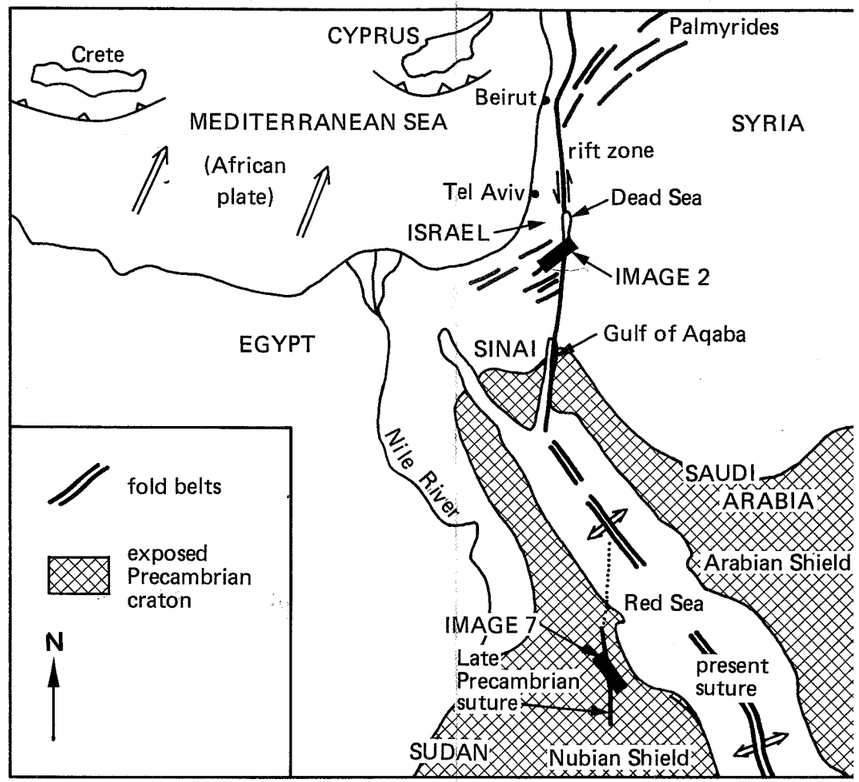

## 3. Central Andean Cordillera, Northern Peru

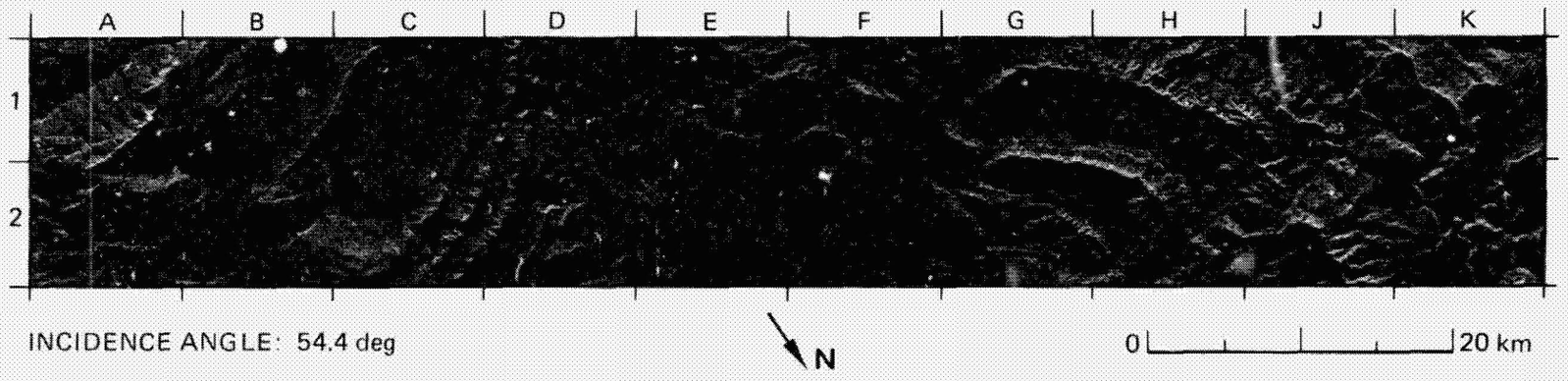


The central Andean Cordillera of northern Peru is in the sub-Andean fold belt to the west of the Amazon platform. Many of the folds are broken and thrust eastward along their more steeply dipping eastern limbs. The strongly folded and thrust-faulted Cretaceous sedimentary rocks that underlie the cordillera are mostly marine shales, sandstones, and limestones. The terrain is rugged and the surfaces are heavily vegetated. The portion of the cordillera covered by this radar image is deeply dissected by the Marañón River and its tributaries. Segments of the Chiriaco River, a major tributary of the Marañón, appear along the top margin of the image from A1 to C1.

The outcrop pattern and the associated flatirons on the image denote moderate to steeply dipping layered rocks in the area from G1 to H1 and from F1 to H2. In this area the mountains display pronounced southwest-facing scarps with dip slopes inclined to the northeast and east. A similar orientation of scarps and dip slopes is seen in the mountains from A2 to B2. Fault traces are evident between the base of the mountains and the Marañón River Valley in the area from F1 to G2. Less deformed rocks are present at lower elevations in the area from J1 through K1 to K2. The dip and strike of the rocks and their outcrop patterns from C1 and D1 to B2 and C2 denote a plunging synclinal structure. The crenulated pattern in the core of the structure at C1 is typical of the hummocky type of karst topography that results from deep chemical weathering in humid tropical areas. The strong discordance between the northwest flank of the fold and the adjacent rocks probably represents the trace of a thrust fault.

The Marañón River is a major tributary of the Amazon drainage several hundred kilometers to the east. It forms an important link between the northeast petroleum-producing province of Loreto and the remainder of Peru. An oil pipeline and a highway that follow this route are seen on the image from D1 to E2. In the upper part of D1, the pipeline and highway take a shortcut over a low mountain pass to rejoin the Marañón near the town of Chiriaco, just off the image. The route is also of historical interest. It is from this locality that the Spanish explorer and conquistador Francisco de Orellana embarked on the first successful river trip to discover the Amazon in 1541.

(This caption was adapted from technical information provided by Professor Arthur L. Bloom of Cornell University.)

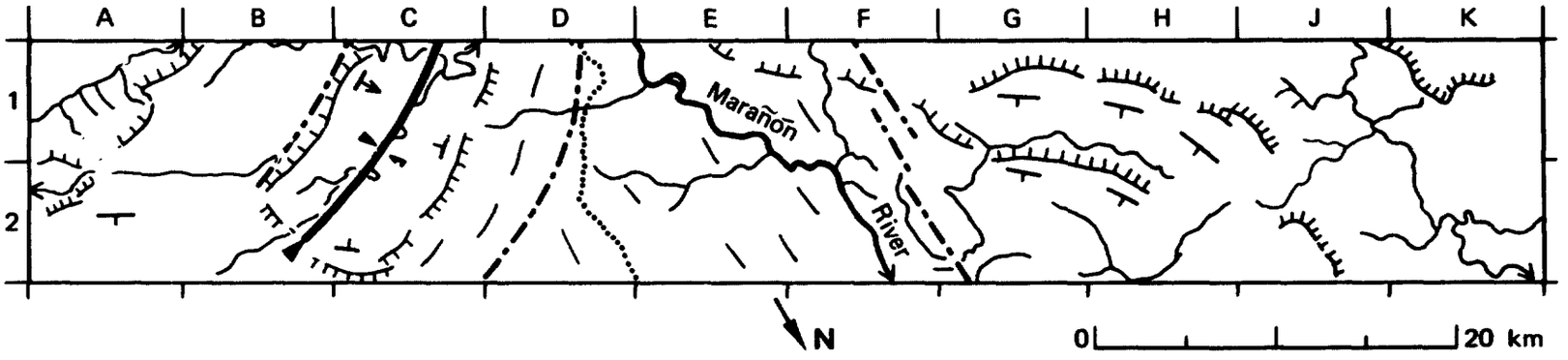


synclinal axis, showing plunge

major fault

escarpment

strike and dip of bedding

routeway; oil pipeline

stream; arrow denotes flow direction

## 6. Precambrian Fold Mountains, Brazil and Colombia

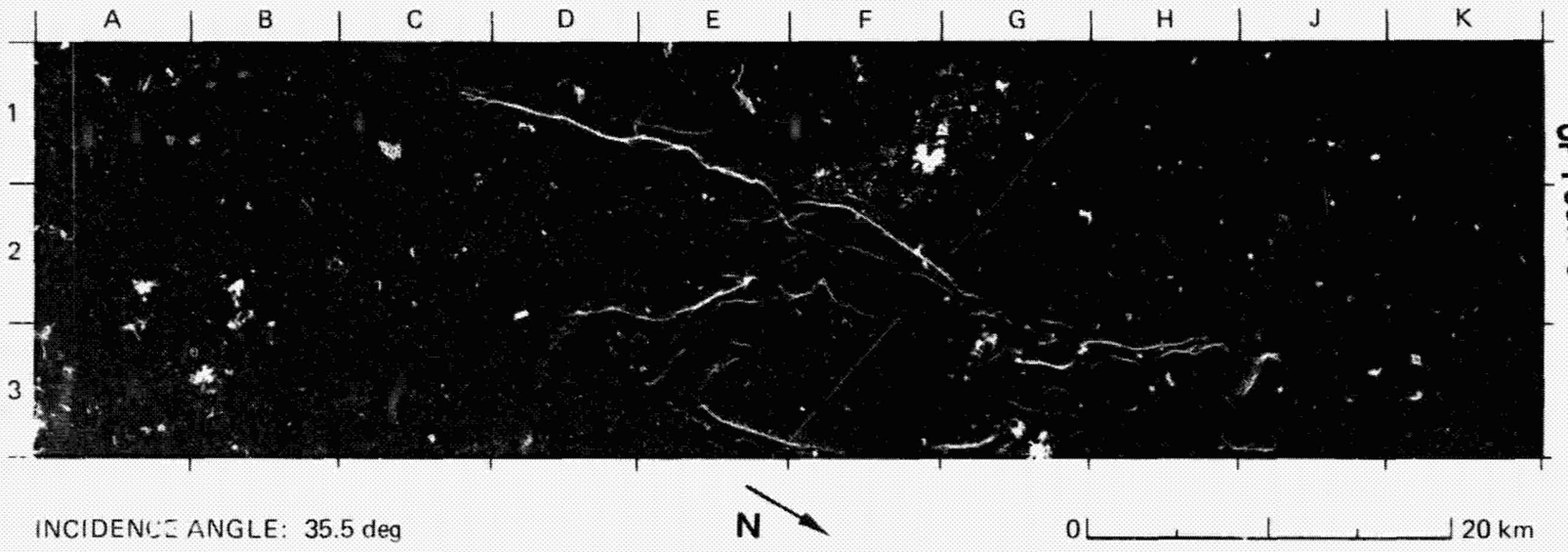




The Amazon Shield in South America is a complex of granite, gneiss, migmatite, and other metamorphic rocks that have undergone several cycles of intense tectonic deformation in early Precambrian (Archean) time. In Brazil, these rocks are referred to the Guiana Complex (Schobbenhaus et al., 1984). In various localities, the Guiana Complex is overlain by sequences of younger Precambrian (Proterozoic) metasedimentary rocks that are folded and locally altered by low-grade metamorphism.

This SIR-B image covers a portion of the Amazon Shield in northwest Brazil and southeast Colombia. It displays a block of low fold mountains that comprises the Serra Caparro (Brazil) from C1 through E2 to D3 and a portion of the Serranía de Naquén (Colombia) from E3 and F2 to J3. The mountains are aligned north-northwest over a distance of about 50 km. They form the drainage divide between north-flowing tributaries of the Río Guainía (Colombia) and south-flowing tributaries of the Rio Cuiari (Brazil). The north margin of the Serra Tunuí, which is a similar elongated block of low fold mountains, is shown at A1.

The rocks in the Serra Caparro are sericite- and muscovite-bearing quartzites that have been referred to the Tunuí Group of Proterozoic age (Pinheiro et al., and references cited therein, 1976). In the Serranía de Naquén, the rocks consist of orthoquartzites that are referred to the upper part of the Roraima Formation. These rocks form Proterozoic erosional remnants believed to lie on a large downfaulted block of the Archean basement, which extends northward beyond this scene (Huguett et al., and references cited therein, 1979).

The mountains rise to about 400 m elevation, and probably 300 m above the level of the surrounding terrain; little detail is known about the relief, however. The area is remote, inaccessible, and covered with a dense heterogeneous forest. At the 35.5-deg incidence angle used in this scene, the geometric compression and tonal saturation of mountain slopes that face toward the radar illumination indicate that the slopes are steep—perhaps 30 deg or more. As a whole, the outcrop patterns and the attitudes of the bedding planes define a series of small anticlines and synclines. The southern part of the Serra Caparro (upper right of C1) is

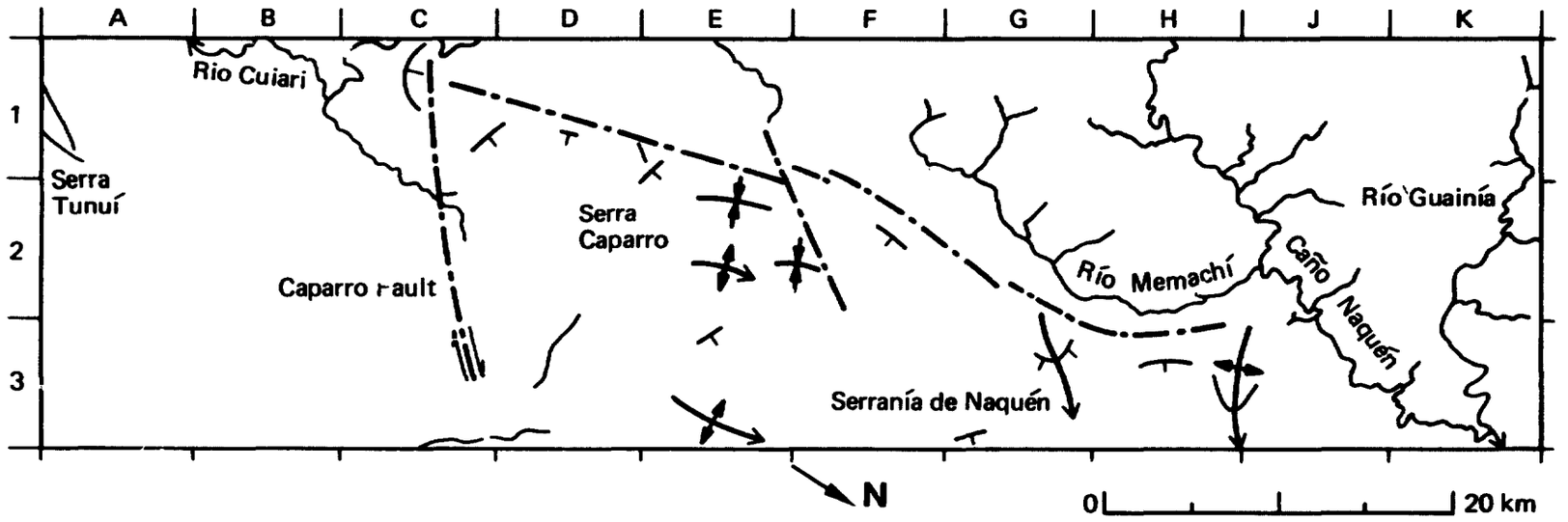


dip and strike

anticlinal axis, with plunge

synclinal axis

major fault; arrows denote relative movements

stream; arrow denotes direction of flow

displaced relative to the northern part (lower right of C1 and following to the north) by the northeast-trending Caparro fault (C1 to C3). This is a right-lateral strike-slip fault whose linear extension beyond the mountain range is scarcely perceptible because it has low relief and is oriented nearly parallel to the direction of illumination.

The forest cover provides a relatively uniform radar backscatter that appears as a monotonous medium gray throughout most of the level areas on the image. Brighter image tones outline portions of the floodplains of some streams, notably on the upper reaches of the Río Memachí (F1/G1 to G2). This probably signifies a change to more open forest above standing water on the floodplain.

(This caption was adapted from information provided by Mr. Fernando Pellon de Miranda, of the Petrobrás Research Center, Rio de Janeiro, Brazil.)

## 5. Amadeus Basin, Northern Territory, Australia

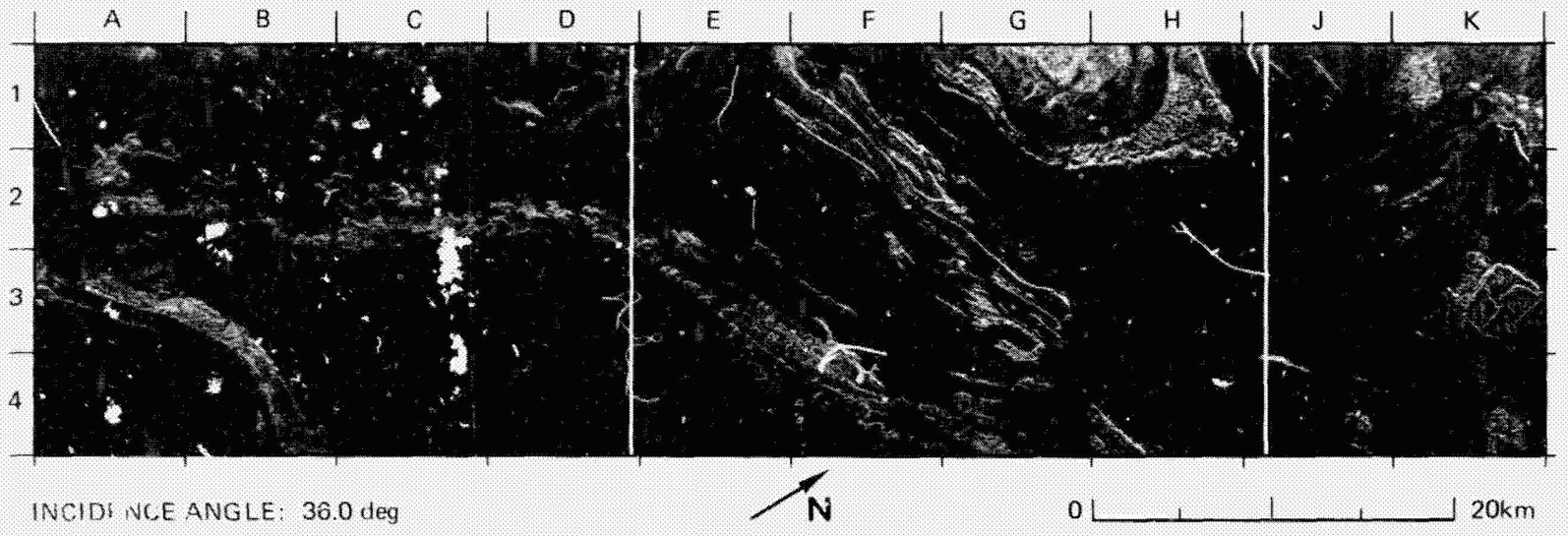


The arid western margin of the Simpson Desert in central Australia is characterized by seif dunes that trend north-northwest and redistributed eolian sands that abut stoney plains, plateaus, and isolated sandstone ranges. The area is underlain by folded and faulted metamorphic and igneous rocks of the Australian Precambrian Shield. Upper Proterozoic, Paleozoic, and Mesozoic marine transgressions deposited sedimentary layers over much of the basin.

Rainfall is extremely erratic – the mean annual average is 16 cm. Heavy rain and flooding occurred immediately prior to the SIR-B overpass, saturating the surface sands and alluvium, and significantly reducing the potential for radar signal penetration. The flora of the test area is typical of that under arid conditions: a variety of drought-resistant species that fix ancient dunes and sparsely cover rock outcrops.

The SIR-B imagery of this basin is of special value in mapping bedding traces and dip directions, which, in turn, allows mapping of several regional geologic features (figure (a)). Dip directions displayed in the image are generally toward the upper right of the image, that is, toward the radar antenna. The extensive dip slopes have bright signatures, and the scarps, which are in the radar shadow, have dark signatures.

Dip directions – interpreted from the radar imagery and confirmed in the field – define a plunging syncline in the upper right and an anticline in the lower center of the image. In the Amadeus SIR-B imagery, most lineaments are expressed as scarps or smaller linear valleys.

The clear expression of topographic characteristics and textural variations due to differing surface roughness conditions on the SIR-B imagery allows recognition of four broad categories of terrain (figure (b)): (1) clastic, which is formed on layered rocks; this terrain is recognized by the topographic expression of resistant strike ridges; (2) carbonate, which has a more subdued outcrop morphology than the clastic rocks and a pitted appearance; (3) eolian, where both dunes and redistributed eolian sands can be recognized by subtle textural differences that arise from variations in surface roughness; and (4) alluvial, which is composed of outwash fans derived from clastic rocks; this terrain can be clearly distinguished by its high backscatter (bright return) derived from characteristically rough surfaces.

A comparison of the maps derived from SIR-B imagery can be made with the published geological map in figure (c) (Ranford et al., 1968).

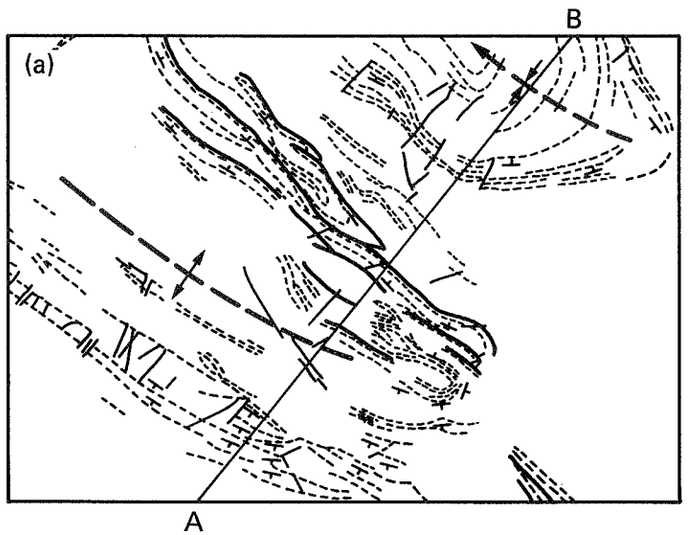


STRUCTURAL FEATURES

- dip and strike
- lineament
- lineament coincident with known fault
- anticline
- syncline, showing plunge
- bedding trends

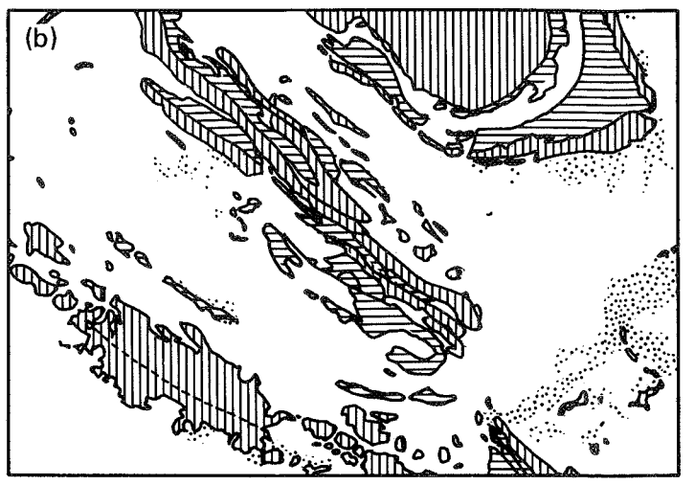


TERRAIN CATEGORIES

- alluvium
- eolian sand
- clastic terrain
- carbonate terrain

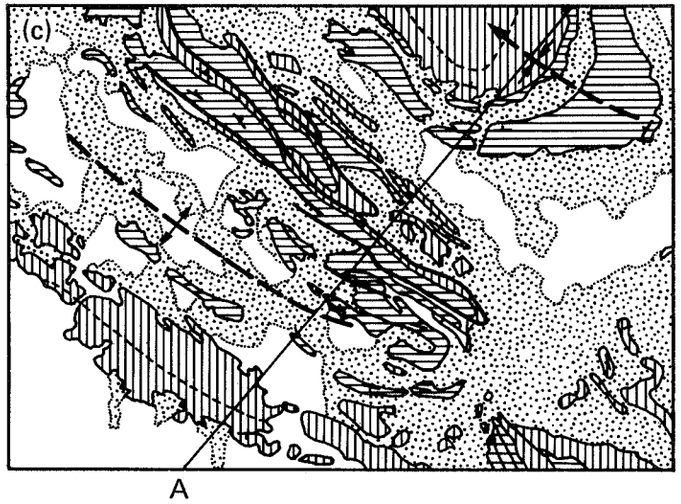


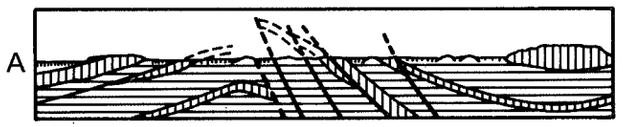


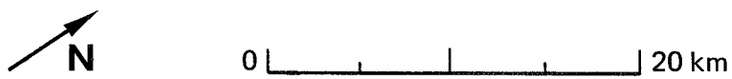


FOLDOUT FRAME 2

FOLDOUT FRAME

## 6. Pasir Mountains and Coastal Lowlands, East Kalimantan, Indonesia

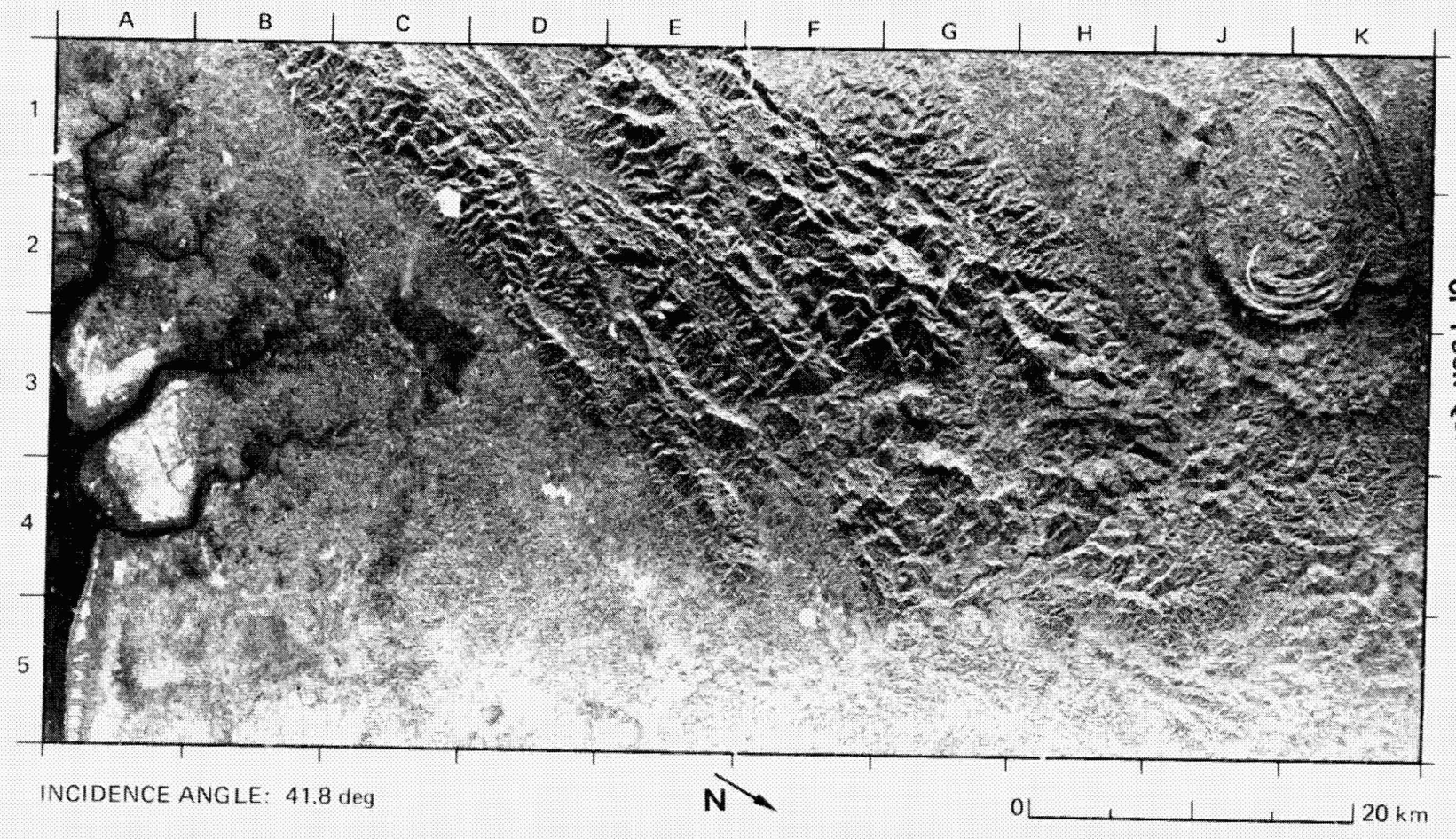




The Pasir Mountains and adjoining coastal lowlands in East Kalimantan are located between the Kutai Basin to the northeast and the Barito Basin to the southwest. The maximum elevation in this scene is slightly over 1200 m at Mt. Lumut (H3); the mountains are underlain by shale, claystone, sandstone, and intercalated limestone of Oligocene to Lower-Miocene age. The rocks are moderately to steeply dipping, with fold axes that generally trend northeast-southwest. The outcrop pattern and trend of the layered rocks are clearly visible on the radar image from C1 to F3. Extensive lineaments across the mountains (for example, from D3 to G3) are probably fault controlled. Small inselbergs at H1/J1 and at the lower margin of G3 suggest discordant relations with the rocks in adjacent areas.

Outcrop patterns in the area from J1/K1 to J2/K2 show a tightly folded, doubly plunging syncline. The northwest margin of this structure is offset by normal faulting. While the dip and strike of the rocks have been mapped locally in the area, the structure itself had not been previously mapped. The pitted texture that appears around the core of the structure is characteristic of deeply weathered limestone terrain in humid tropical areas.

Landsat MSS Band 7

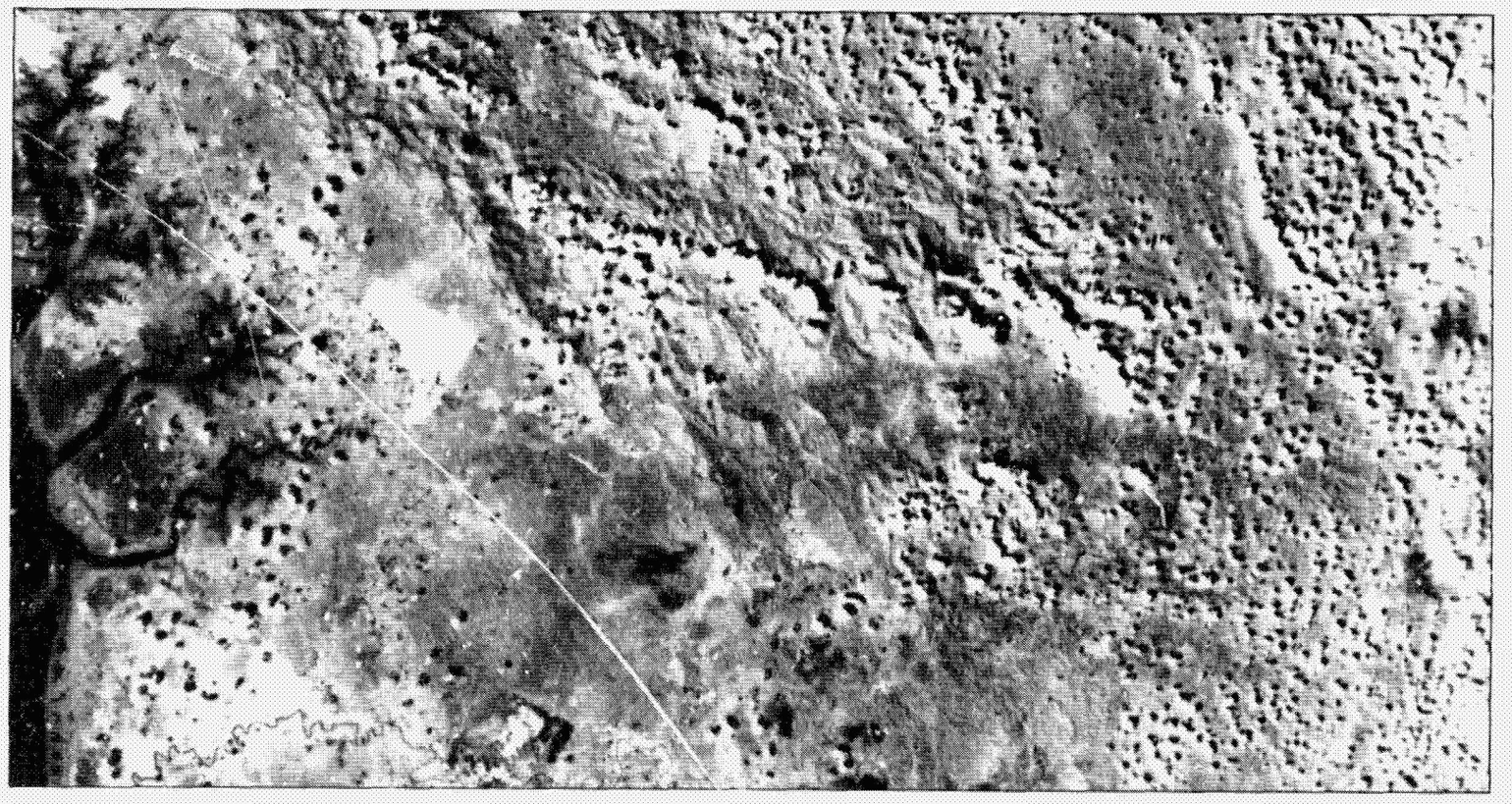



The region is heavily forested, but the coastal lowlands are being progressively cleared for cultivation, as evidenced by regular geometric patterns of deforestation; oil palms provide an important cash crop in these regions. The lands are being cleared also for the resettlement of people from overpopulated areas elsewhere in Indonesia. Newly opened land appears in relatively dark tones as seen in the vicinity of Semantai (B2) and Long Ikis (C3). Longer-established secondary vegetation appears in brighter tones in the vicinity of Long Kali (D5). The Adang (A4 to B4), Semantai (A3 to B3), and Kuaro (A1 to A2) Rivers are flanked by estuarine vegetation that yields medium-gray image tones. Mangroves in the coastal areas from A3 to A5 provide bright image tones.

Corresponding vegetated areas on the Landsat MSS image, which was obtained 14 days after the radar image, appear in inverse tones. The mountains on the Landsat image are largely obscured by cumulus clouds and their shadows.

An oil pipeline follows the sinuous route of a highway that connects communities on the coastal lowlands (A1 to C5). Oil is pumped through this pipeline from producing fields in Tanjung, 85 km to the southwest, to a major refinery at Balikpapan, 50 km to the northeast.

Access to the interior is limited to a few trails and drainage channels, the largest of which is the Telekai River (A1 to H3). A pattern of curvilinear drainages extends from J3 to J4 and K3 to K4.

(This caption was prepared from information provided by Prof. J. Rais of the National Agency for Surveys and Mapping, Cibinong-Bogor, Indonesia, and Dr. R. Sukamto of the Geological Research and Development Centre, Bandung, Indonesia. The Landsat MSS image was provided by Dr. Wiranto Arismunandar of the Indonesian National Institute for Aeronautics and Space.)

## (ii) Linear and Intrusive Structures

## 7. Late Precambrian Suture Line, Northeast Sudan

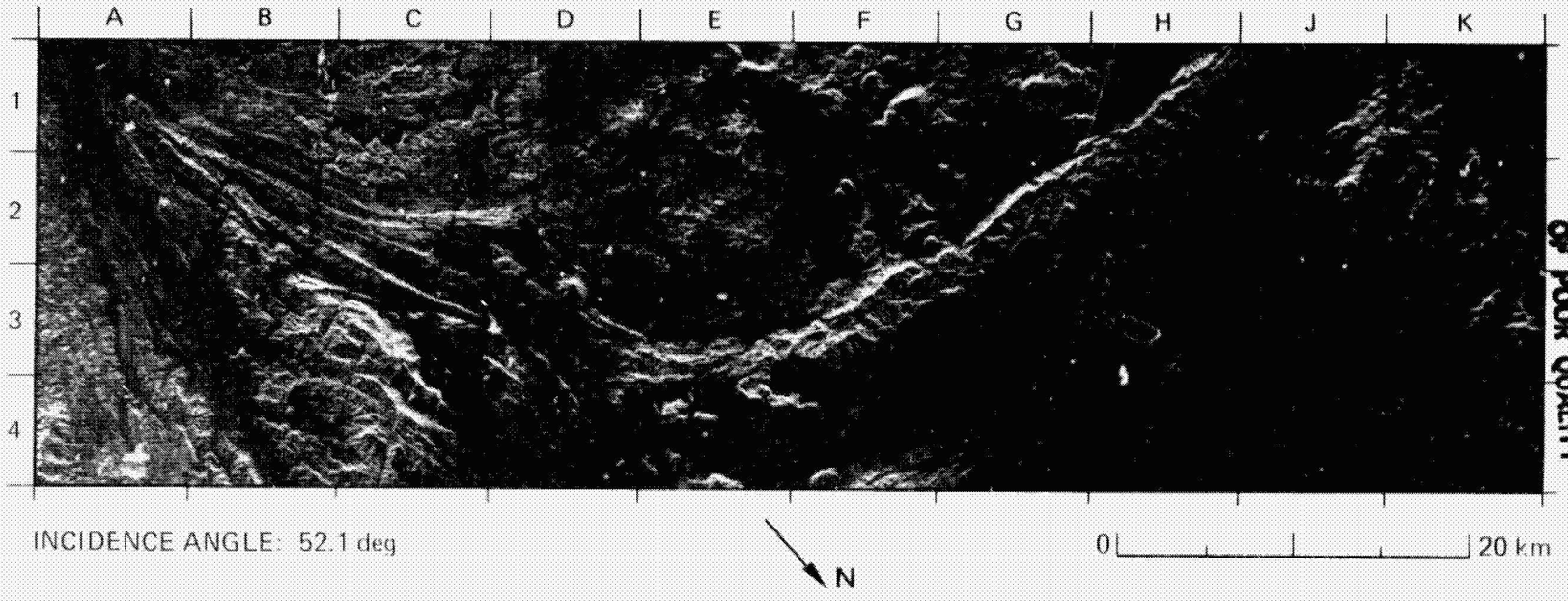




The pronounced arcuate feature from A1 to J1 on the radar image is part of an extensive complex of linear ridges in northeast Sudan. The ridges extend southward from this scene for about 150 km along the 35-deg-east parallel. The ridges are believed to trace a major suture line, called the "35-deg-east suture," where an island arc assemblage of volcanic and sedimentary rocks was destroyed during a Late Precambrian plate collision. Relations between this suture line, the present suture of the Red Sea, and the Dead Sea Rift Zone are shown on the regional sketch map that accompanies Image 2. Recent geodynamic studies suggest that the 35-deg-east suture was an antecedent of faults associated with the fragmentation of the Nubian/Arabian Shield and the opening of the Red Sea.

Ultrabasic rock masses are scattered throughout the volcanic-sedimentary sequence of the suture. The prominent ridge from F3 to J1 is formed from ultrabasic rock that is thought to be part of an ophiolite suite. Pillow basalts have been mapped at F4. The ridge exposures appear bright on the radar image because of their roughness relative to the radar wavelength. On the corresponding Landsat TM image, how-

Landsat TM Band 4



ever, the exposures appear very dark because of strong absorption by iron-rich material at the near-infrared wavelength (0.76 to 0.90 $\mu$m). Alluvial fans associated with the ophiolite and the pillow basalt are clearly perceptible on the Landsat image, though they are not seen on the radar image.

Paleozoic granite shows a subdued morphology on the radar image in the area from J1 to K3, and in the subtle circular feature at E1/E2, which has an approximate diameter of 10 km. Silica-rich granitic rocks show brighter image tones on the corresponding Landsat image. Sand in the wadis and on the lowland (for example, B2 to C1 and G4 to J1) is outlined by dark tones on the radar image, and by corresponding bright tones on the near-infrared image. In this scene, the radar image expresses small-scale textural differences in the rocks, while the near-IR image provides more compositional information.

(The Landsat TM image and the technical analyses upon which this caption is based were provided by Dr. Geoff Lawrence, Hunting Geology and Geophysics Ltd.)

## 8. Upper Rajang Region, Central Sarawak, Malaysia

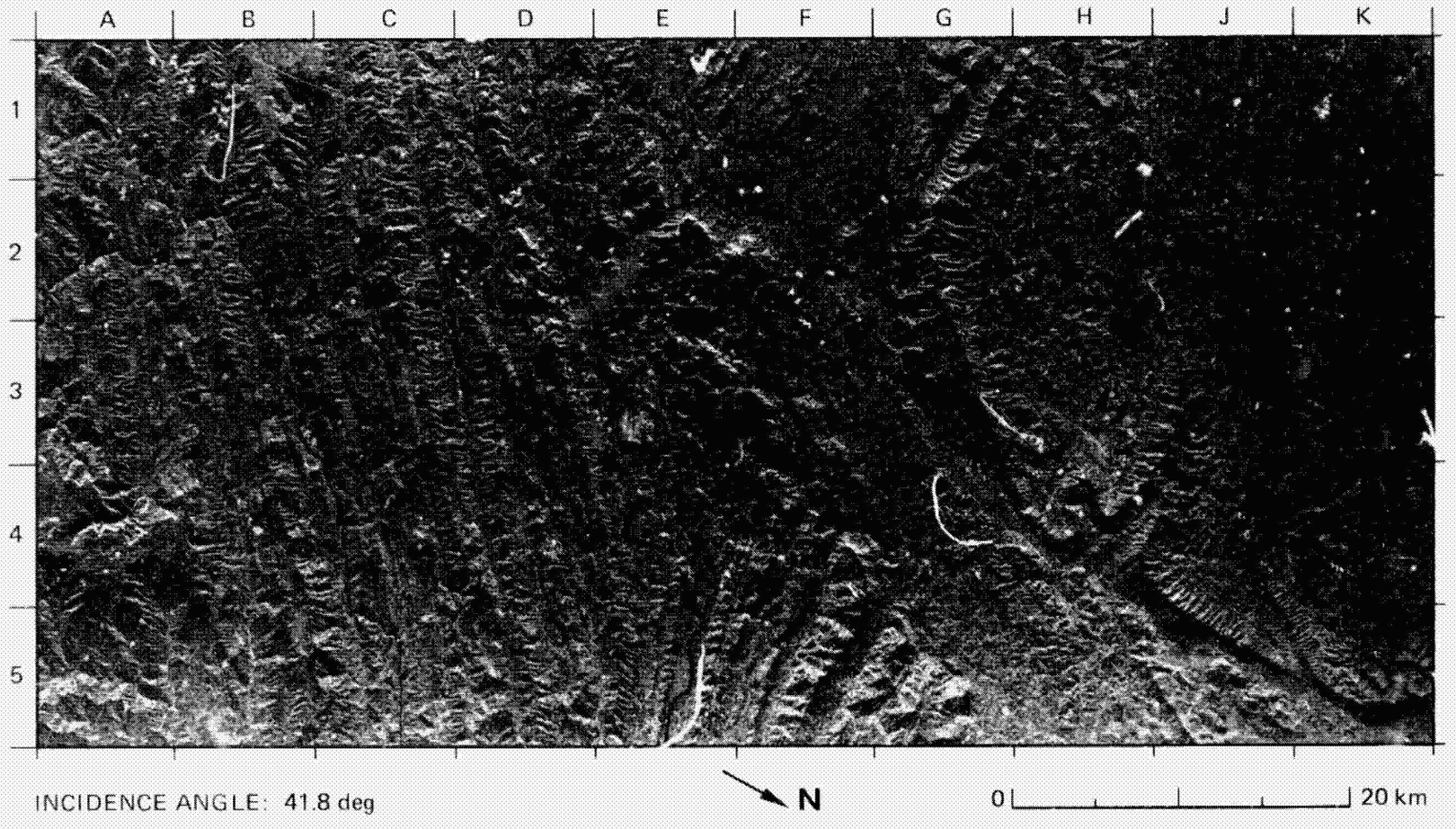

The Upper Rajang is a remote region of jungle-covered mountains separating isolated river basins. Structurally it is dominated by strongly folded, steeply dipping rocks that form an alternation of pronounced linear ridges and valleys (Kirk, 1957). Most of the vegetation is a hill-forest type dominated by species of dipterocarps that grow to a height of 50 m. Access to the area is difficult. Mapping has been confined mostly to the major river channels, which provide the main routes of communication; owing to the many rapids, only longboats can be used.

The SIR-B image covers portions of three distinct structural units in central Sarawak: the Rajang Block, the Kemena-Baram fold belt, and volcanic mesas.

In the Rajang Block from A1 to E1 through G5 to A5, massive Eocene sandstone and thick graywacke alternate with weak shale and siltstone to form pronounced linear strike ridges and intervening valleys. This results in a trellis drainage pattern. Dips range from 65 to 90 deg. Relief from the valley floors to the ridge tops ranges from 300 to 500 m. Linear transverse valley segments of the Balui River from A2 to B2 and tributaries from C3 to D2 are probaby controlled by joints or oblique regional faults. The ridges and valleys show a marked change of orientation from northeast to almost due east in the area from E3 to F5.

Less-deformed Oligocene to Miocene carbonate and clastic rocks in the Kemena-Baram fold belt extend from G1 and H1 through J2 to J5 and G5. Bedding traces and outcrop patterns on the radar image show the outlines of several open fold structures in the area. The divergence of the fold axes from the area at G4/H4 and the proximity of the sharp change in strike of the adjacent linear ridges in the Rajang Block indicate extensive large-scale deformation in this locality.

Flat-lying to gently dipping Quaternary volcanic rocks form mesas, which lie above the level of the linear ridges in the Rajang Block. The mesas have strongly dissected margins with precipitous cliffs and deep marginal embayments. Examples are at A3 to A4, where the steep slopes that face toward the radar illumination appear as very bright thin lines and those that face away from it are very dark, and at B1/C1. The elevation of these mesas is about 800 m.

Alluvial deposits in relatively level valley lowlands are swampy. They appear in monotonous gray tones from J1 and K1 to K2, and in a narrow zone from F1 to G5.

(This caption was prepared from material provided by Mr. C. H. Kho and Mr. S. P. Chen of the Geological Survey of Malaysia, Sarawak, Malaysia.)

FOLDOUT FRAME

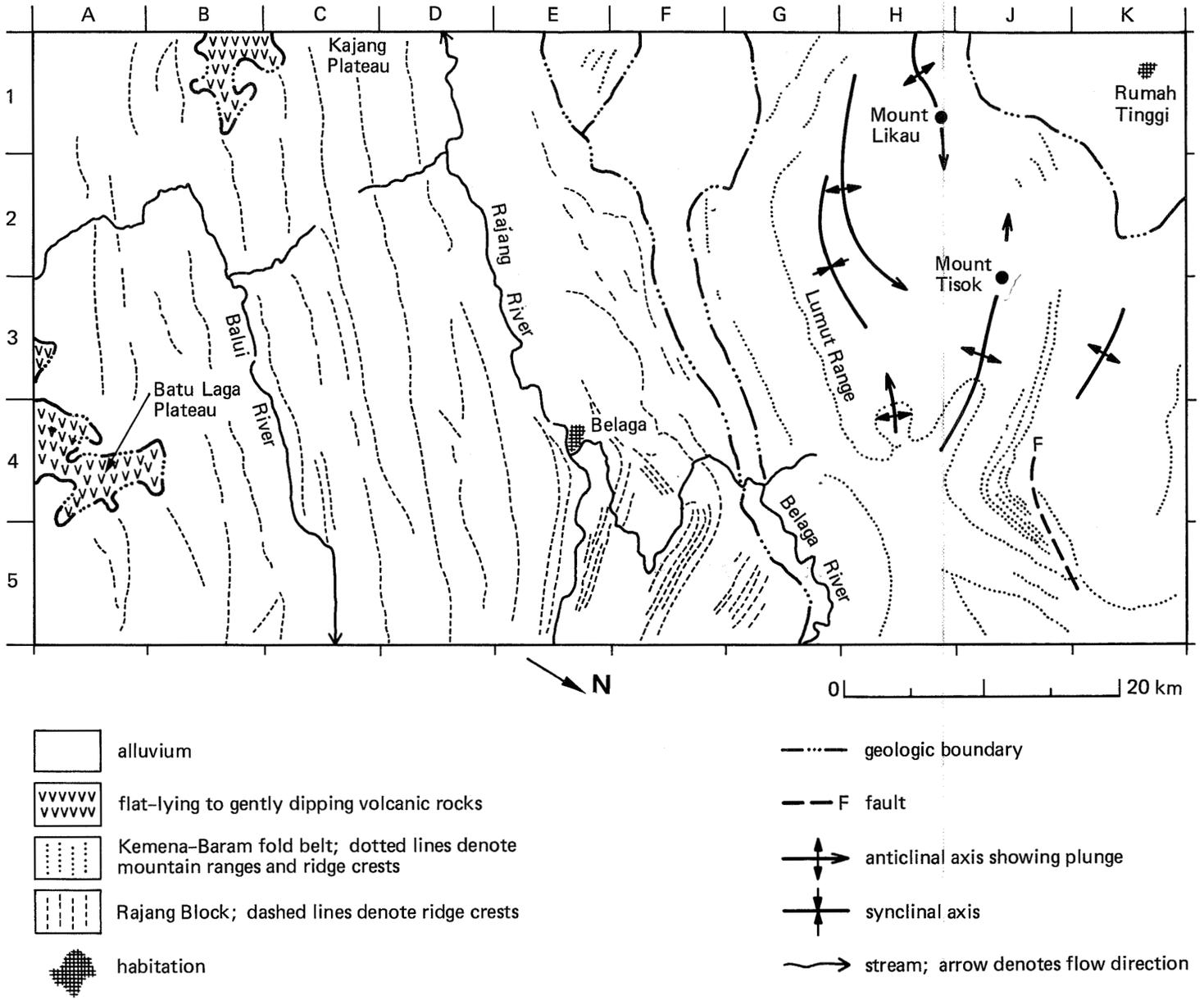


2

FOLDOUT FRAME

## (iii) Volcanic and Impact Terrain

## 9. Kilauea Volcano, Hawaii, U.S.A.

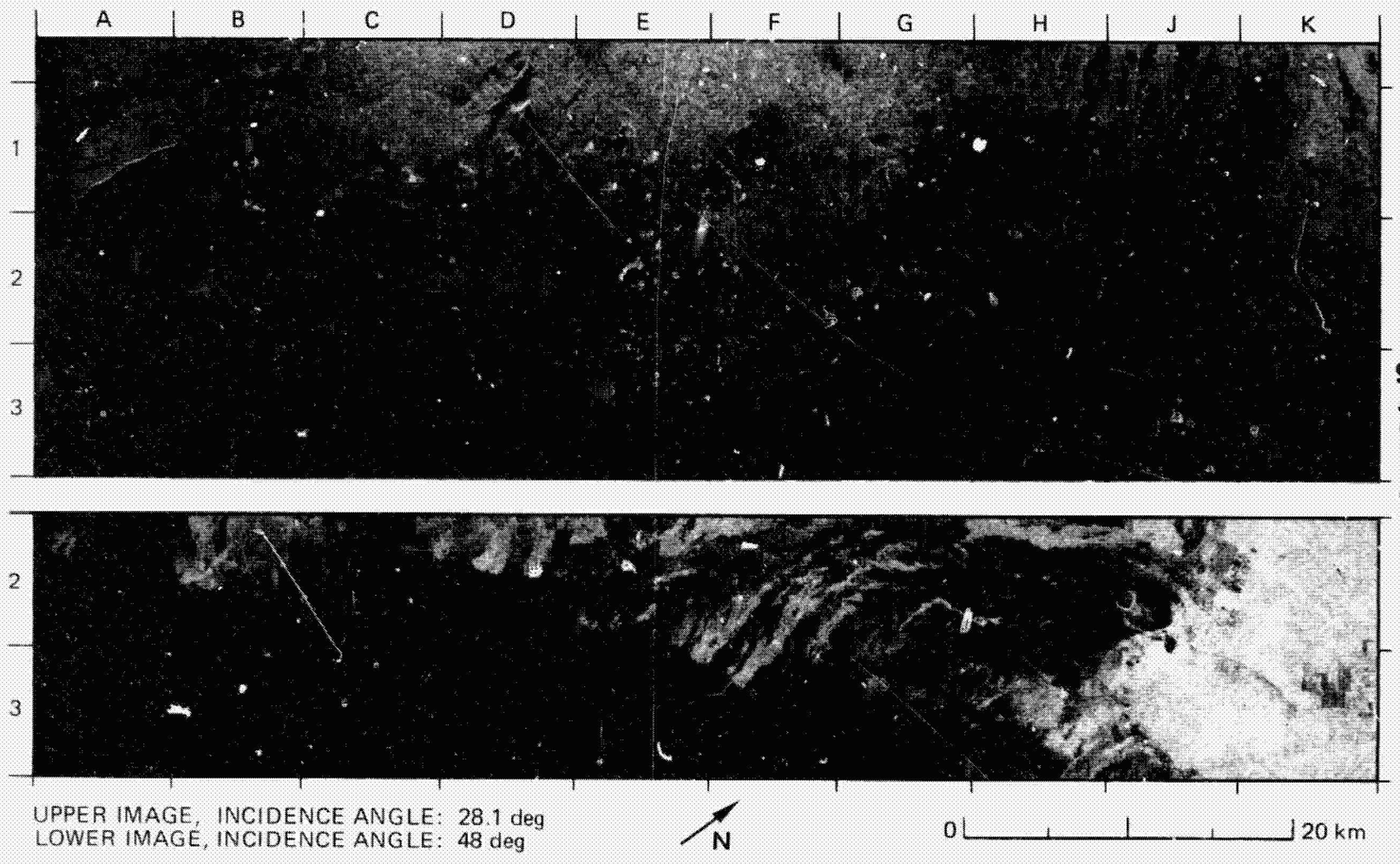




Images were acquired by SIR-B over southeastern Hawaii at incidence angles of 28 deg and 48 deg. The summit and Southwest Rift Zone of Kilauea Volcano were primary targets. Coverage extends from South Point (A2) through the Kau Desert (E2 to H2 through H3) and Kilauea Crater (J2).

The Kau Desert spreads southwest from the summit crater of Kilauea Volcano for almost 30 km. Its semiarid climate is produced by the rain-shadow effect of Kilauea as it blocks the prevailing northeasterly trade winds. In addition, acidification of rainfall by volcanic fumes has led to a very low vegetation density in the area. Rainfall and vegetation density increase sharply to the north and east of Kilauea Crater.

Because this pristine, unvegetated volcanic terrain contains several historic lava flows from Kilauea and Mauna Loa volcanoes, it is an ideal site for a test of the radar data's ability to discriminate and identify lava flows of different type and age.

Surface materials in the Kau Desert consist predominantly of airfall deposits and relatively young basaltic lava flows. The two main types of lava flow are easily distinguished: "aa" flows, which are extremely rough,

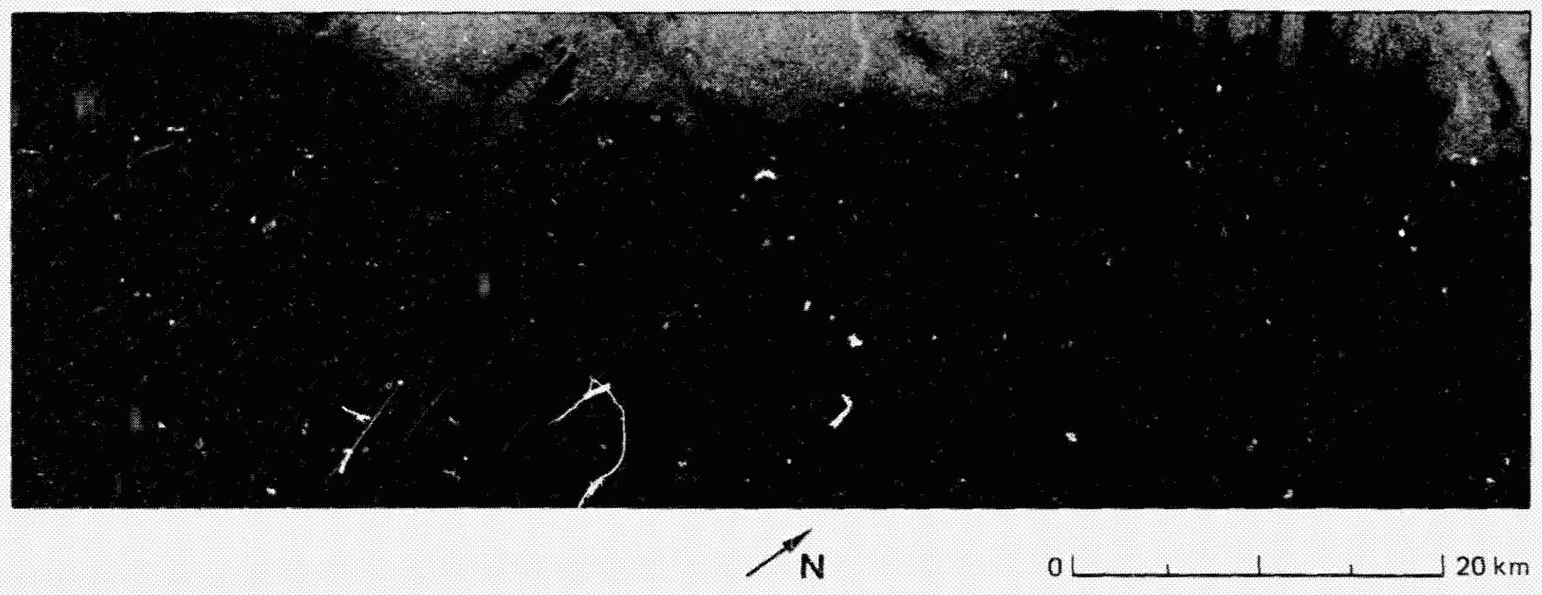




show up as bright areas; the L-shaped flow from G2 to H2 is an example. Smoother "pahoehoe" lava flows make up much of the darker surface of the Kau Desert.

Individual pahoehoe flows are not as easy to distinguish as aa flows. Through detailed analysis of the dual-incidence angle data, however, it has been possible to map different age ranges of pahoehoe and aa flows in the Kau Desert. This is a result of the smoothing effect of weathering processes, which tend to decrease the radar brightness of a surface with increasing age.

The summit of Kilauea is characterized by a collapsed caldera within which lies a smaller pit crater named Halemaumau (left side of J2). A line of smaller pit craters called the Chain of Craters extends southeast from Kilauea (left of center, J2 and J3) along the boundary between the desert and vegetated areas. Another large pit crater, Kilauea Iki, is the dark spot at the east rim of Kilauea Crater (lower right, J2). Most of the eruptions within Kilauea Crater produced smooth pahoehoe flows, causing the interior of the caldera to appear dark in the radar images. An exception to this is the bright tone of the deposits from an explosive eruption in 1924 that surround the north and east sides of Halemaumau. These deposits consist of sandy ash and numerous boulders up to 2 m in size.

The image acquired at the 28-deg incidence angle was used to generate the false color image, which emphasizes brightness differences between ash-covered surfaces, different types of lava flows, and vegetation. The image was constructed by separating the black-and-white image into three components based on brightness, after which each component was filtered to emphasize different size ranges of features. Finally, the three components were recombined as colors: red was used for the darkest component, green for the next darkest, and blue for brightest. Thus, red represents the lowest radar backscatter, and green and turquoise the intermediate backscatter; the highest backscatter is shown in yellow. Geologically, red indicates areas of smooth ash cover, dark green areas of smooth pahoehoe lava, light green areas of rough aa lava, and turquoise blue and yellow represent heavy vegetation.

(This caption was prepared from a text provided by Dr. Tom Farr of the Jet Propulsion Laboratory and Dr. Verne Kaupp of the University of Arkansas.)

## 10. Mount Shasta, California, U.S.A.

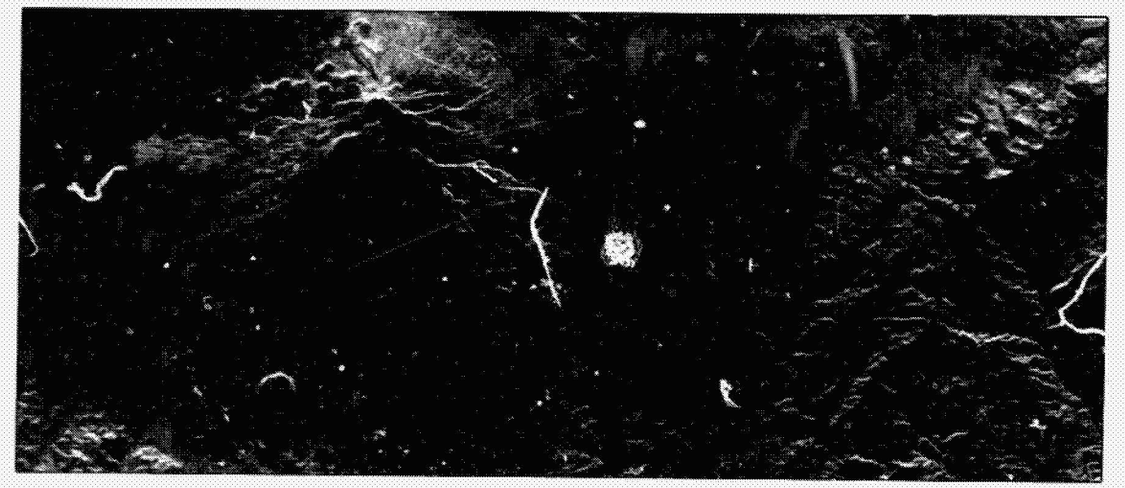

INCIDENCE ANGLE: 29.7 deg

INCIDENCE ANGLE: 53.8 deg

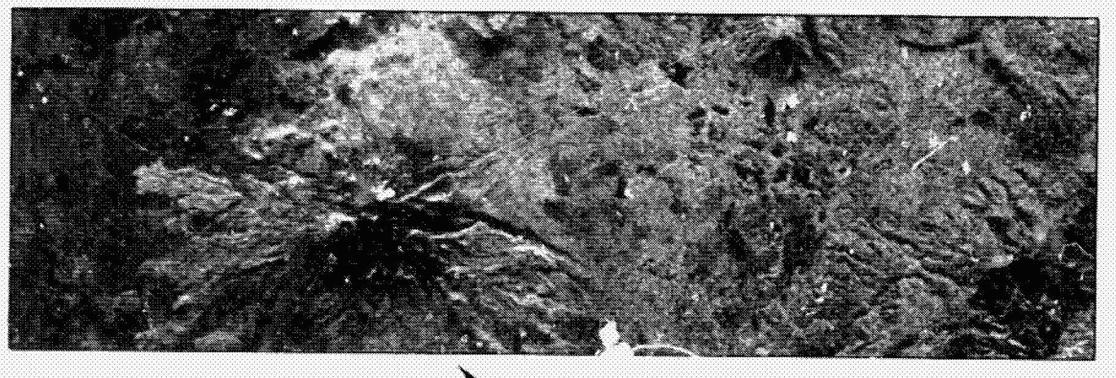

INCIDENCE ANGLE: 63.8 deg

N

20 km

(a)

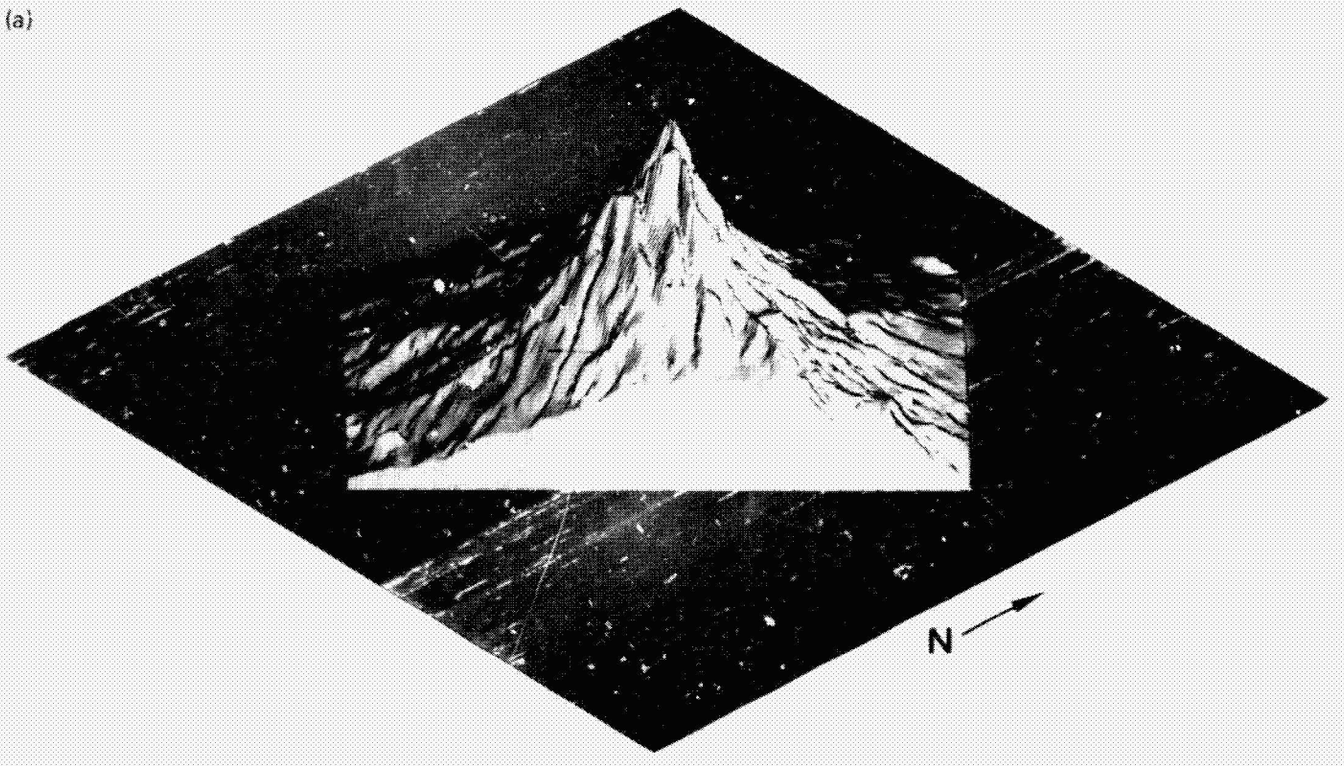




The possibility of using overlapping radar images for topographic mapping has intrigued researchers for many years, with the first theoretical contribution appearing as early as 1948 (Rinner). A considerable body of literature has since developed on the subject, although most work has been limited by the unavailability of radar image data.

The ability of SIR-B to image targets at different incidence angles on successive days of a one-week mission makes SIR-B ideal for a radar stereo-mapping experiment. Therefore, an effort was mounted to collect sets of images of geologic sites that were previously well-mapped so that a systematic stereo experiment could be performed. The objective was to determine the optimum incidence-angle combination for both visual interpretation of a geologic site and for topographic mapping. A multiple data set was collected over Mount Shasta, California, at incidence angles of 29.7, 53.8, and 63.8 deg.

Mount Shasta is a volcano of the Cascade chain. Recent results indicate that 350,000 years ago it may have undergone an explosion similar to that of Mount Saint Helens, but of vastly greater magnitude; the resulting debris created the Shasta valley to the north (Crandell et al., 1984).

A digital elevation model (a) was generated from the images obtained at incidence angles of 29.7 and 53.8 deg. With this data set, the X, Y, and Z coordinates as well as the radar brightness of each point in the scene are known. This information can be used to generate perspective views of Mount Shasta from a selectable vantage point. Twenty

ORIGINAL PAGE
COLOR PHOTOGRAPH

views of the mountain (figure (b)) were produced; all these views were generated from the data collected during the SIR-B mission. The color was derived from a color-density slice of the image obtained at the 29.7-deg incidence angle. This technique is particularly valuable for structural mapping of remote mountainous terrain.

(This caption was adapted from work by Dr. Franz Leberl of the Vexcel Corporation, Boulder, Colorado, and Dr. Mike Kobrick of the Jet Propulsion Laboratory; they generated the digital elevation model and the 20-view color image as well.)

## 11. Charlevoix Crater, Province of Quebec, Canada

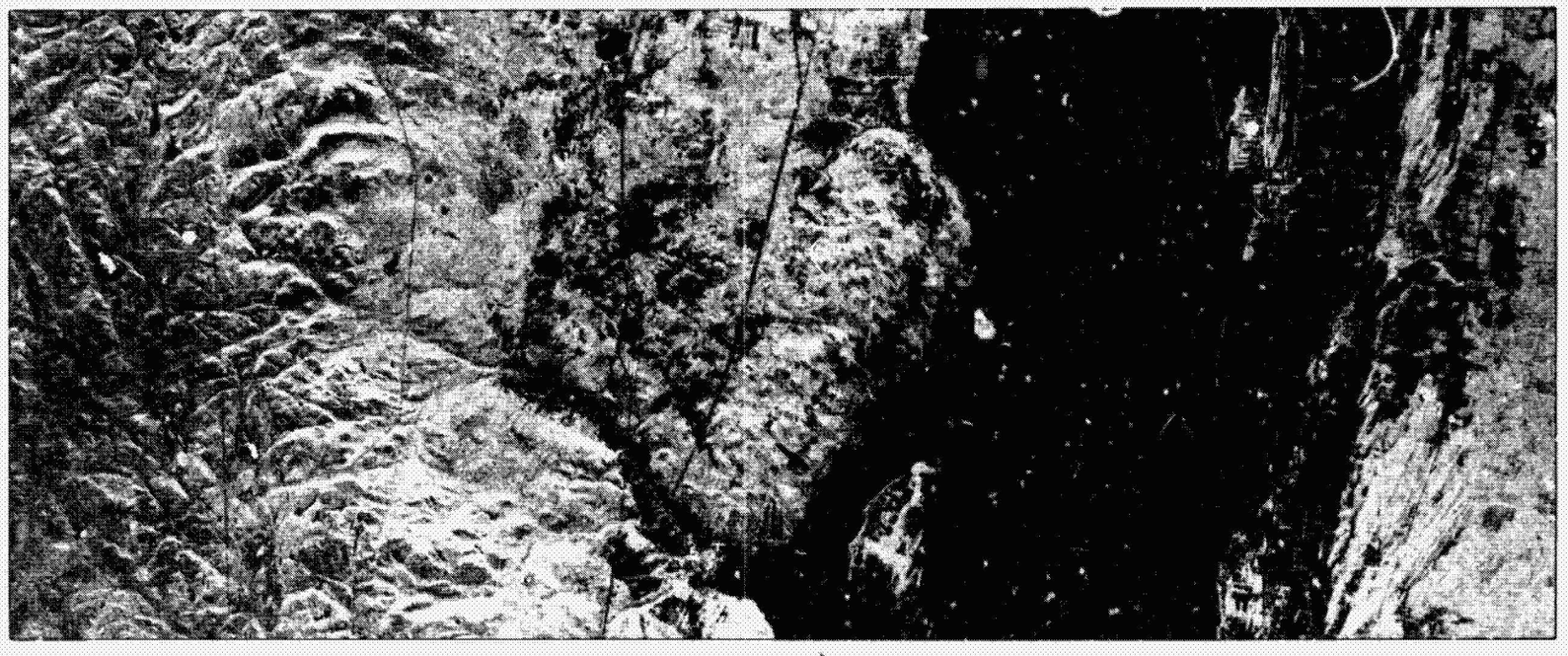

INCIDENCE ANGLE: 49.9 deg

N

0 20 km



Approximately 100 terrestrial impact structures with a diameter larger than 1 km have been recognized. Because the terrestrial geologic environment is dynamic, much of the characteristic crater topography has been removed. Recognition of these craters has been from the presence of circular anomalies detected initially on high-level aerial photographs and, more recently, on synoptic images obtained by Landsat. The processes of erosion, which hamper recognition, also expose the substructure at various levels; this exposure allows reconstruction of petrologic and structural relations within the crater. Such studies are complementary to studies of planetary craters where the initial morphology is well preserved, but the subsurface structure is inaccessible.

SIR-B data are being used to determine the radar backscatter characteristics of well-exposed impact craters; this will allow the detection and mapping of poorly exposed impact craters. Since the majority of

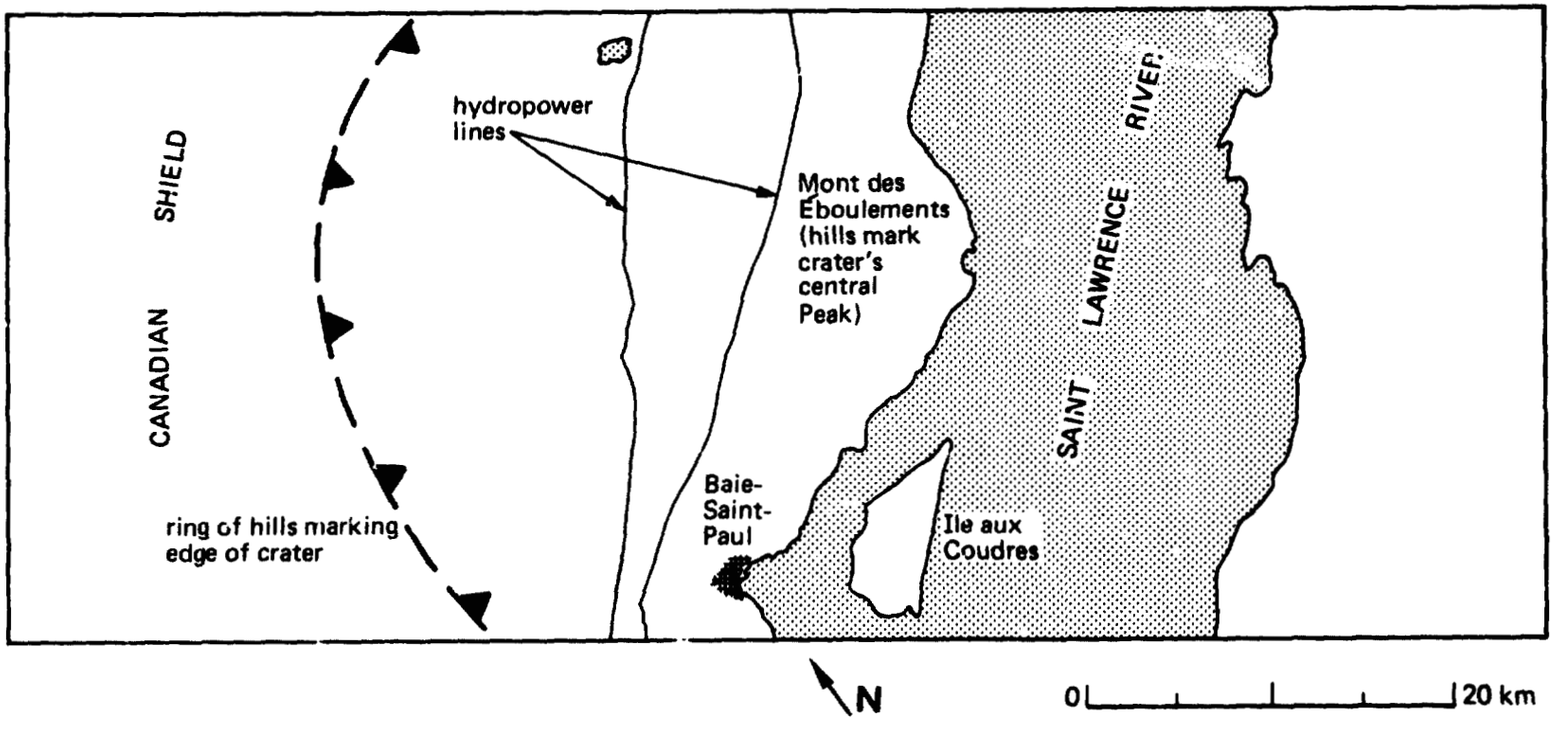


known terrestrial craters are on the North American craton, primary crater targets for the SIR-B mission are in Canada. One such crater imaged by SIR-B is Charlevoix. The sketch map locates the hills that mark the crater rim. Because of its low topography, the crater's center is used extensively for agriculture.

The Charlevoix impact crater is in a locally active seismic area parallel to the St. Lawrence River. The seismic activity probably relates to failure along normal faults in the Grenville basement; these faults antedate the impact event. Although the faults are not directly related to the impact, their seismic activity may have increased as a result of an increase in crustal weakness that accompanied the impact.

(This caption is an adaptation of technical information provided by Dr. James Head III of Brown University.)

## 12. Altiplano, Bolivia

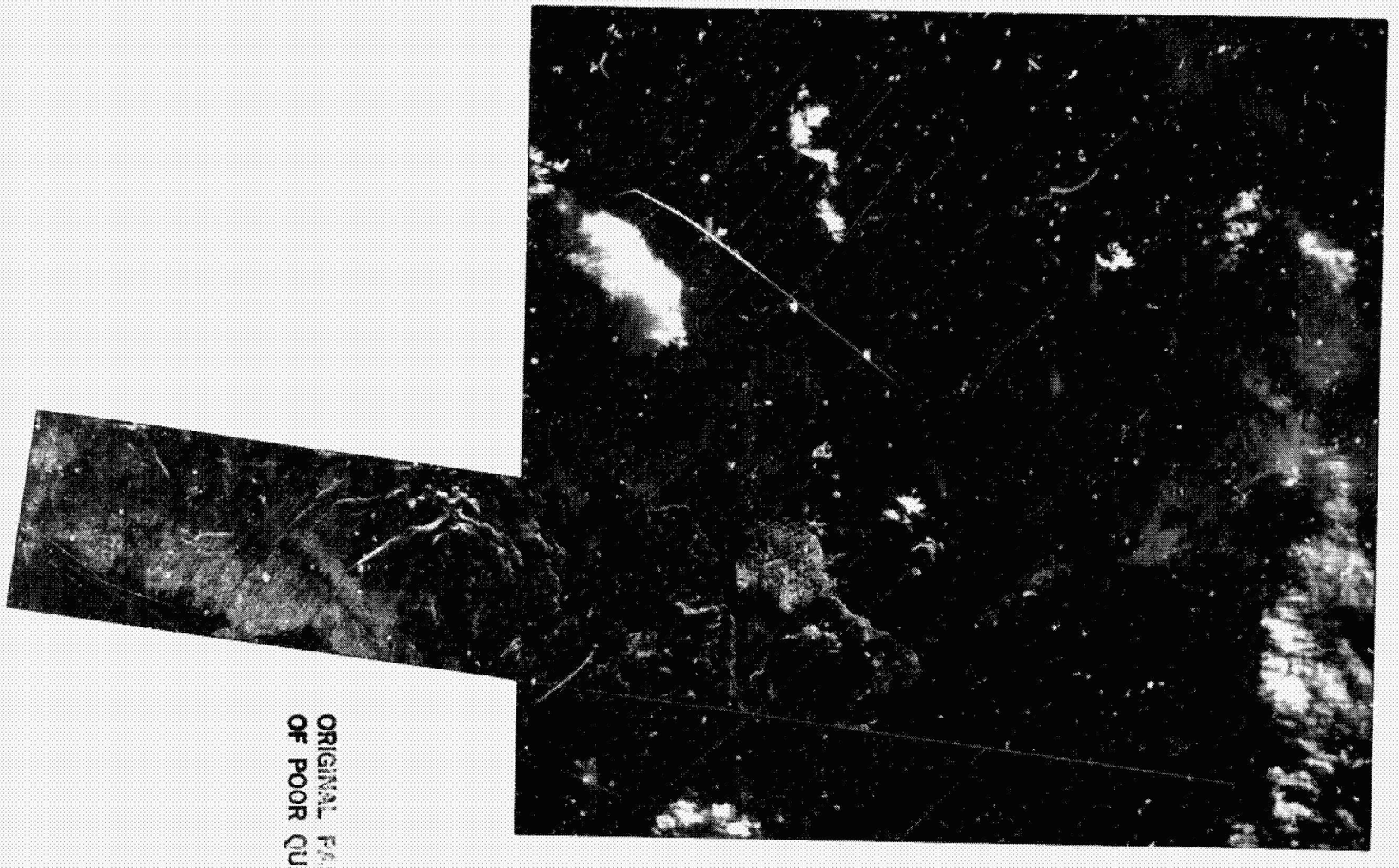

0 20 km

A set of overlapping Hasselblad photographs taken with a 250-mm lens by the crew on Flight 41-G over the Altiplano region of Bolivia provides a synoptic setting for this SIR-B image. The cold, dry plateau was characteristically nearly barren of vegetation and snow cover during the SIR-B flight, which provided ideal conditions for photographic and radar imaging of this remote area.

The Altiplano varies in elevation from about 3.7 km above sea level on most basin floors to volcanic peaks more than 6.5 km above sea level. For the past 25 million years, this region has undergone intense volcanic activity that is related to the subduction of the Nazca plate along the Peru-Chile trench (Jordan et al., 1983). Much of the surface is covered with dacitic-to-rhyolitic ignimbrites (pyroclastic flow deposits) and andesitic stratovolcanoes, some historically active (Baker and Francis, 1978).

The ignimbrite sheets of the Altiplano are notably bright on the SIR-B radar images, the result of very strong backscatter of the radar beam. This distinctively strong backscatter is probably attributable to the rough surface of the ignimbrites at two different scales of centimeters and hundreds of meters. The smaller-scale contribution to the backscatter is due to surface roughness that is a fraction of the radar wavelength (greater than about 4 cm for the 23.5-cm L-band radar). At the larger scale, straight parallel quebradas (gullies) appear to dissect the ignimbrite sheets.

These quebradas have a regional southeast trend (nearly perpendicular to the radar beam); their steep walls provide surface facets facing toward and away from the radar beam, and for this reason they appear on SIR-B images as pairs of parallel very bright and dark lines. The quebradas are 30 to 200 m apart and range in depth from a few meters to over 30 m.

(This caption was adapted from information provided by Mr. Eric J. Fielding, Mr. William J. Knox, Jr., and Dr. Arthur L. Bloom of Cornell University, Ithaca, New York.)

## (iv) Alluvial Fans and Dissected Plateau

## 13. Tuwaiq Escarpment, Central Saudi Arabia

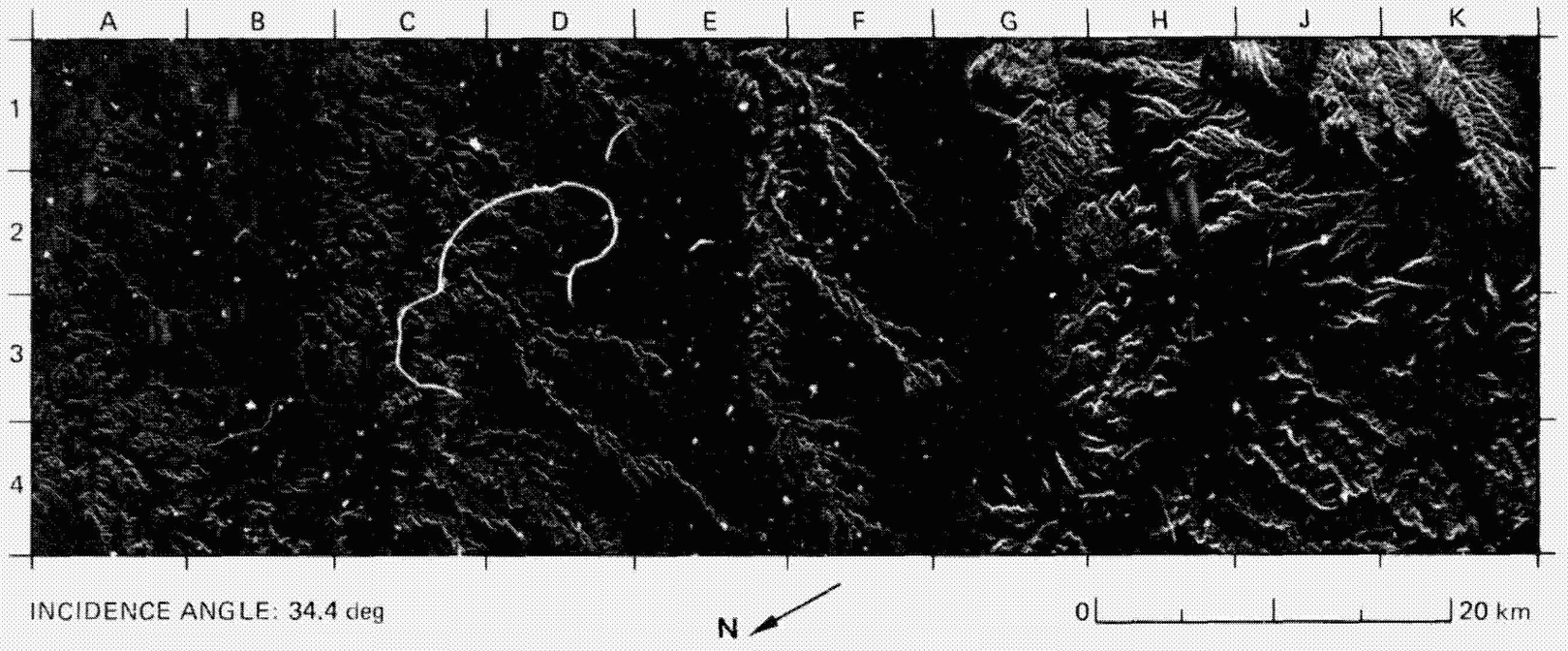




Differing hardness and compaction of the Jurassic limestones and interbedded shales that underlie the Tuwaiq escarpment result in distinctive surface textures that are characterized by sporadic traces of the bedding and variability in the extent of fluvial dissection. The bedrock in much of this area is mantled by silt and desert varnish. The contrasting textures are readily discriminated into radar mapping units, which are displayed as litnologies on the accompanying sketch map.

Flat-lying outcrops of alternating shale and limestone in the area west of Al Hariq (J3/K3 to J4/K4) exhibit distinctive convoluted scarps. The adjacent massive limestone that appears in a band from G4 through H1 to K2 forms prominent high scarps and flat plateau tops.

Overlying beds of soft lir. estone display a distinct and intensive drainage network. These beds form a characteristically low scarp with a basal silty hollow that appears dark on the radar image (for example, upper right quarter of G4). Compact homogeneous limestone forms moderate scarps and flat plateau tops, which show mostly dark image tones. Slightly brighter linear tones on the plateau tops are wash lines of coarse gravel and boulders entrained by flash floods. The limestones form important aquifers where they dip eastward beneath younger sediments. Local wadi sands, which appear dark on the image, bear sufficient water to supply the oasis at Al Hariq (H2).

The linear feature that extends from B2 to C3 is possibly tectonic in origin.

(This caption is based on a technical analysis by Dr. Geoff Lawrence, Hunting Geology and Geophysics, Ltd., who also provided the sketch map.)

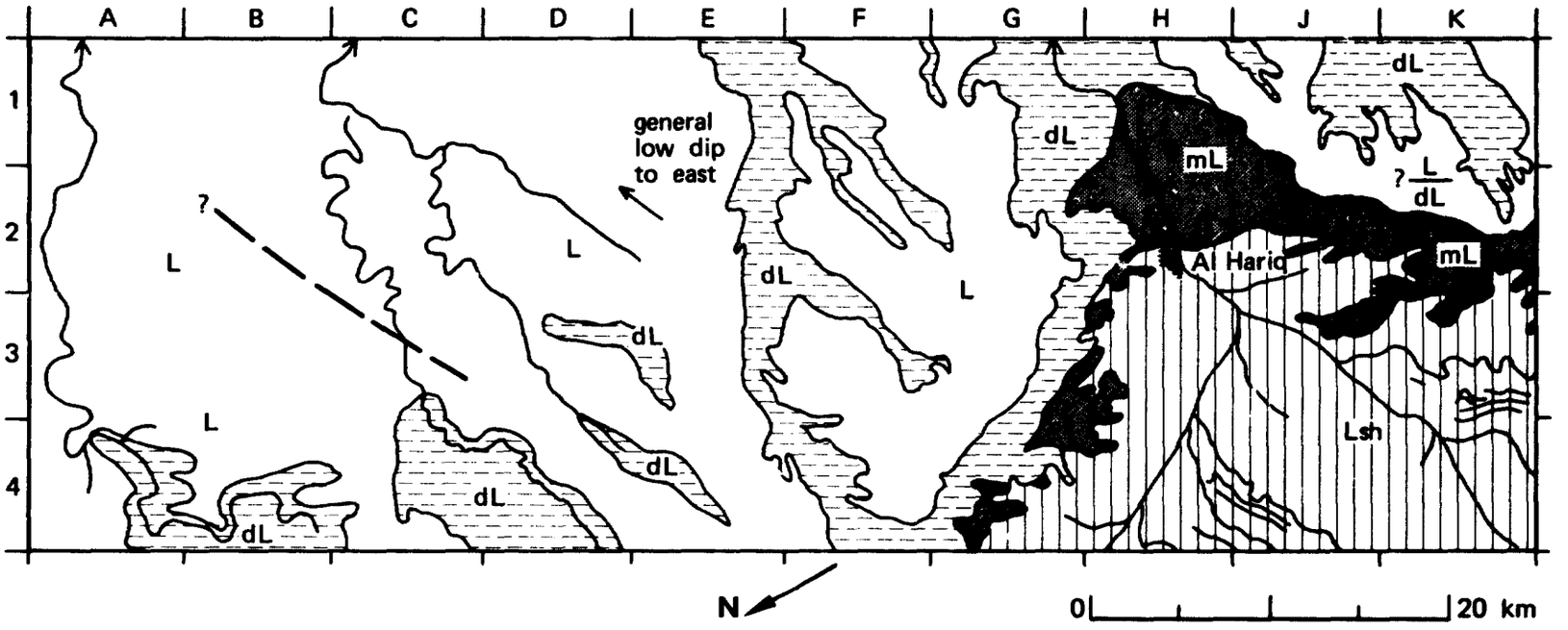


L — limestone, compact, homogeneous

dL — limestone, soft with shale interbeds

mL — massive limestone

Lsh — limestone/shale

topographic lineament

stream; arrow denotes flow direction

## 14. Spring Mountains and Pahrump Valley, Nevada, U.S.A.

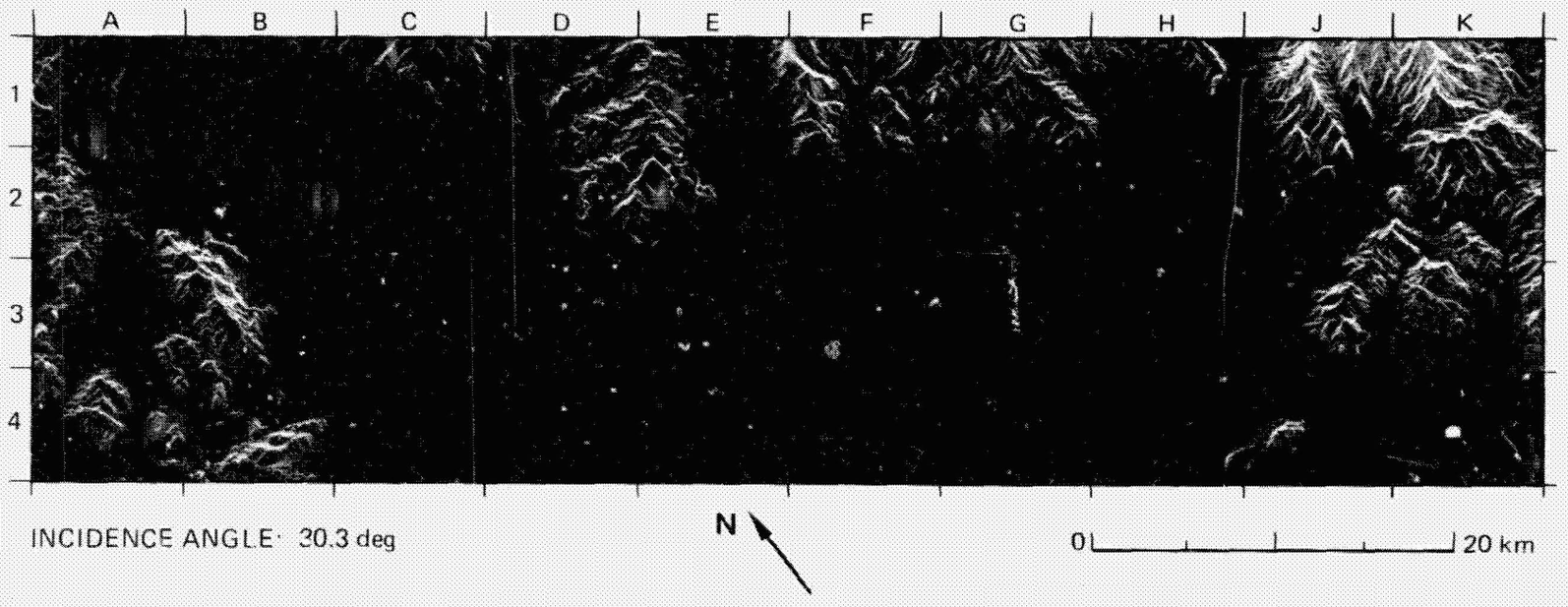




This scene in southern Nevada includes the western portion of the Spring Mountains and the eastern half of the Pahrump Valley. In the mountains, Paleozoic sedimentary rocks over 7000 m thick are exposed; Precambrian metamorphic rocks are in the northern part of the scene. The rocks include limestone, dolomite, quartzite, marble, shale, sandstone, and some gypsum. Major features displayed on the image are shown on the accompanying sketch map.

The complex geologic structure of the Spring Mountains is dominated by large thrust faults and associated folds. Normal faults with a northwest strike are also present. The curvilinear feature from J1 to K2 on the image is the Keystone Thrust. This feature is readily detected on the image because its trend is nearly normal to the direction of radar illumination. The linear feature in E1 is the Lee Canyon Thrust. This feature is largely obscured on the image because the trend is nearly parallel to the radar illumination.

The mountains are flanked on all sides by an apron of alluvial materials. The apron consists of large alluvial fans formed from the progressive coalescing of numerous small fans. Two large alluvial fans lie in the areas from A1/A2 to D2 (Pahrump Fan) and from E2/E3 to J3 (Manse Fan). Surface materials on these fans are poorly sorted alluvial gravels, sand, silt, clay, and caliche. On the upper portion of the fans the rocks are very coarse, angular, poorly sorted, and dip at angles from 12 to 18 deg. The rougher surfaces yield greater radar backscatter and consequently appear brighter on the image.

There are no perennial streams in the Spring Mountains. Rainwater percolates through the very permeable alluvial fans to the groundwater system with little to no surface runoff. The surfaces of the fans are cut by numerous washes (channels) of varying size that appear bright on the image. Normally the washes are dry, and very little vegetation is present in them. Periodically the washes are cut by flash flooding. Large cobbles and boulders deposited in the washes at such times yield bright returns on the radar image.

(The caption was prepared from information provided by Mr. Marcus Borengasser, Mackay School of Mines, University of Nevada.)

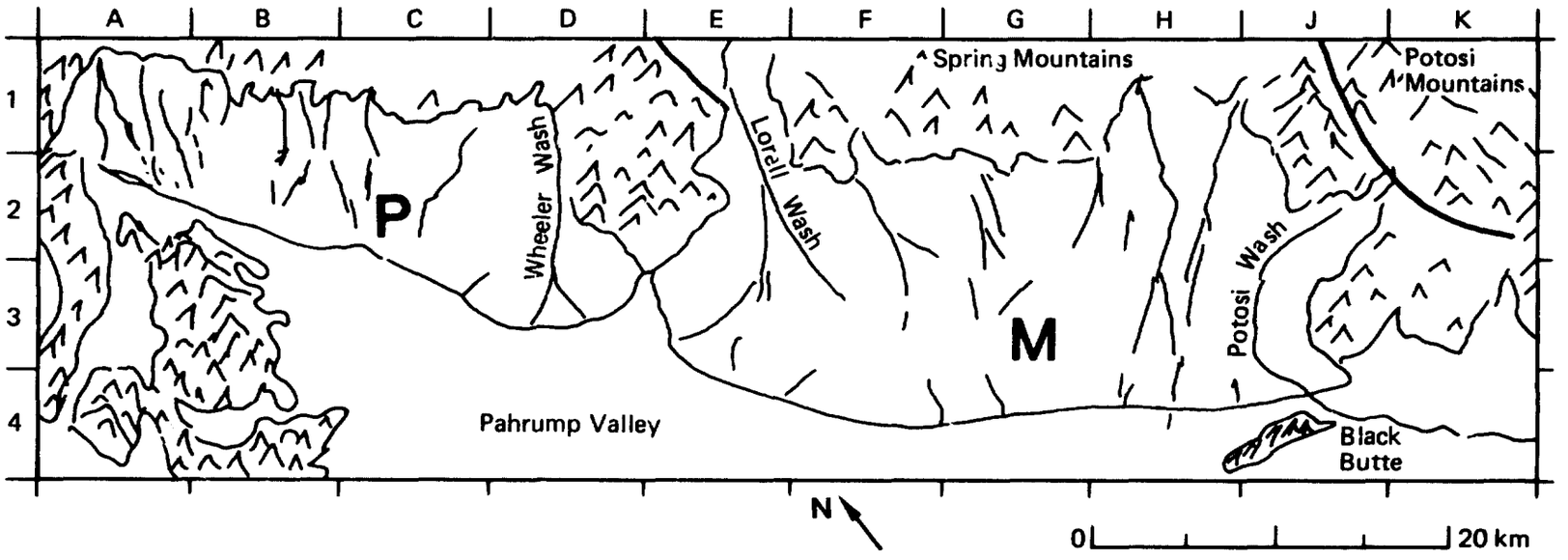


thrust fault

mountains

P Pahrump Fan

M Manse Fan

## (v) Eolian Features

## 15. Wind-Eroded Sandstones, Borkow Province, Northern Chad

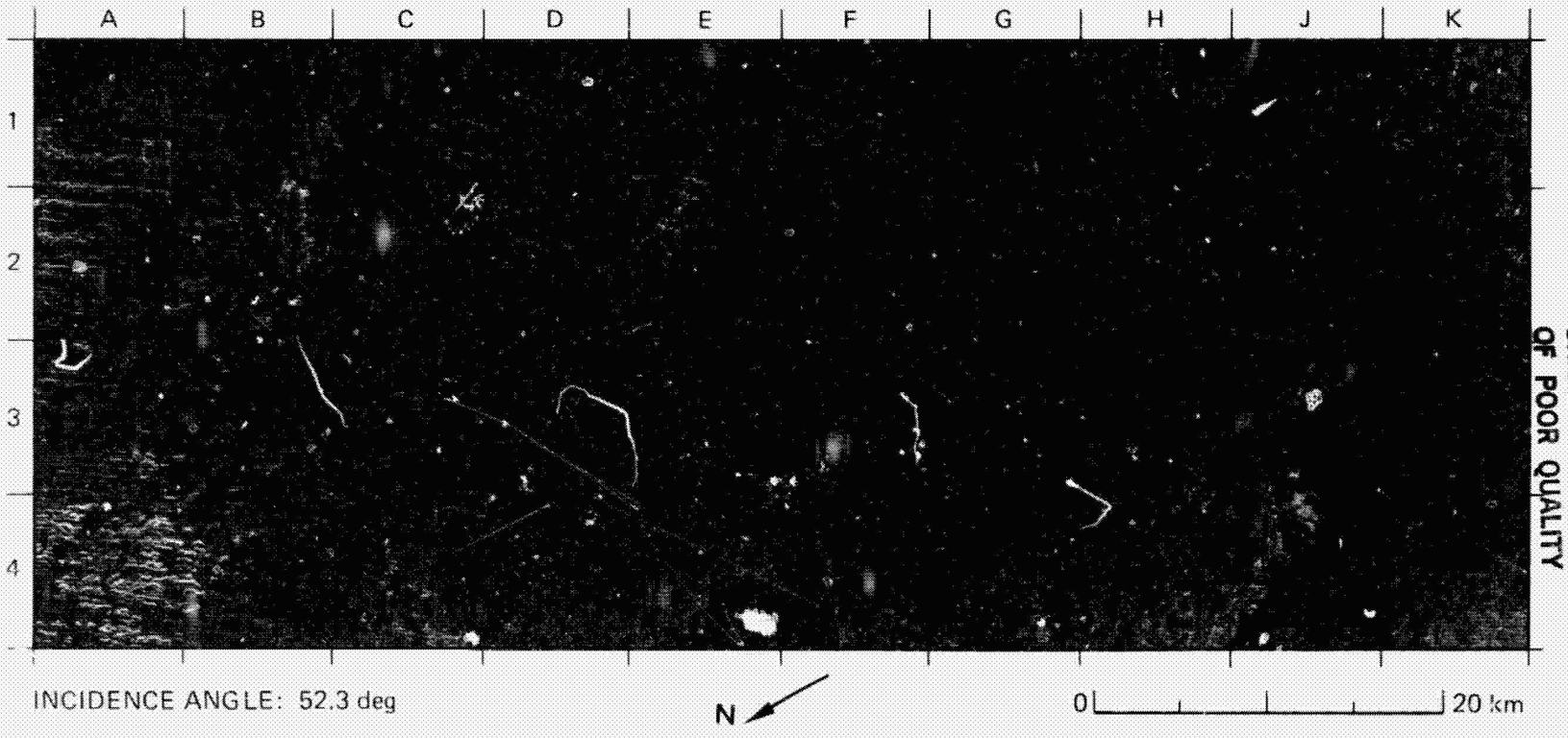




Paleozoic sedimentary rocks at the rim of the Koufra Basin in Libya have been peneplained and sculptured by the wind for thousands of years. In this scene south of the Libyan Desert and east of the Tibesti Mountains, the bedrock of Devonian sandstones shows varying resistance to erosion. Different image textures indicate the presence of four sandstone units whose boundaries are marked by bedding scarps. Unit 1 (see sketch map) is the most resistant though it is deeply dissected. It is characterized by moderate relief (for example from A2 to A4) and by a pronounced scarp from B2 to C1 and from D1 through D2/E2 to E1. Units 2 and 3 show low to very low relief, and limited areas of outcrop. Unit 4 shows a limited outcrop at J3/J4. The strike of the sandstone units is across the image in the range direction: from the top (near range) to the bottom (far range); the dip is gentle toward the north. This structure results from the relative tectonic stability of the underlying Precambrian craton. A subtle linear feature that extends across the strike from A4/B4 to D2/E2 probably represents a fault trace. Ancient drainage channels in the area suggest the existence of a former wetter climate in this arid region. A patchy veneer of thin sand appears in dark tones on the image.

The extensive dark linear streaks that are nearly normal to the strike of the bedrock units are gullies formed in response to a lengthy period of wind erosion. Strong persistent winds blow to the southwest and south-southwest from the giant sand seas in the Libyan Desert. Sand deposited on the floors of the gullies is nonreflective at the relatively high radar incidence angle of this scene. Brighter tones on the image indicate stronger radar backscatter from the rougher surfaces of the outcropping bedrock.

(The caption and sketch map were prepared from technical information provided by Dr. Geoff Lawrence, Hunting Geology and Geophysics, Ltd.).

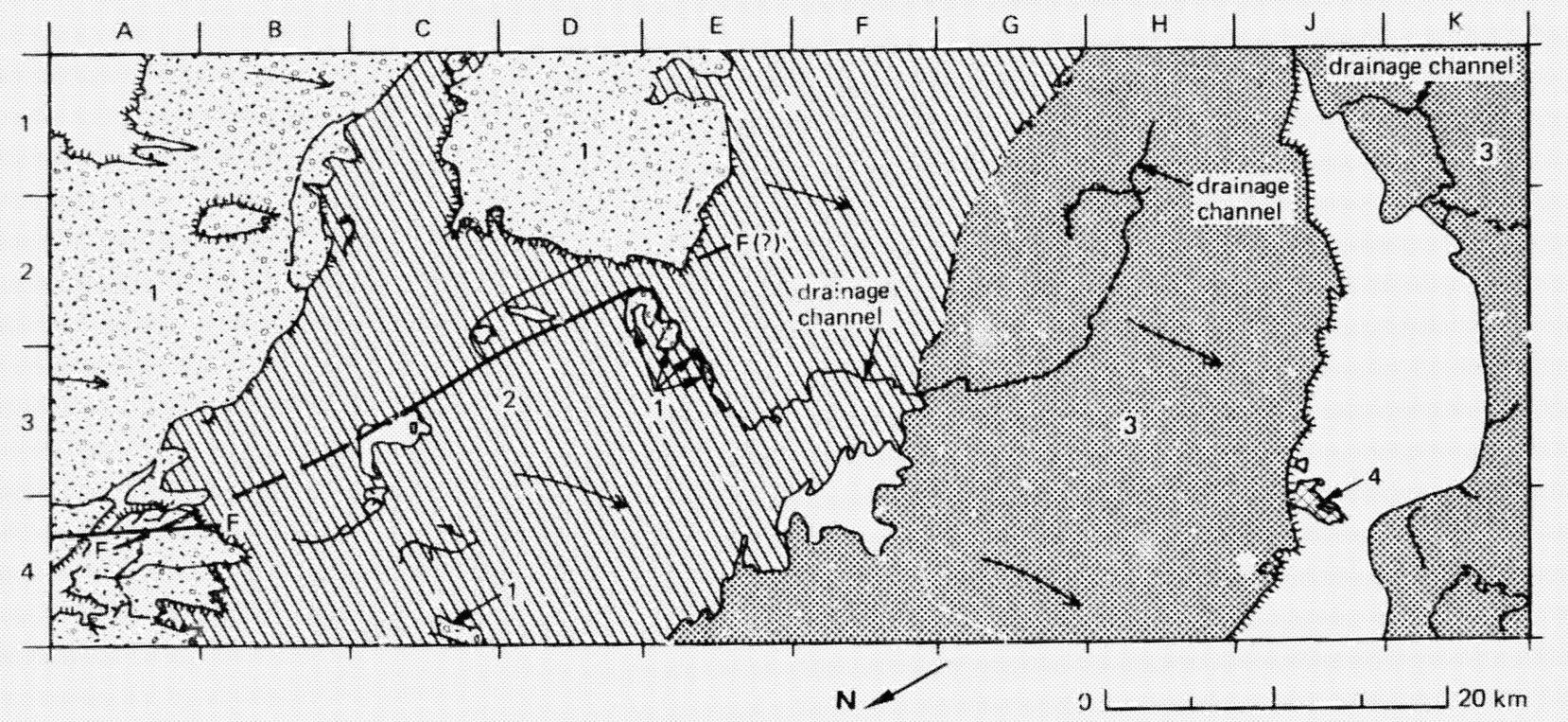


sand

4 sandstone unit(?)

3 sandstone, low to very low relief, limited outcrop

2 sandstone, very low relief, sand veneer, limited outcrop

1 sandstone, deeply dissected, strong ridges, extensive outcrop

flat terrain with thin veneer of dry sand, parallel to dominant wind direction

scarp

F linear feature, fault(?)

## 16. Gebel Mufta, Western Desert, Southwest Egypt

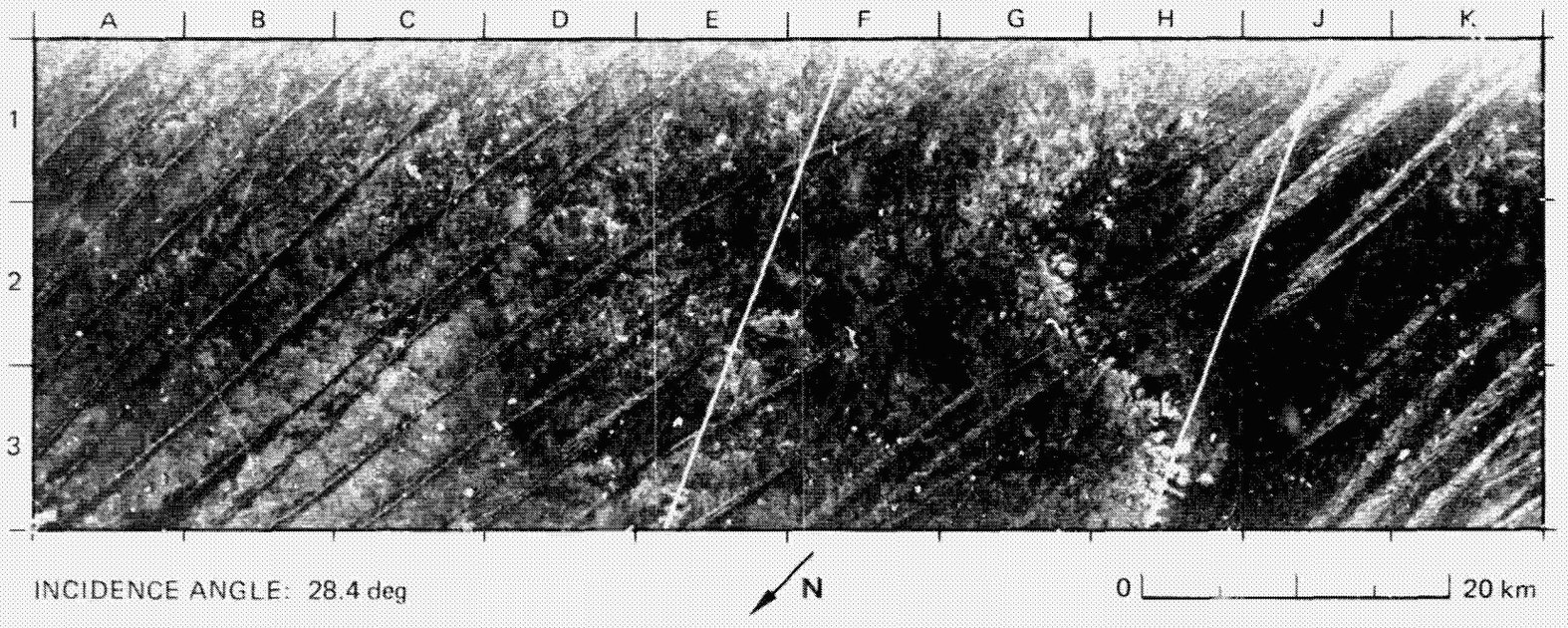




The western desert area of southwest Egypt is underlain by Mesozoic sandstones and shales. Low irregular scarps mark the outcrop of more resistant rocks. Quaternary sand and gravel deposits cover wide areas and long linear dunes extend in a north-south direction for great distances.

The area was imaged by SIR-B with two different directions of illumination, each at a different incidence angle. The image shown above was obtained from a southeast look direction at an incidence angle of about 28 deg. The azimuth angle between the southeast look direction and the long axis of the dunes is about 52 deg. The scarp of Gebel Mufta appears bright in the area from G1 to H3. A large rock pediment area in front of the scarp that may be partly covered by radar-transparent sand appears in moderately bright tones on the image from H3 to J3. Thicker sand sheets in the interdunal areas appear in darker tones (for example, in the area between J3 and K2). Brighter tones are observed in interdunal areas that expose moderately rough sandstone and shale surfaces (for example, in the area from B3 to C2).

The portion of the image between the parallel lines from E3 to F1 and from H3 to J1 was also imaged by SIR-B from a northeast look direction at an incidence angle of about 43 deg. The azimuth angle between the northeast look direction and the long axis of the dunes is about 57 deg. In addition to portions of the dune field, the area of common coverage includes Gebel Mufta and Twin Hills (E2 to E3). The corresponding segments of the two image swaths are shown for comparison on the facing page.

Gebel Mufta and the Twin Hills area appear about equally bright in both images. The rock pediment in front of Gebel Mufta is less clear on the left image, probably due to a low signal-to-noise ratio in the far-range position on the image. In both images, the same-side slopes of the dune surfaces face toward the radar illumination. The azimuth angle between

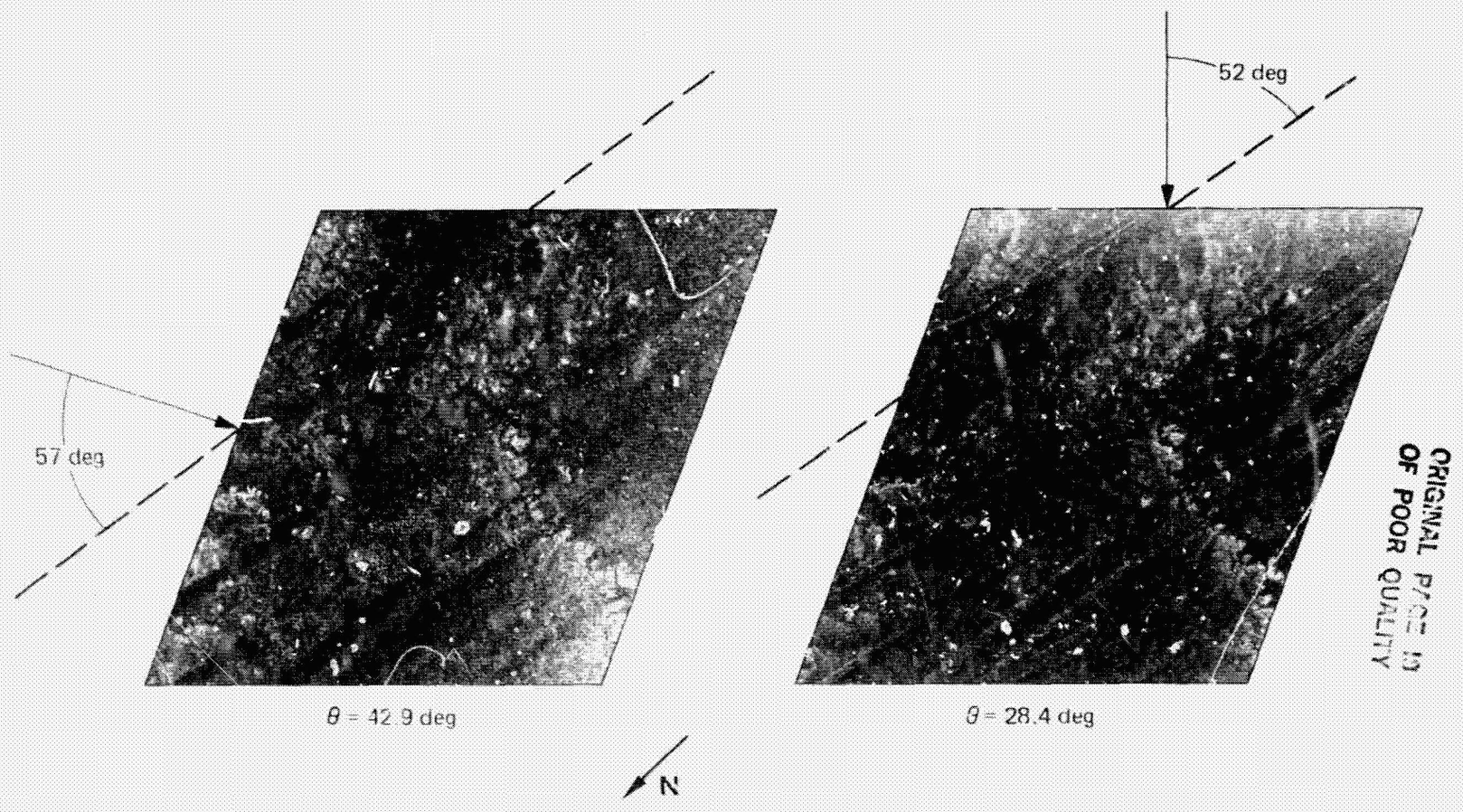




the radar illumination and the long axis of the dunes is comparable in each case. However, at the 28-deg incidence angle, the dunes are clearly perceived with numerous bright reflections from appropriately oriented dune slopes (right image). At the 43-deg incidence angle, the dunes appear as dark streaks that are outlined only by their brighter surroundings (left image). This illustrates the observation that dune surfaces yield radar backscatter only when the radar incidence angle is less than the angle of repose of the dune slopes (about 34 deg).

At the 28-deg incidence angle (right image), some of the dune faces are oriented nearly normal to the radar illumination. This produces specular reflections that yield bright tones on the image. At the 43-deg incidence angle (left image), the dune faces are more highly inclined to the radar illumination. In this case, very little radar energy is returned and the dunes are outlined by dark image tones. Detailed relations between illumination geometry and the perception of sand dunes on radar images have been documented by Blom and Elachi (1981, 1986).

## 17. Hexi Corridor, Gansu Province, China

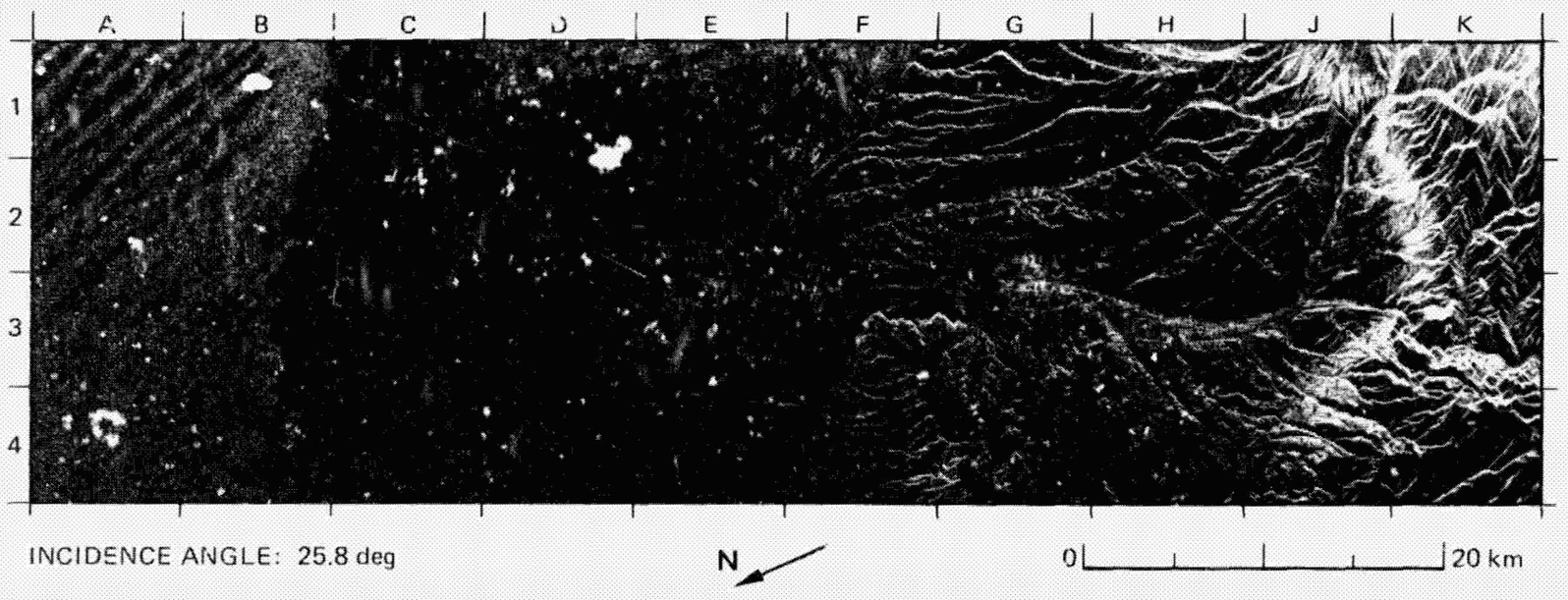


The Hexi Corridor in central China is a series of valleys that separate the Qilian Mountain Range to the southwest from the Tengger Desert to the northeast. Oases along the Hexi Corridor formed important stops on the ancient Silk-Road trading route between China and the West. The village of Huang Yangzhen lies on the road between Wu Wei 35 km to the northwest, and Lanzhou, 190 km to the southeast. The corridor is clearly demarcated on the image by linear patterns of settlement and cultivation in the area from C1 to F1 through C4 to F4. A circular pattern of cultivation about ½ km in diameter is present in the lower left portion of D3. The present routes through the corridor that appear on the image include a single-track railroad from D1 to D4 and a roadway from E4 to F1. Channels of intermittent streams from the Qilian Mountains traverse the corridor area.

The Qilian Mountain Range is composed predominantly of Paleozoic schists and gneisses. The mountains extend from the foothills at about 2000 m elevation (F1 to F4 through H1 to H4) to high peaks at about 4000 m (K1 to K4). The image texture shows that the mountains are rugged and deeply dissected. The smooth linear to curvilinear outlines and form of the valleys that extend from G3 to K1 and from F2 to H1 provide clear evidence of former glaciation in the mountains. Linear patterns of cultivation are evident on the floor of the larger valley between G2/G3 and J3.

The accompanying sketch map shows the outlines of a linear escarpment and pronounced linear features in the foothills that are probably fault controlled. The finely textured area in the foothills from G2 to H3 through G4 to H4 probably represents a dissected loess surface. An abrupt change in the texture of the mountains from J1 and K1 to K3 denotes the limits of the loess.

The image area from A1 to B1 through A4 to B4 shows a portion of the Tengger Desert. The surface of the desert in this region is covered by large numbers of small crescentic dunes about 2 to 3 m high and 5 m wide at an average elevation of 1700 m. The lower portions of the dunes are about 10 to 15 percent vegetated. At the incidence angle of about 26 deg used in this scene, only the sectors of the small crescentic dunes that are normal or nearly normal to the radar illumination show bright image tones. The remaining surfaces appear relatively dark and poorly defined despite the thin vegetation cover. Consequently, the crescentic form of the dunes is not perceived on the radar image. Linear interdunal corridors up to 1 km in width appear dark in the area from A1 to A2 through B1 to B2. Such areas probably have smooth and relatively unvegetated sand-free surfaces.

(The caption and sketch map were prepared from information provided by Dr. Alta Walker of the U.S. Geological Survey.)

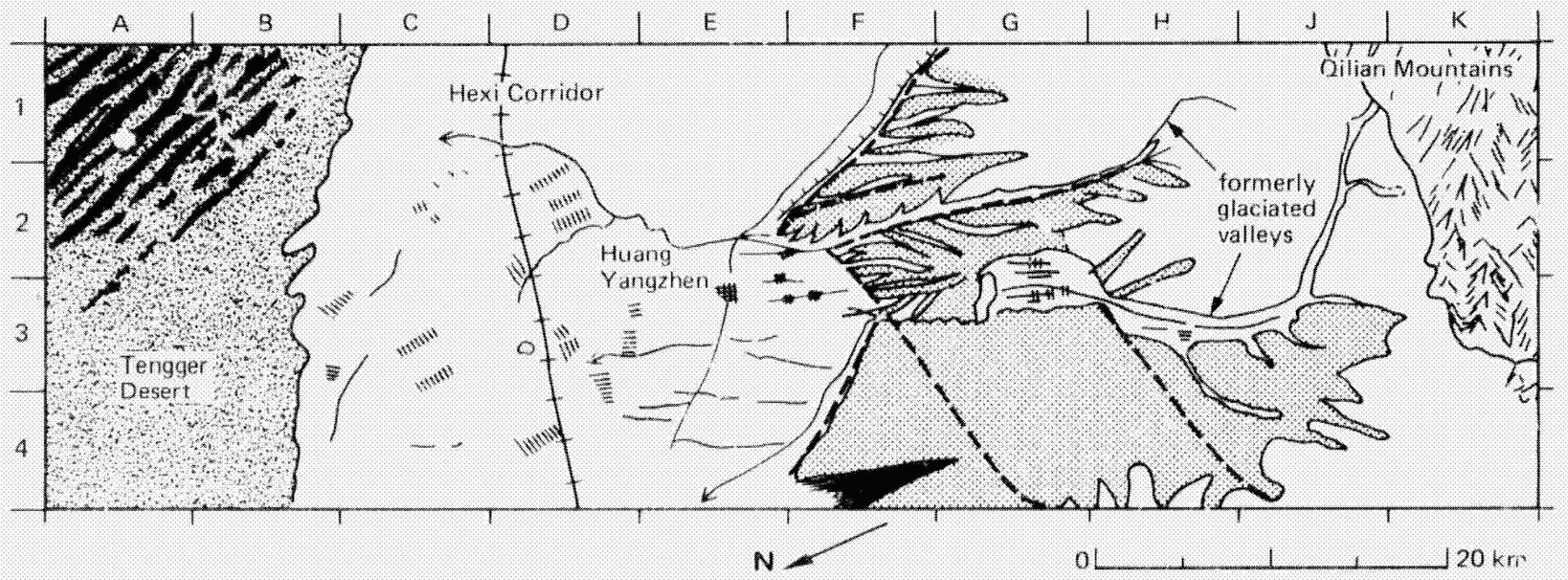


schist and gneiss

dissected loess

dunes

interdunal area

lineament

escarpment

stream; arrow denotes flow direction

single-track railroad

cultivation

habitation

# B. Renewable Resources

The increased capabilities of SIR-B have allowed better and more useful measurements of the Earth's renewable resources. Multiple-incidence-angle observation has extended the utility of spaceborne radar data by allowing, for the first time, incidence-angle-related parameters to be characterized and their impact on image interpretation and classification assessed. The SIR-B images in this section were obtained at incidence angles from 21 deg to 59 deg.

The first efforts to utilize this information are well depicted in the color composite images (scenes 24 and 26) where the component of radar backscatter for each incidence angle is assigned a color. This technique allows a simple and direct method of qualitatively assessing radar backscatter as a function of incidence angle, and may well be extended quantitatively when calibrated imagery is collected on the reflight of SIR-B.

## (vi) Hydrology and Drainage Networks

## 18. Rio Japurá, Amazonas, Brazil

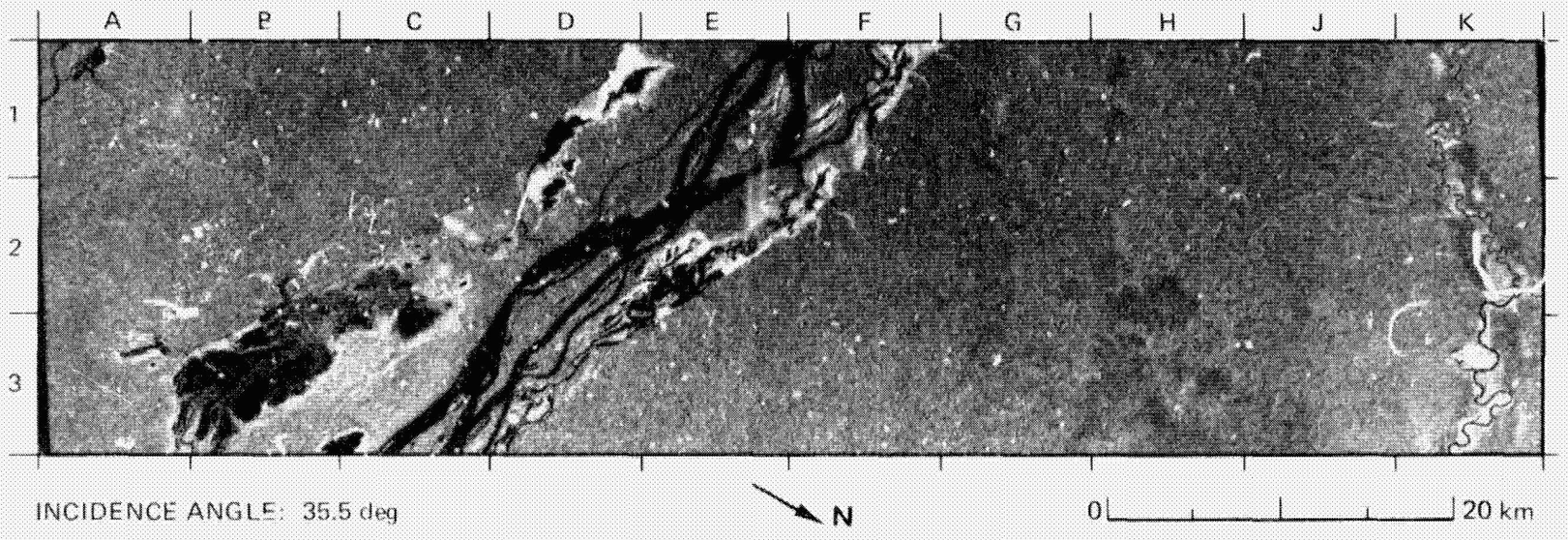


This portion of the Rio Japurá in Brazil is located 500 km east of the border between Colombia and Brazil in the north-central region of the Amazon Basin. It lies 60 km downstream of the settlement of Japurá. The river flows to the east as inferred from the orientation of the tear-drop-shaped islands.

A prominent feature in the image is the varzea (floodplain), which is approximately 12 km wide. This area of seasonal flooding is demarcated by areas of bright returns and lakes that extend from F1 to D3 on the north and from D1 to A3/B3 on the south. The bright returns (for example, D1) are areas of alluvial forest where standing water reflects the radar signal into a partially open forest canopy, which scatters the energy back to the sensor. The extent of these bright areas can be used to estimate flood stages of the river. Other wetlands with more sparse canopy are observed in the medium- to dark-gray areas between B3 and C2.

Beyond the varzea, the uniform gray tone of the generally flat tropical forest dominates. It is locally interrupted by darker areas of similar texture (for example, H1 to H3), which may be cultivated land or

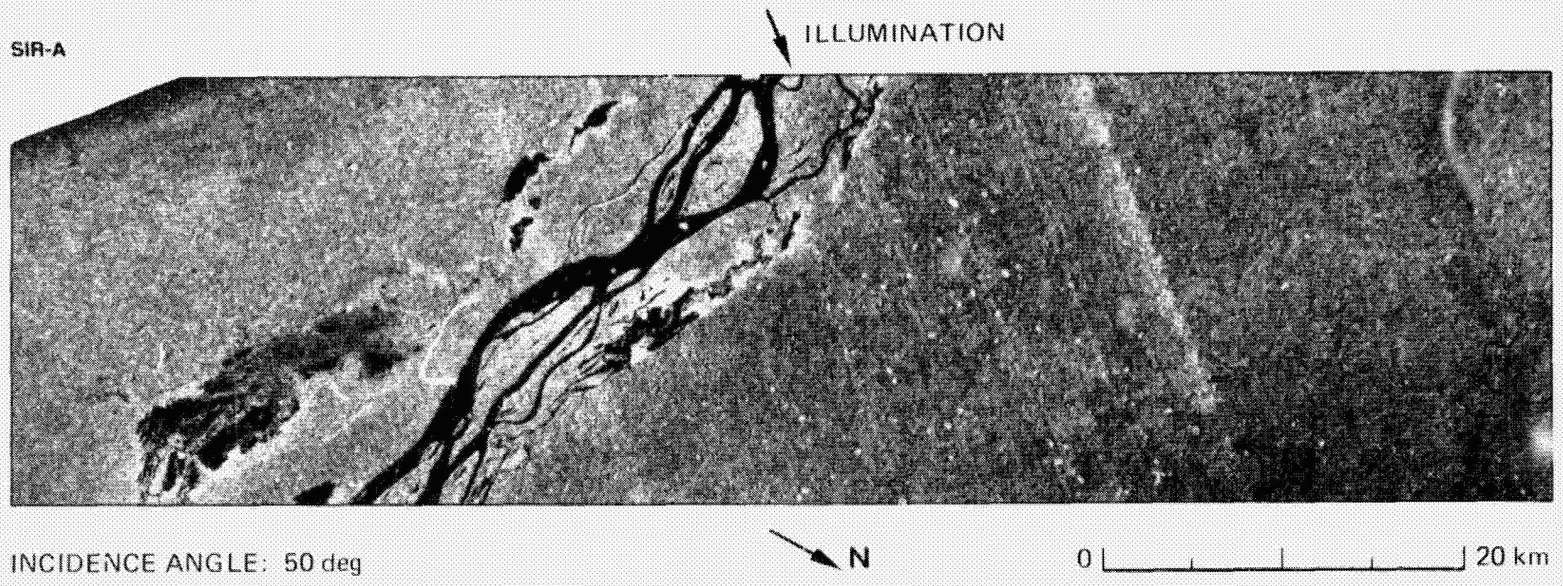


areas of less-dense natural vegetation. The angular outlines of the darker areas along the Uneiuxi River (K1 to K3) suggest cultivation patterns rather than natural vegetation differences.

On the right is a corresponding image acquired by SIR-A in November 1981. The areal extent of lakes and wetlands is greater in the SIR-B image, suggesting a higher water level in October of 1984. This agrees with the expected annual flooding cycle of the Amazon, which reaches a low point in late November. Practically no change in the course of the river is observed.

The lack of any significant topographic relief or geometric features allows a reasonable comparison of the images, although the look angles and illumination directions are slightly different. Most notable is the effect of increased resolution and dynamic range of the digital SIR-B system. This is evidenced by the fine forest structure (F3) in the SIR-B scene. Artifacts of optical processing that appear on the SIR-A image as light-toned banding parallel to the illumination direction have been removed from the SIR-B image by digital processing.

## 19. Sundarbans Mangrove Forest, Bangladesh

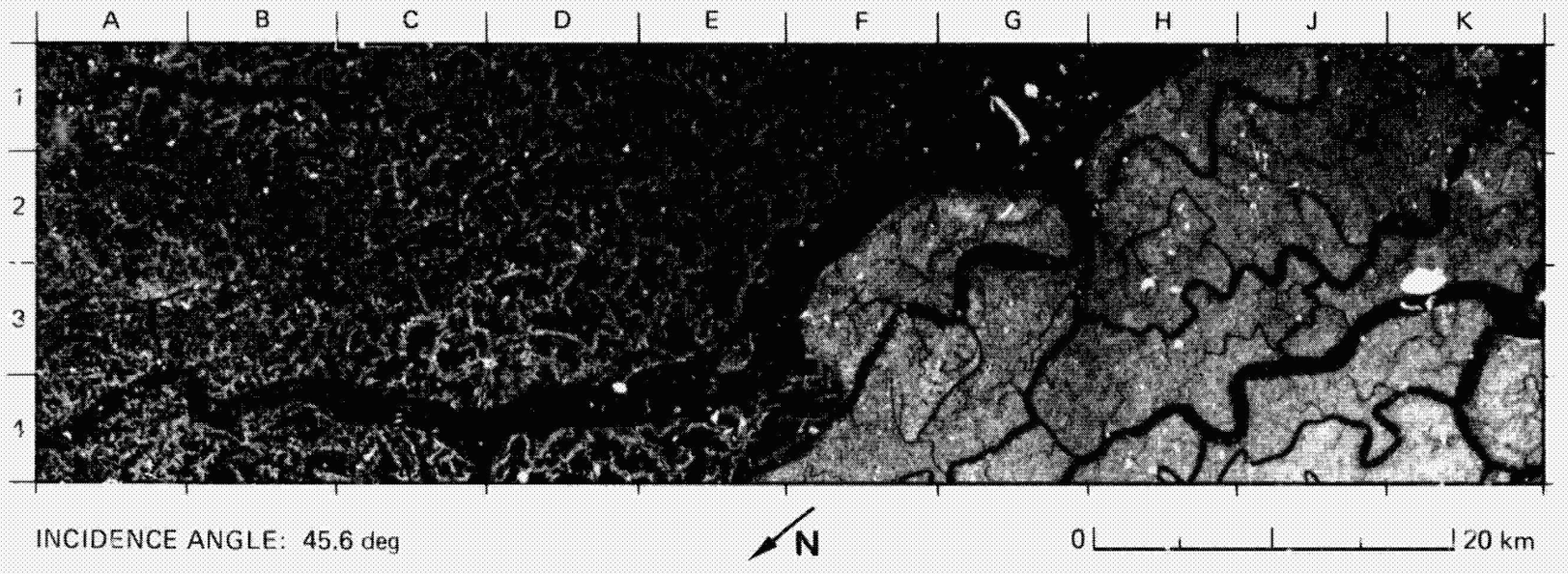


This area is about 200 km southeast of Dacca and part of the Ganges-Brahmaputra River delta. The open waters of the Bay of Bengal can be seen at K1.

The area within F4 to H1 through K1 to K4 is dominated by the uniform medium-gray tones of a Sundarbans mangrove forest reserve known as the Sarankhola Range. The dominant tree species of the Sundarbans are gewa (*Excoecaria agallocha*) and sundri (*Herietera fomes*), both evergreen obligatory halophytes that grow in mixed stands. Gewa is a soft wood used for paper-pulp production, and sundri is a valuable hardwood used in construction. The Sundarbans is also one of the world's largest Bengal tiger preserves, where the cats account for 200 fatalities each year.

Characteristic of the tidally influenced river morphology are the angular inside bends and smooth outside bends at elbows in the rivers. They are seen on the Baleswar River at B4 and on its tributaries at F3/G3, G2, and K2. Bright areas visible at G2, K2, and K3 correspond to ponded water beneath the 12.5-m-high forest canopy, which is 70 to 100% closed. Because the islands within the delta are surrounded by levees, the areal extent of standing water as revealed by the radar brightness can be used to map topograpic contours of the islands as they

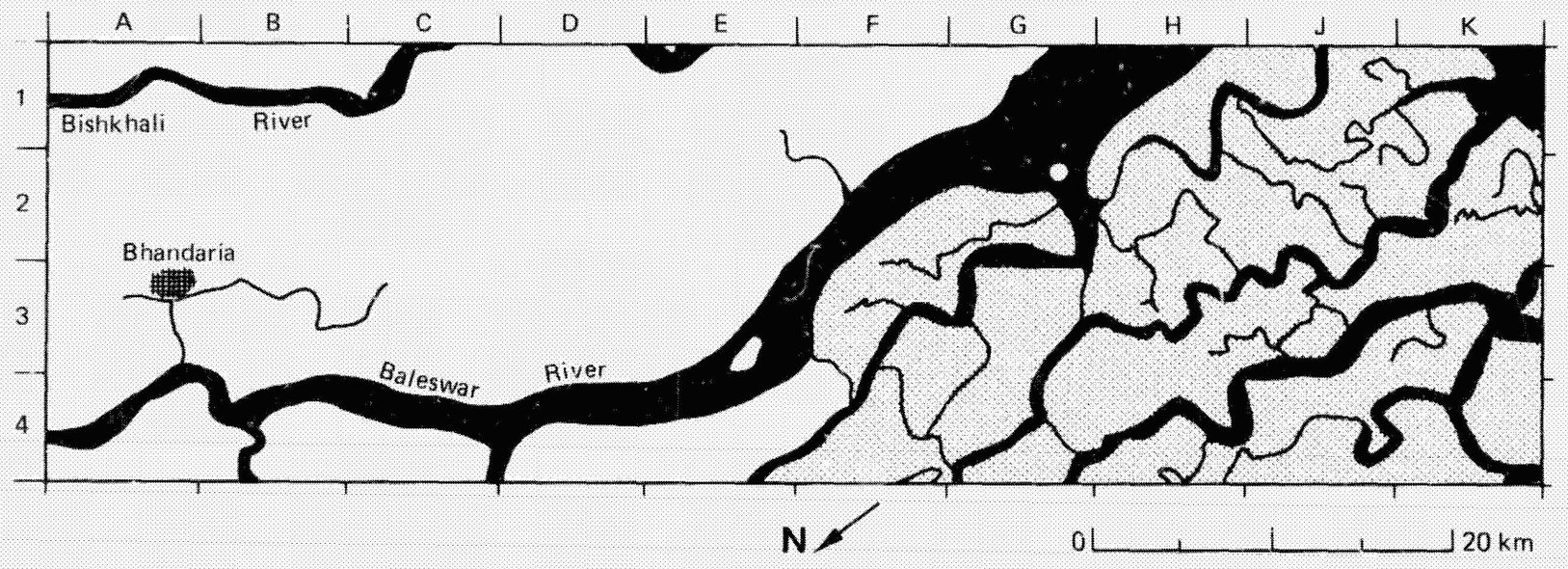


are differentially flooded through the tidal cycle. This phenomenon was observed at the three angles of incidence at which data were collected. The image shown here was acquired at about 4 a.m. local time during heavy weather.

Irrigated agricultural land with village and road networks lie within A1 to A4 through G1 to F4. The dark regions typified by areas in D3 and E1/F1 are flooded fields of rice. Irrigation takes place in cycles related to the tides and monsoons; tidal sluice gates and rainfall are used to regulate water levels. Villages such as Bhandaria (A3) and roadways are maintained on raised earthen embankments above the nominal monsoon water level. Most of the embankments are planted with shade and fruit trees and a profusion of vegetables, which contribute to the bright radar returns. Dwellings are mostly mud-walled huts with thatched roofs, although some concrete buildings with metal roofs are present. Population density in this region exceeds 300 persons/km$^2$.

(This caption was adapted from information provided by Dr. Marc Imhoff of the NASA-Goddard Space Flight Center.)

## 20. Mangrove Swamp, Exmouth Gulf, Western Australia


Nearly 75 percent of the coastlines between latitudes 25 deg north and 25 deg south are dominated by the many species known collectively as mangroves. Mangroves are terrestrial plants that have moved back to the sea, adapting themselves to life in saline water and mud; they thrive where few other terrestrial trees can live, and they create an ecosystem all their own. In a mangrove swamp, it is difficult to determine where land ends and water begins. The substrate is an ooze—a viscous liquid composed largely of organic matter.

Mangroves are found at intervals along the north coast of Australia. This SIR-B scene covers part of a mangrove swamp that extends northward for over 90 km along the east coast of Exmouth Gulf. The mangroves provide very bright radar returns from A3 to H3. At the relatively low incidence angle used in this scene, these very bright returns are probably the result of backscatter from the mangrove canopy combined with multiple reflections from the watery surface of the ooze beneath it. They form a distinctive band up to 2 km wide along the coast, following the numerous channels that wind inward from the gulf. The mangroves are flanked on the seaward side by narrow mud flats, which appear black on the image, and on the landward side by swamp, which appears dark gray. The swamp is about 6 km wide.

The swamp terminates abruptly against the coastal plain in the area from A1/A2 through J1 to H2. The plain is covered with linear sand ridges, which provide bright specular reflections at the 30-deg incidence angle used in this scene. Typically, the ridges bifurcate at small angles as seen in H1/J1. Small islands with surface textures similar to that of the coastal plain are distributed within the swamp. In addition, the boundary between the plain and the swamp is marked by broad headlands and narrow embayments, which suggest the position of a former coastline.

Eolian sands encroaching upon this possible former coastline may have provided the sediment necessary for the establishment and seaward propagation of the mangroves. Alternatively, the mangroves may have first established themselves on offshore banks where sufficient sediment was already available, and thereby promoted growth of the swamp between themselves and the mainland. Whether the mangroves are making new land or colonizing available niches, they serve to protect the coast from the winds and waves, and they provide an important habitat for other plant and animal life.

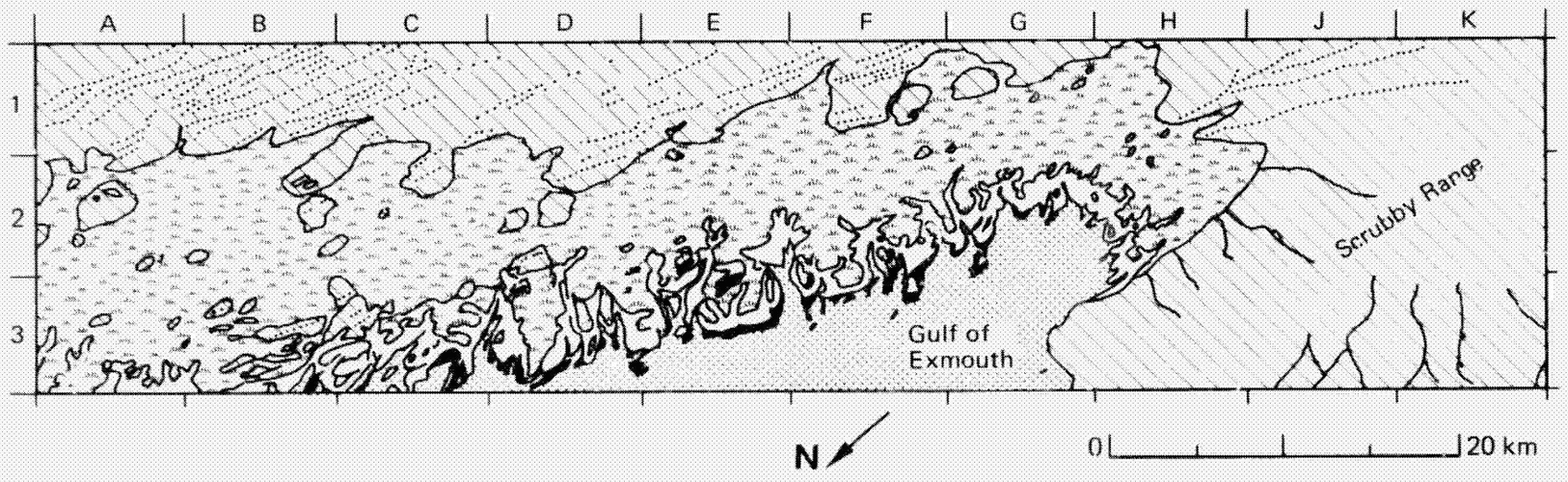


ocean

mud flats

mangroves

swamp

coastal plain showing sand ridges

## 21. Río Cisnés, Cordillera Patagónica Central, Chile

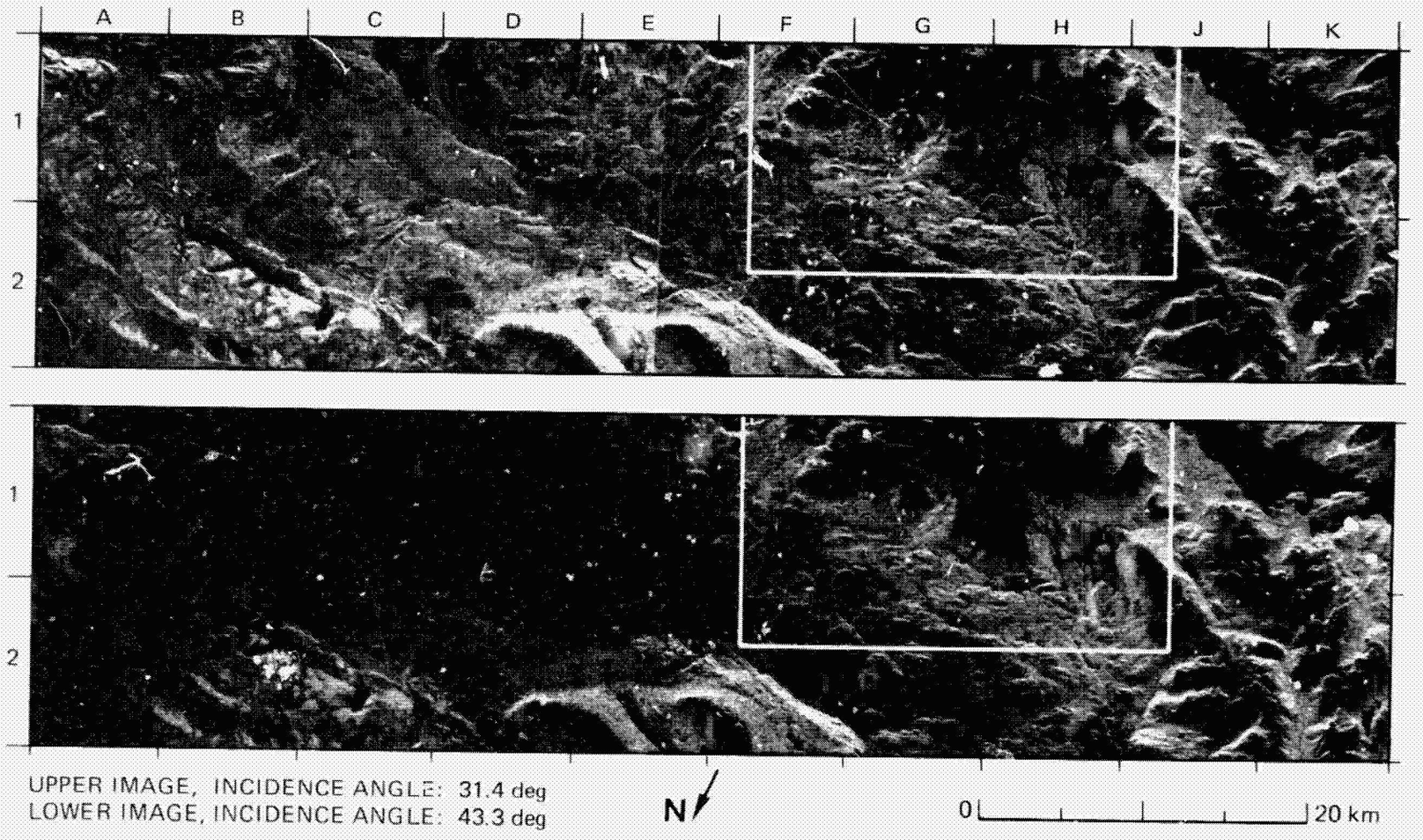

Landsat TM Band 1

N

0 20 km

ORIGINAL PAGE IS
OF POOR QUALITY

This region was imaged by SIR-B at two different incidence angles. Lago la Plata (K1) is just across the border in the Chubut Province of Argentina. Río Cisnés (C1 through G2/H2) flows to the west.

Of particular interest is the very low backscatter from F1/G1 to H1. This area is mapped as rough glacial till and therefore expected to produce relatively high backscatter. Further examination of Landsat imagery acquired about 7 weeks after the SIR-B mission indicates a snow cover over the area. Inasmuch as the SIR-B flight occurred during springtime in the southern hemisphere, snow was most likely as extensive then as at the time of the Landsat image. Snow, then, apparently reduced the normally high backscatter of the glacial-till region. This effect may be controlled by several factors, such as the moisture content and granule size of the snow; radar energy may be either specularly reflected off the smooth surface or absorbed by the snow. Reduced radar backscatter would result in either case.

Further examination of the two SIR-B images indicates that the larger incidence angle appears to have a much lower backscatter in the snow-covered region than the smaller incidence angle. To compare the effect of snow cover at the two different incidence angles, the areas outlined on the SIR-B images were specially processed to enhance the features.

This special processing shows that the image taken at the 31-deg incidence angle (figure (a)) is of high quality; there are many recognizable features in the image, possibly because no radar energy penetrated the snow. The special processing for the image taken at the 43-deg incidence angle shows a very low signal-to-noise ratio (SNR). The snow-covered region appears uniformly dark with little feature differentiation, which can be attributed to either the low SNR or a low radar backscatter from the snow.

## 22. Michinmahúida Volcano, Chiloé Province, Chile

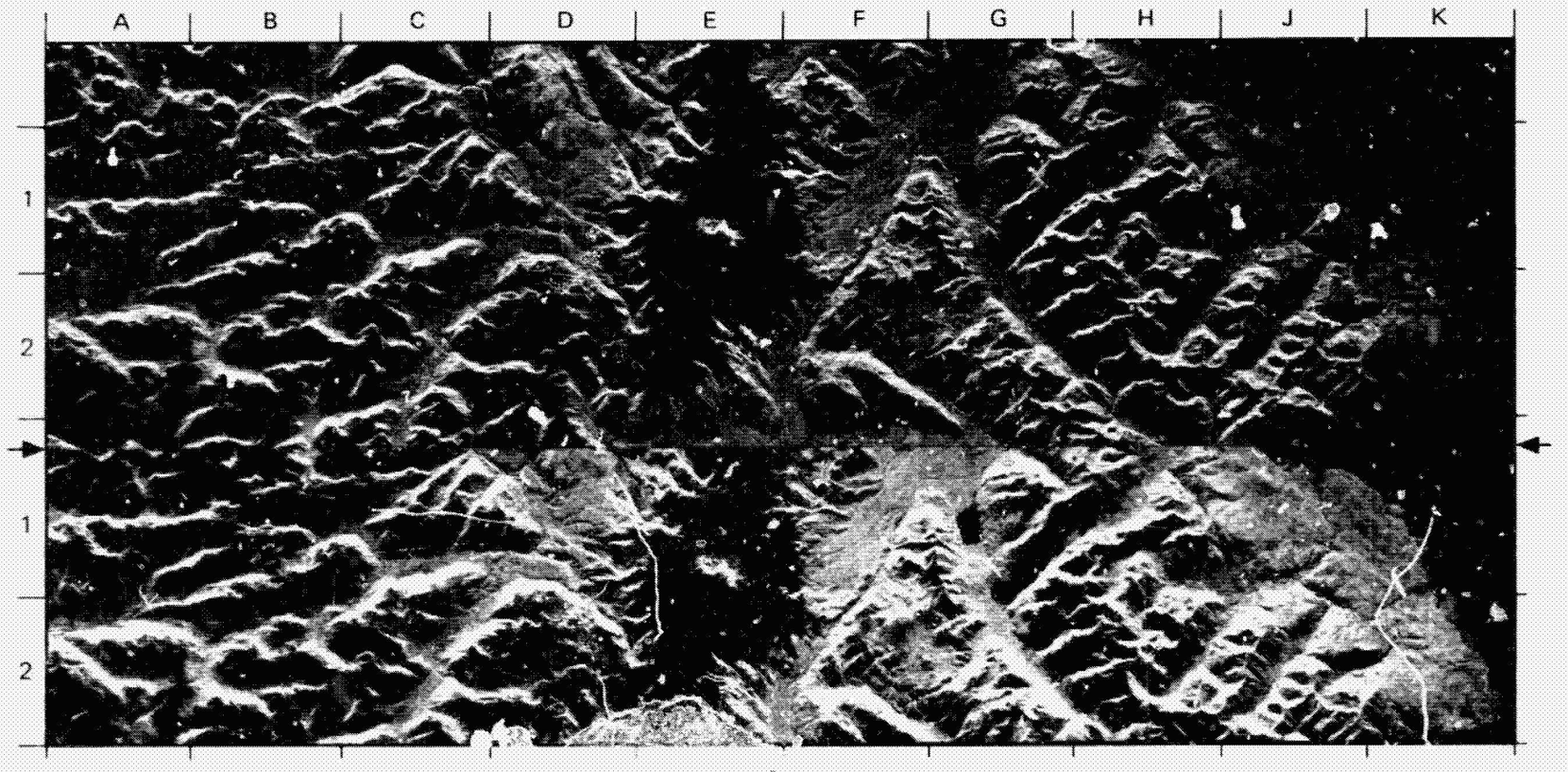


UPPER IMAGE, INCIDENCE ANGLE: 45.2 deg
LOWER IMAGE, INCIDENCE ANGLE: 53.7 deg

The active subduction of the Pacific plate below the continent of South America is evidenced by mountain building, volcanism, and earthquakes. Michinmahúida, the volcano shown at E1/E2 in this stereo pair of SIR-B images, forms part of a chain of volcanoes along the Andes Mountains; it rises 2400 m above the surrounding alluvial valleys, which are near sea level.

Michinmahúida has been active in historic times, and in 1960 this part of the Chilean coast was the site of an earthquake with the largest magnitude recorded by modern instruments: 9 on the Kanamori scale; fault displacements up to 20 m were observed.

The snow-covered slopes of the volcano appear black because of an extremely low radar return. The snow probably absorbed most of the radiated signal.

Mountain glaciers radiate from the circular crater (E1) at the peak of Michinmahúida. A notable example appears in the lower left of E1: the valley sides are characteristically steep and curvilinear, and a bright convex ridge marks the terminus of the glacier. Valleys to the north and east have been carved by a large continental ice sheet that covered the area in Pleistocene time. The linearity of the valleys suggests that their locations are controlled by faults.

These features can be more readily viewed on the images with a standard field stereoscope. The images were collected at incidence angles of 53.7 deg and 45.2 deg with same-side illumination. Although this stereo convergence angle of 8.5 deg is relatively small, the steep slopes of the volcano and the steep sides of the glaciated valleys are quite clear in the three-dimensional perspective.

(This caption was prepared from information provided by Mr. Eric Fielding of Cornell University.)

## 23. Albemarle Sound, North Carolina, U.S.A.


Albemarle Sound (E1/F1 through G3/H3) on the coast of North Carolina lies about 80 km south of Norfolk, Virginia. This scene is mostly in the Tidewater Province, a low nearly level plain composed largely of peninsular tracts divided by broad embayments that formed from engulfed river valleys. Elevations do not exceed 8 m. Much of the area is naturally subject to flooding from storms and tides, and it is poorly drained. Tupelo, gum, cypress, and Atlantic white cedar are the dominant tree species in such riverine swamps as those along the Roanoke River from H2/H3 to K4. These swamps give bright returns from the tree canopy above the standing water. Darker tones within these swamps are probably areas of marsh grasses. Hardwood and pine lowlands (E3/F3) are found in interstream divides.

Large areas of swamp have been drained through an extensive network of canals and the land converted to agricultural use (K1 and

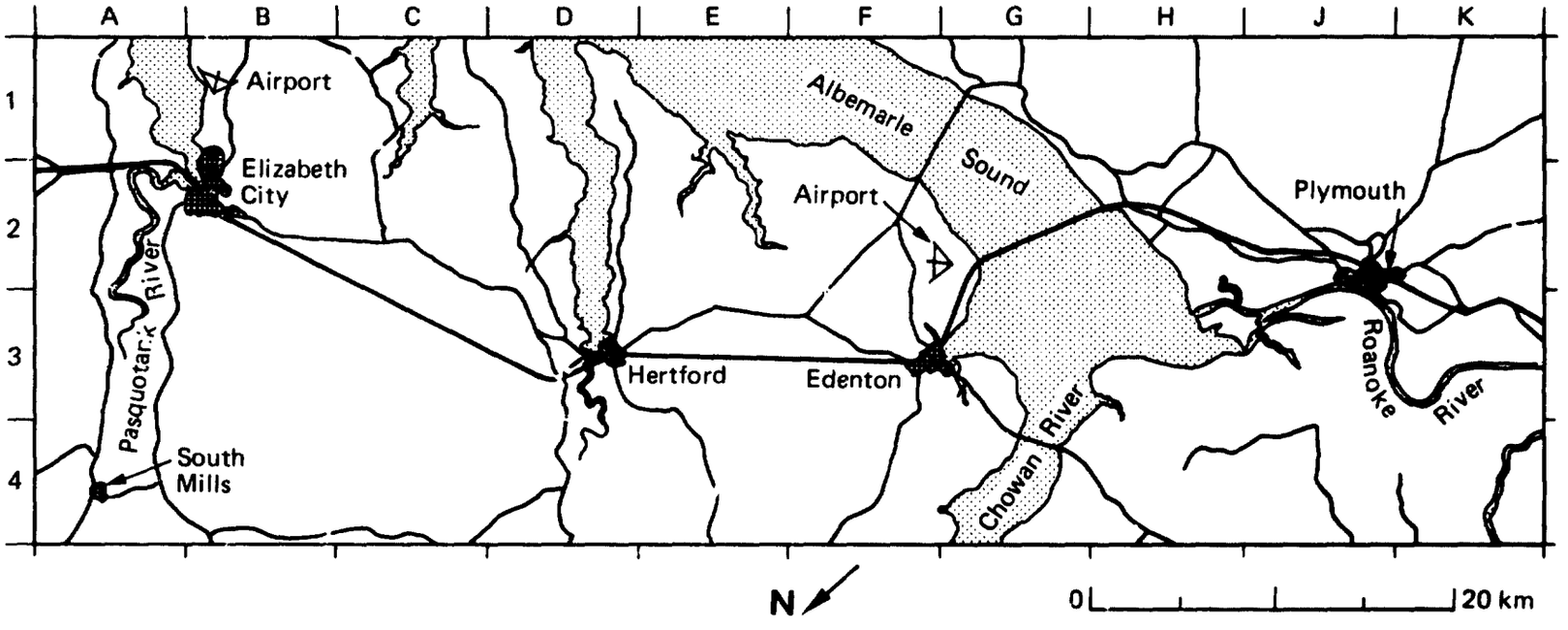


B3)—crops of mostly corn and soybeans. A portion of the Intracoastal Waterway connecting the Pasquotank River and the James River in Virginia can be seen at A3/A4. The bright linear return from D3 to F3 is the railway connecting Hertford and Edenton. The railway bridge crossing Albemarle Sound is clearly visible at G2 but the automobile crossing to the east is not, perhaps due to differing constructions or orientation.

A significant darkening is observed along the north shores of Albemarle Sound and other rivers (for example, A1, D1, E1, G1, and G3). Apparently this is a wind shadowing effect. The rougher, open water produces a brighter return than the protected downwind coastline.

(This caption was prepared from information provided by Heather M. Cheshire of the North Carolina State University.)

## (vii) Agriculture and Forest

## 24. Ocean Pond, Florida, U.S.A.

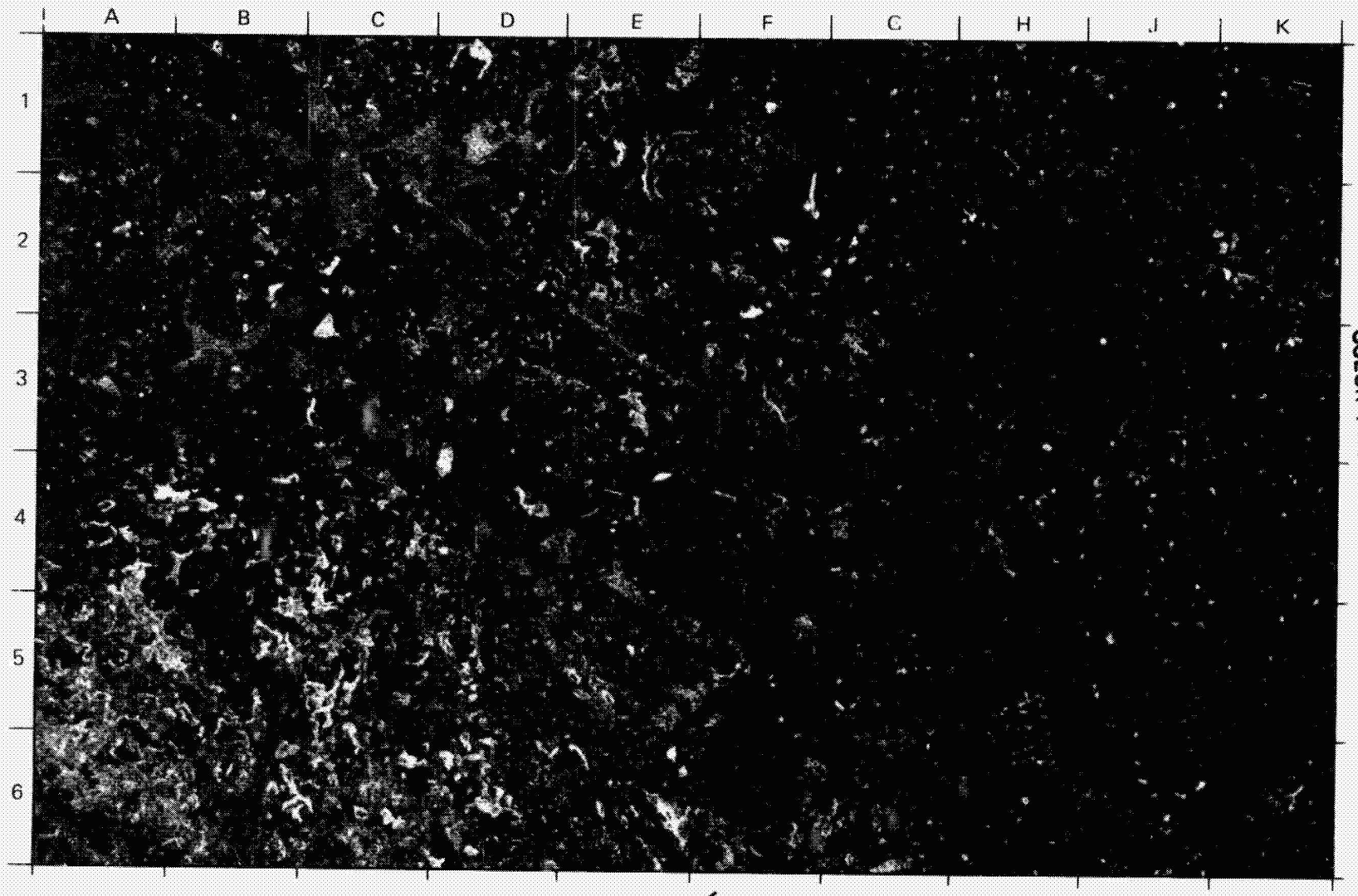


ORIGINAL PAGE
COLOR PHOTOGRAPH

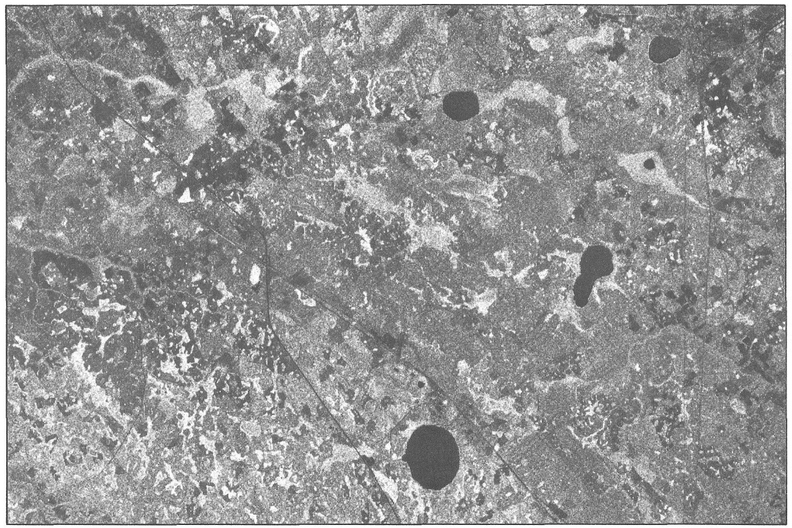

INCIDENCE ANGLE: 28.4 deg

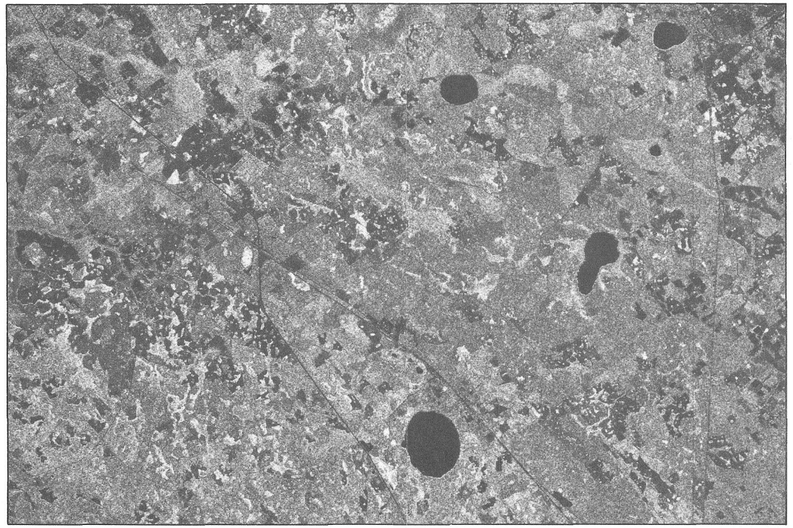

INCIDENCE ANGLE: 45.3 deg

N

0 10 km



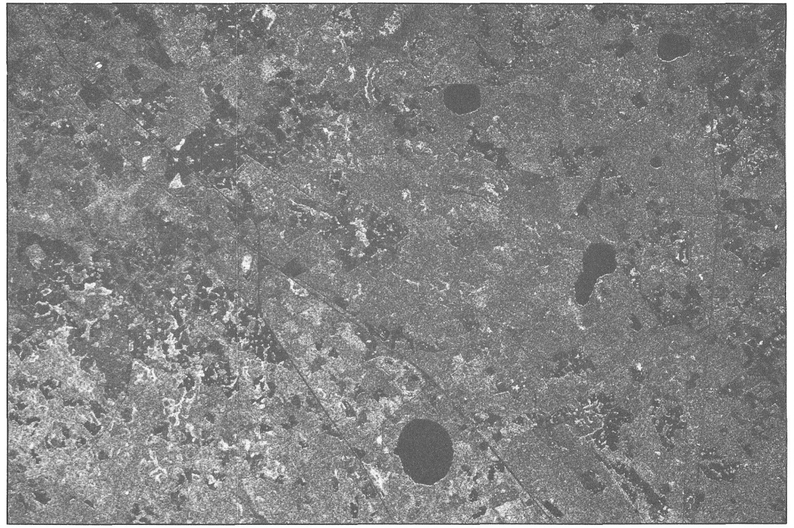

INCIDENCE ANGLE: 58.2 deg

Ocean Pond (F6), Palestine Lake (H3/H4), Swift Creek Pond (F1/F2), and Lake Butler (J1) are prominent features in this image of a forested area in northern Florida, 65 km west of Jacksonville. The terrain is flat with a mean elevation of 45 m. Mostly sandy soils overlay weathering limestone to produce the characteristic circular sinkhole lakes. Interstate Highway 10 crosses from A1 to E6 generally in parallel with a railroad grade and U.S. Highway 90 from A1 to G6. The much finer linear feature to the south extending from A1 to H6 is a power line right of way.

This color image was produced from the coregistration and combination of three separate SIR-B images, each acquired at a different incidence angle: the 58.2-deg image was assigned red, the 45.3-deg image green, and the 28.4-deg image blue. From this image, the radar brightness of an area as a function of incidence angle can be quickly assessed.

Much of the land in this scene is cultivated with plantations of slash pine, which appear generally as a uniform muddy green in such areas as E4/F4. These stands, managed for paper pulp production, are on a 25- to 30-year rotational cycle of harvest. Other areas, many of which are part of the Osceola National Forest, contain natural stands of older longleaf pine, which appear reddish (for example, B6), and native cypress-tupelo in swamps, which provide the bright-blue returns of C1/C2, E3/F3, and J2. Many of the dark returns (for example, C2 and D4/D5) are recently clear-cut areas and, in some areas (K2 through K5), farmland—pastures or newly planted fields. The small spot of pure red in A1 (produced by the largest incidence angle of 58.2 deg) was discovered to be an ornamental shrub nursery containing thousands of 25-cm-high pots of plants.

The use of multiple-angle imagery to distinguish the surface cover under forest canopy is demonstrated by comparing the returns from the cypress swamp surrounding Fisher Lake in the lower half of J2. The area is very bright in the 28.4-deg image. This small incidence angle allowed the radar signal to penetrate the partially open canopy; from there it was reflected by the standing water beneath the trees and scattered back to the sensor. At the angle of 58.2 deg, there is no distinction between the swamp and the surrounding slash pine stands; the incidence angle is too large to allow the signal to penetrate the canopy and reach the surface.

(This caption was prepared from information provided by Prof. R. M. Hoffer of Purdue University.)

## 25. Shillong Plateau, India, and Sylhet Uplands and Lowlands, Bangladesh

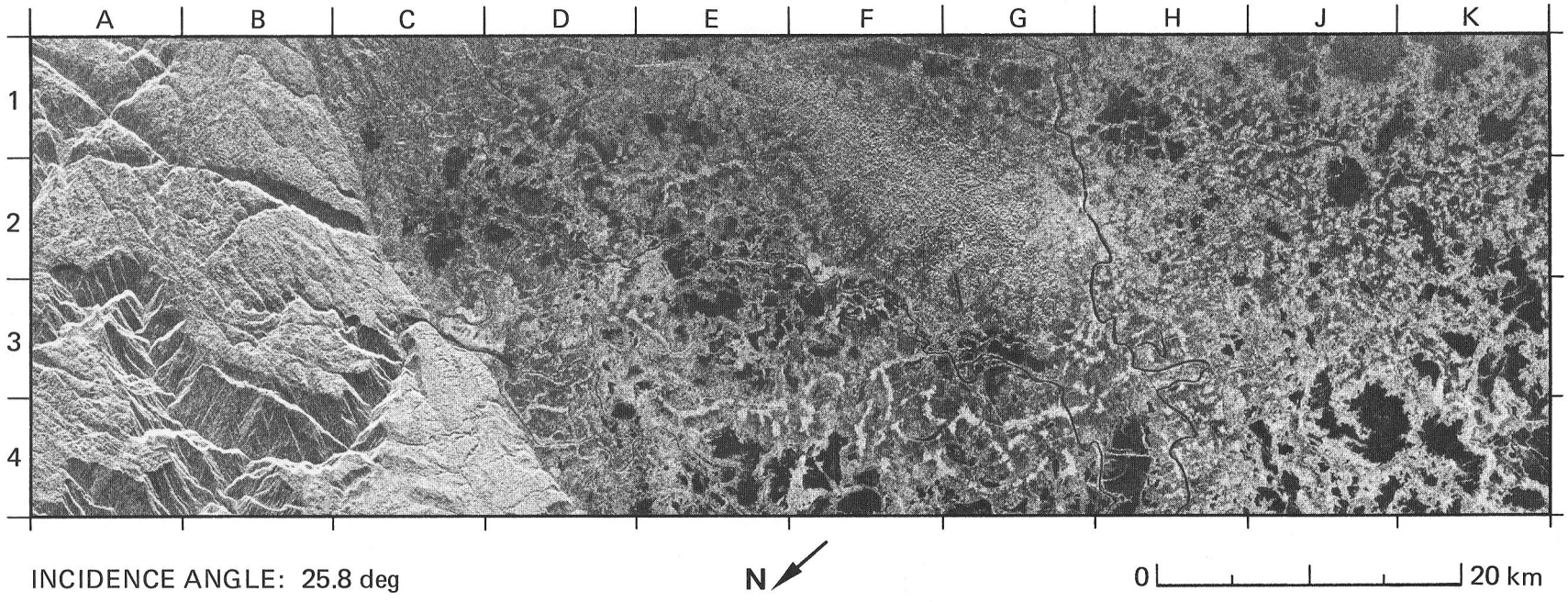




The Shillong Plateau in the Assam region of India is composed of Tertiary and Quaternary sandstones, siltstones, shales, and conglomerates that overlie Precambrian granite and gneiss. A portion of the plateau is shown in the image from A1 to B1 through A4 to C4. The plateau rises to an average elevation of about 1400 m, and it is deeply dissected by ravines that are dominantly fault controlled. Local relief reaches 800 m.

The mean annual rainfall exceeds 5000 mm, the plateau surface is largely covered with scrub and grass, and the area as a whole is undergoing regional subsidence owing to tectonic movements of the Indian subcontinent. These conditions combine to produce serious seasonal flooding in the Sylhet lowlands to the south.

The Sylhet uplands and lowlands in Bangladesh occupy the remainder of the image. The Surma River forms the major drainage of this area, and it is fed by sediment-laden runoff from the adjacent Shillong Plateau. In common with other drainages in the area, it tends to overflow and flood the adjacent countryside. Small earthen levees along the banks of the river provide bright radar responses on the image. The lowlands are characterized by a widespread distribution of lakes, some of which are permanent, and many of which are seasonal. During the monsoon season—at which time this image was obtained—the lakes are used to grow deep-water rice, jute, and water hyacinth.

A succession of plunging fold structures gives rise to uplands such as the Cherragong, which rise about 80 m above the surrounding country. Such areas support a natural cover of mixed deciduous trees and they are used for large tea plantations. This contrasted land usage results in distinctively different image texture in the area extending from E1 to G2.

The town of Sylhet is the largest settlement in the area. It is a major center for the production of tea, rice, cattle, and some jute. Numerous villages built on embankments for protection against flooding appear very bright on the image. A network of roads and other transportation routes is readily perceived from the bright linear trends in the lowlands. Many of the routeways are built on embankments and locally flanked by habitations.

(The caption was adapted from information provided by Dr. Marc Imhoff of the NASA–Goddard Space Flight Center.)

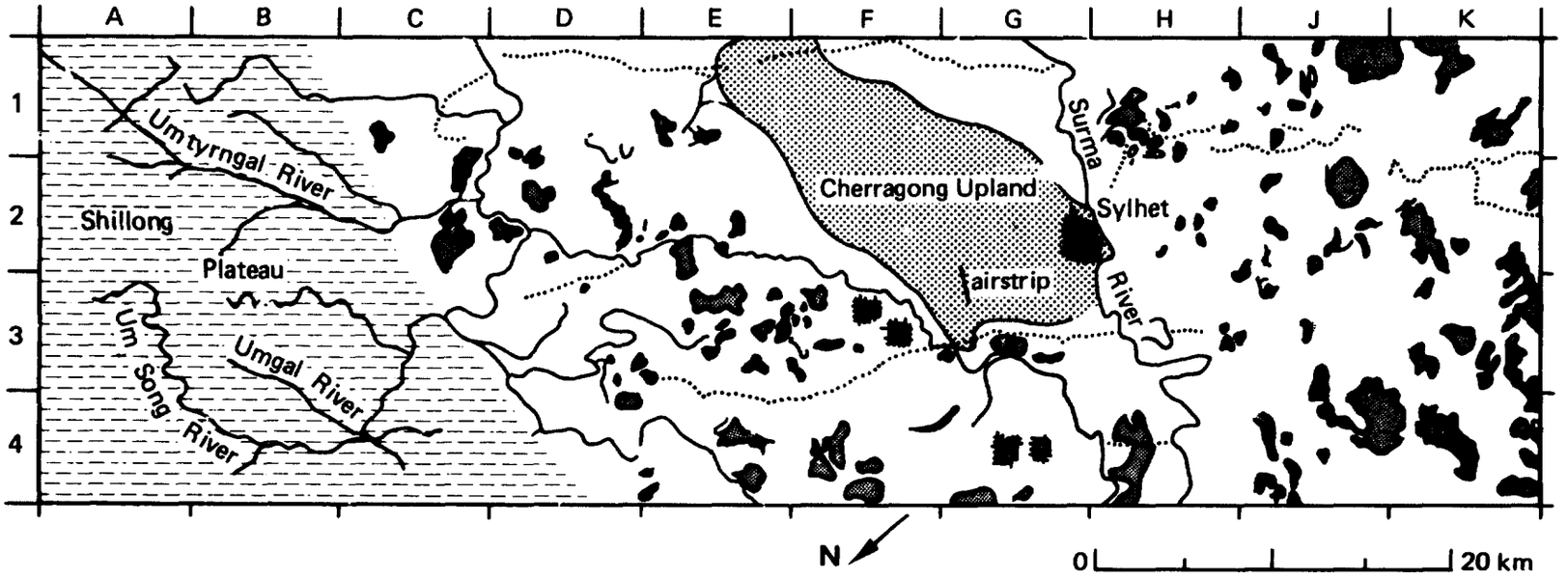


lake

habitation

roadway

## 26. Cordón la Grasa, Chubut Province, Argentina

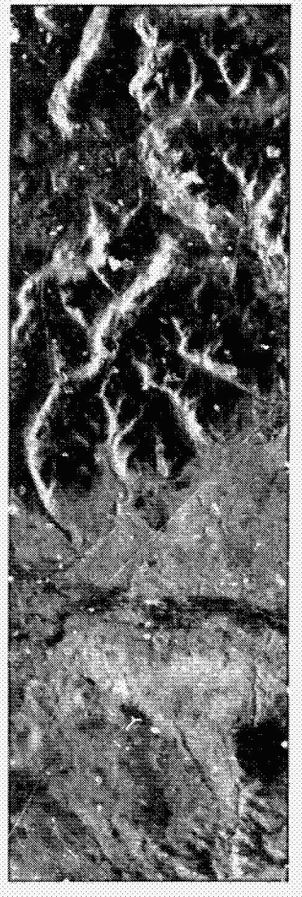

INCIDENCE
ANGLE: 33.0 deg

INCIDENCE
ANGLE: 44.7 deg

INCIDENCE
ANGLE: 53.7 deg

INCIDENCE
ANGLE: 59.4 deg

ILLUMINATION

N

0 20 km

ORIGINAL PAGE IS
OF POOR QUALITY

These four images are a portion of a descending multiple-incidence-angle data set acquired by SIR-B near the border between Argentina and Chile, just east of the Andes Mountains. The prominent features (see map) are the Valle Frío and Cordón la Grasa, a lower elevation mountain, the peak of which was snow covered at the time of the SIR-B mission.

The vegetation is transitional from the closed forests of the Andes to the dry grasslands of central Argentina; this transition zone is a complex mosaic of several deciduous and evergreen forest communities, grasslands, semiarid steppe associations, prairies, and bogs. The vegetation types in this area of coincident coverage are governed primarily by elevation and rainfall.

The vegetation community at the highest elevation is a deciduous forest of lenga (*Nothofagus pumilio*) (Brandani et al., 1984). These trees have horizontal branches that radiate from the trunk at several distinct levels. The trees had shed their leaves by the time of the SIR-B mission. Below the canopy, dead trees and branches accumulated over years litter the ground.

The lower-elevation forest community west of Cordón la Grasa extends to the Valle Frío; it is a mixed forest composed primarily of ñire (*Nothofagus antarctica*). In general, ñire is shorter than lenga, and it has a more random branch structure; during the mission, it had no leaves. To the south and east of Cordón la Grasa, the vegetation community is also ñire, but with a different structure and mixture of other tree species.

The intensity of the four SIR-B images is relatively uniform except in the region of the high-elevation lenga forest. This forest is readily distinguished from the adjacent lower-elevation forests in the low- and medium-incidence-angle images; however, in the highest-incidence-angle image, the distinction is minimal. This may be due to a strong, horizontally polarized signal return from the dead trees and branches on the ground. At the highest incidence angle, the radar loses its ability to penetrate the canopy.

The color composite of the images obtained at incidence angles of 33.0 deg (blue), 53.7 deg (green), and 59.1 deg (red) shows the high-elevation lenga forest displayed in blue. This indicates stronger returns at the lower incidence angle, as expected. The ñire forest to the south and east is displayed in darker blue-green, which indicates a relatively equal backscatter at the low and medium incidence angles, both of which produce backscatter stronger than the backscatter at the highest incidence angle. The ñire forest on the west slopes of Cordón la Grasa is displayed mostly in red, indicating stronger returns at the higher incidence angles. A more subtle structural difference in the two ñire canopies results in two significantly different backscatter curves.

Although relative brightness could be modified by variations in the radar transmitted power, the color-composite image indicates a strong variation in brightness as a function of incidence angle for the high-elevation lenga forest and the lower-elevation ñire forests.

(This caption was adapted from information provided by Dr. Aldo Brandani of the University of Mar del Plata, Mar del Plata, Argentina, and Dr. Jorge Rabassa of the University of Comahue, Neuquén, Argentina.)

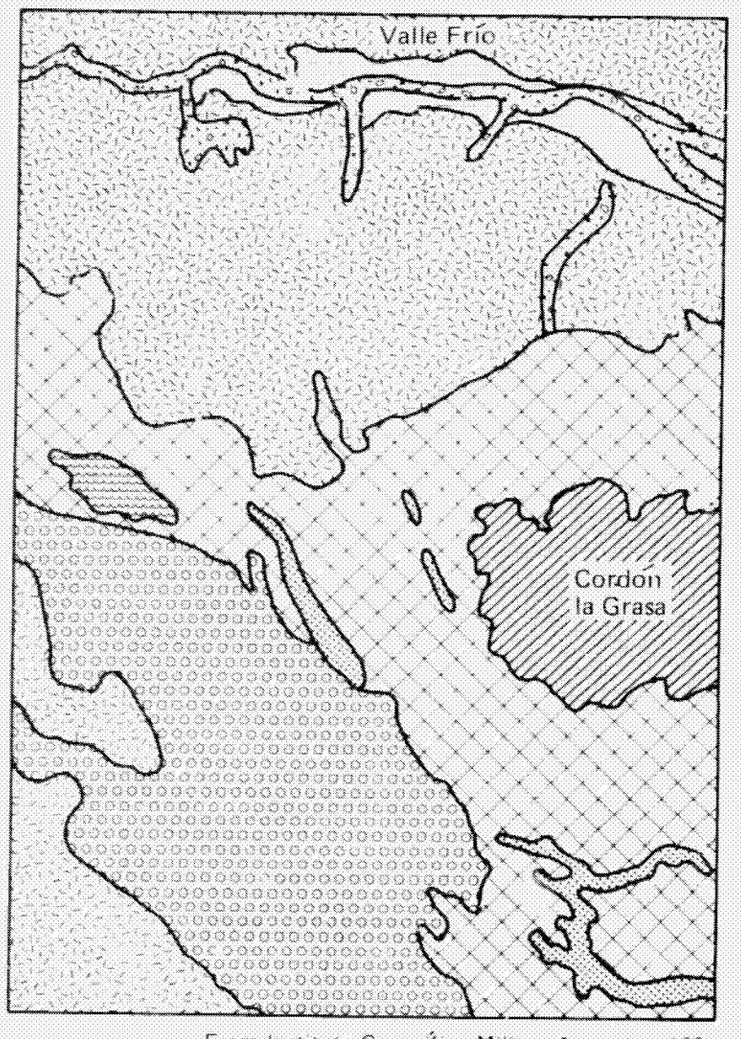


From Instituto Geográfico Militar, Argentina, 1981

snow and bare soil
lenga forests
mallínes (grasslands)
grazed mallín
ñire forests
low ñire forests
grasslands and alluvial valley
willows

N

0 5 km

INCIDENCE ANGLE: 33.0 deg
INCIDENCE ANGLE: 53.7 deg
INCIDENCE ANGLE: 59.4 deg

ORIGINAL PAGE
COLOR PHOTOGRAPH

# 27. Gravel Terrace and Alluvial Plain, Chubut Province, Argentina

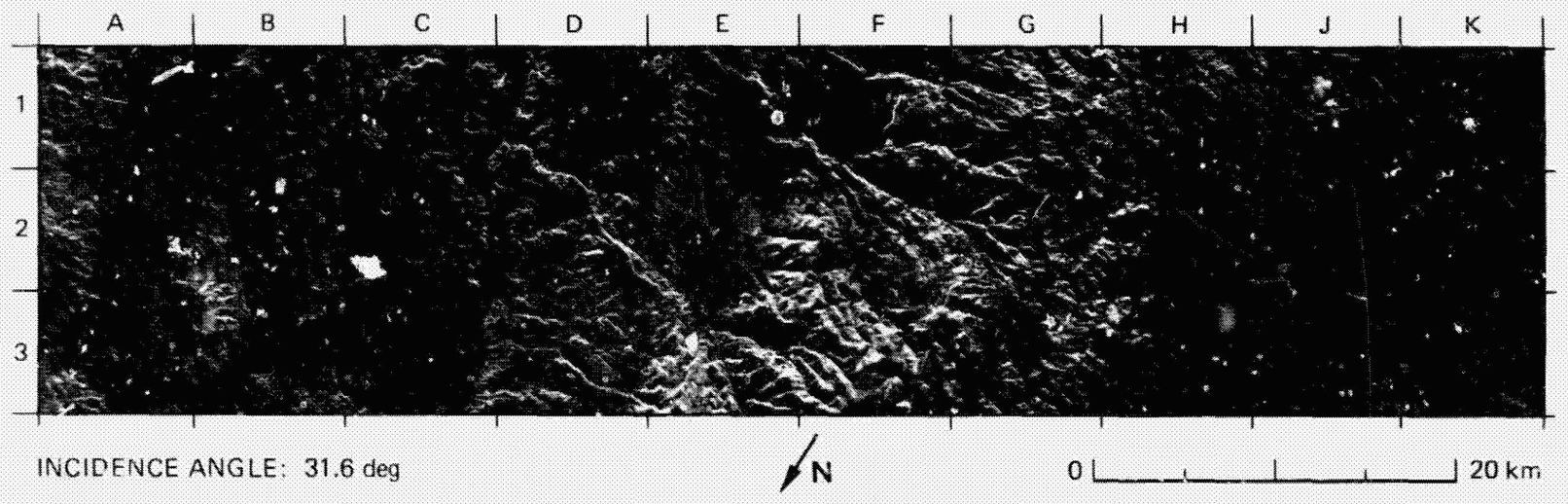




A striking feature of the Patagonian Desert of southern Argentina is the apparent uniformity of the vegetation from west to east. From the Andean Pre-Cordillera eastward to the Atlantic Coast the rainfall is uniformly low and the environment is very arid. This is conducive to the growth of low shrubs and grasses. In examining the SIR-B images acquired over southern Argentina, it is difficult to account for the strong difference in brightness between two topographically smooth vegetated surfaces – those of a gravel terrace and an alluvial plain.

The gravel terrace at E2 shows the characteristics of a coarse-grained surface. Bright dots alternate with dark ones and bright linear traces are oriented in a northwest-southeast direction. The terrace has been dissected by the tributaries of the Chubut River, leaving large northwest-southeast oriented interfluvial areas that are covered by alluvial gravels of diverse composition.

By contrast, the alluvial plain from J1 to K1 through H3 to K3 appears as a dark, relatively homogenous surface transected from west to east by several bright linear features. The plain is a typical "pampa" – a flat unit formed by a continuous deep layer of finer alluvial and eolian sediments.

Major differences between the gravel terrace and the alluvial plain seen on the SIR-B image probably result from differences in vegetation. The SIR-B image was acquired in springtime (October), when temperature and soil moisture encourage active plant growth. At this time the differences in leaf and stem production among different species of plants is greater than at any other period of the year.

The vegetation on the gravel terrace (figure (a)) is a steppe community. It contains 1.5- to 2-m shrubs, 0.5- to 1-m shrubs and herbs, and a 5- to 50-cm-high herbaceous layer. In general, the branching structure


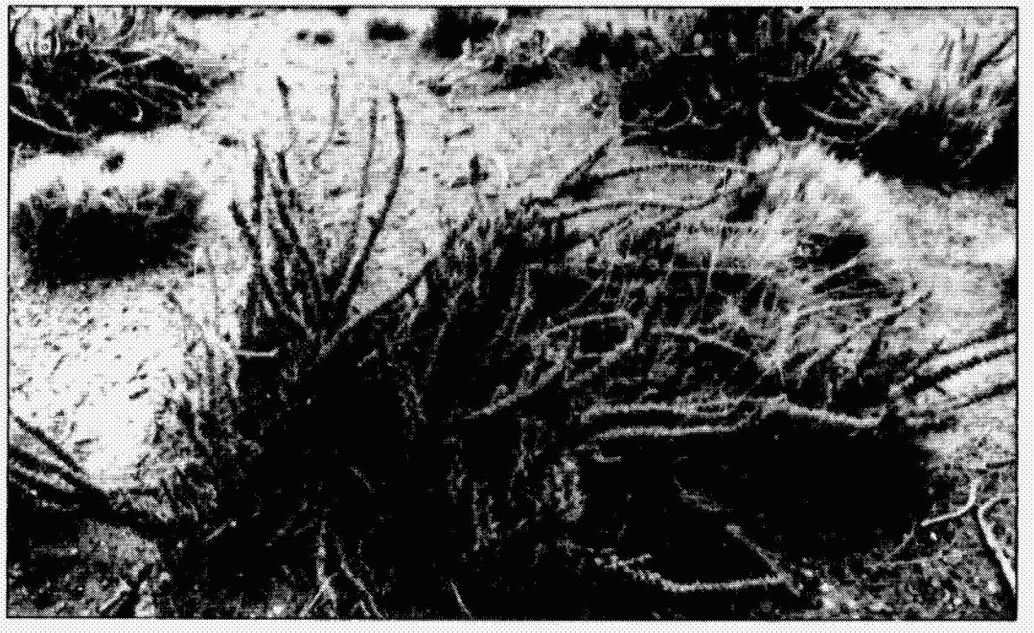


of the shrubs is randomly oriented. Vegetation patchiness in the gravel terrace might be a leading cause of the coarse-grained pattern registered in the SIR-B image, where bright dots indicate the presence of tall shrubs in areas of abundant vegetation, and darker zones correspond to sites of the lower two-plant strata.

Vegetation in the alluvial plain consists of a 1.5-m tall shrub layer and a stratum of short (about 50 cm) shrubs and herbs. The branch structure of the shrubs is generally vertical (figure (b)). The darker aspect and finer grain of the alluvial plain on the SIR-B image is likely the consequence of reduced plant cover (more denuded soil directly exposed), the lack of tall shrubs, and the morphological structure of the plants—vertical branching, and small leaves and spines—all of which diminish radar backscattering. Additional support for this interpretation is the fact that bright lines registered by SIR-B in the alluvial plain correspond to the locations of riparian vegetation (willows and related species in full leaf, 2 to 5 m tall); these areas are in contrast to the extreme aridity of the remaining ecosystem.

(This caption was adapted from information provided by Dr. Aldo Brandani of the University of Mar del Plata, Mar del Plata, Argentina, and Dr. Jorge Rabassa of the University of Comahue, Neuquén, Argentina.)



C-2

## 28. Agricultural Development, Sumatra, Indonesia

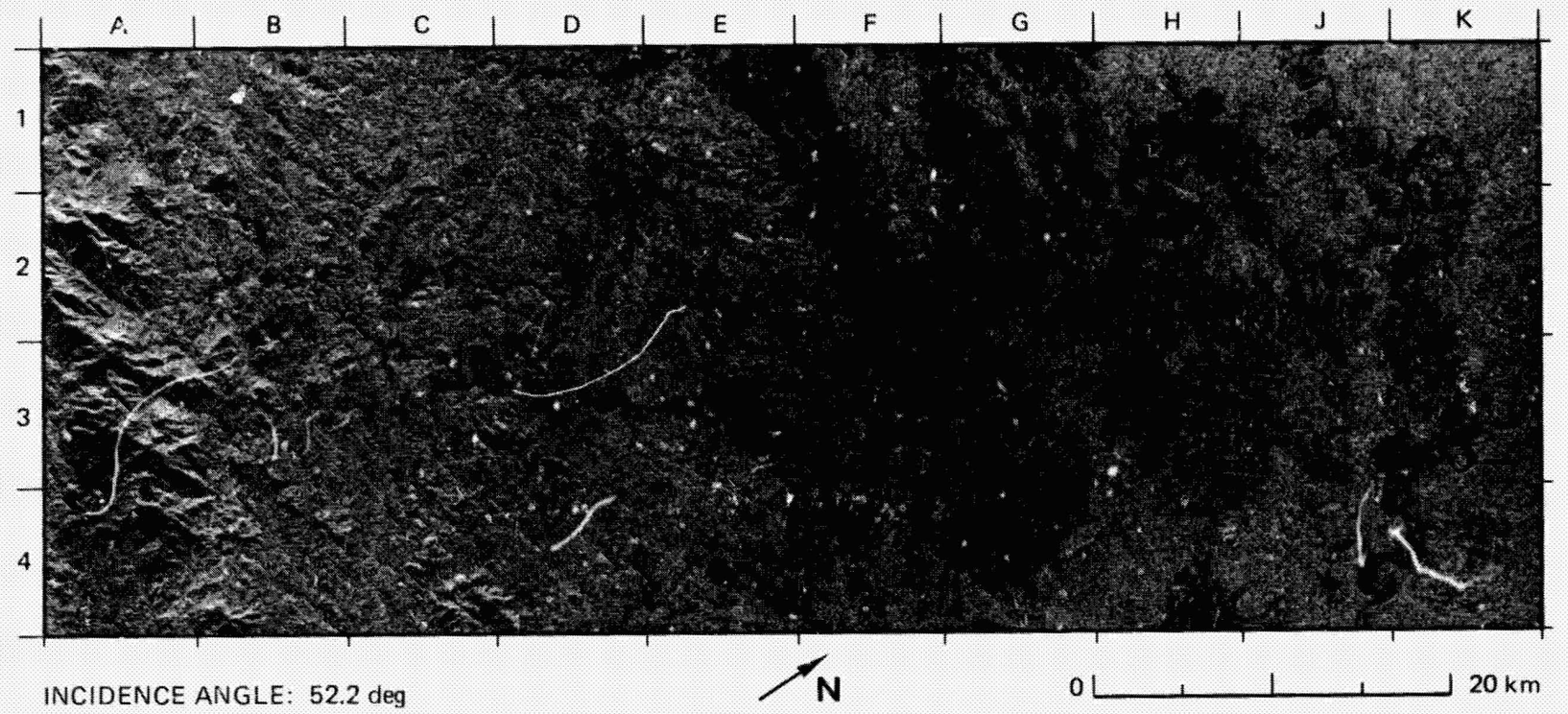




This SIR-B image shows forested terrain from the north slopes of the Barisan Mountains (A1 to A4), which rise to about 1200 m, to broad lowlands (from E1 to K1 through E4 to K4) at an average elevation of about 60 m. The Barisan mountains in the scene consist mostly of granites of Carboniferous to Jurassic age (Rosidi et al., 1976). The image shows a conjugate set of linear features formed by joints or faults in the mountains. The lowlands are underlain by gently dipping clastic sedimentary rocks with interbedded tuffs and pumice of Tertiary and Quaternary age (Simandjuntak et al., 1981). The Hari River (J1 to J4) and such tributaries as the Bungo (A1 to F4) and Tebo (E1 to F4) Rivers provide drainage to the southeast.

From the foothills through the lowlands (D1 to K1 through D4 to K4) the image covers part of the Rimbobujang Transmigration Area Development. This is one of numerous areas in the lesser populated parts of Indonesia that have been settled and cleared for agricultural development by government sponsored immigrants from more densely populated regions.

Very bright radar returns at various locations along the river banks are settlements; an example is in the upper portion of E1 on the Tebo River. Corrugated sheet metal is used extensively for roofing material in the towns. The corrugations have a wavelength of about 7.5 cm, which is approximately one-third of the radar wavelength; small

**Landsat MSS Band 7**

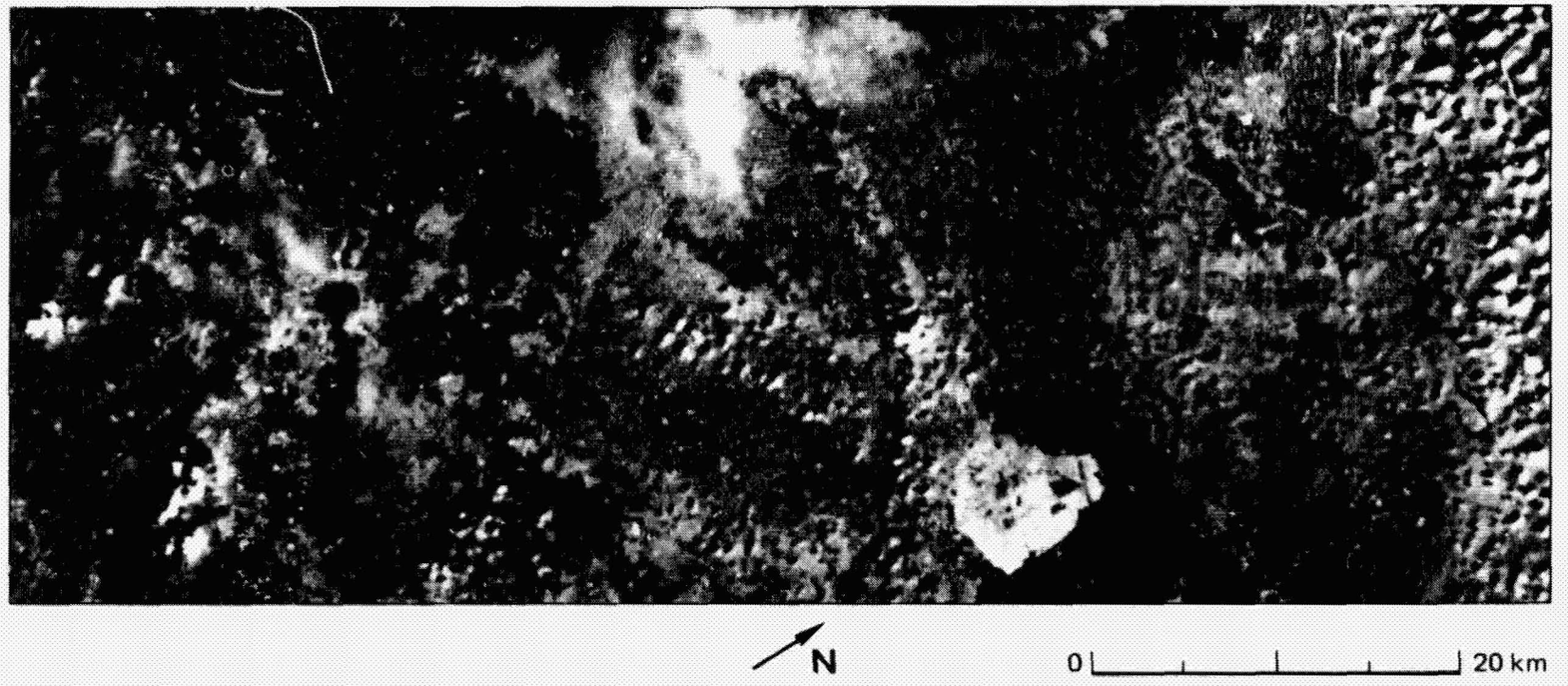




clusters of buildings roofed with this material form bright radar targets. The largest settlement is at the junction of the Bungo and the Tebo Rivers (F4). This is Muarabungo, the district administrative center. Parallel linear rows of bright radar returns in the lowland from F2 to J2 and at H3/J3 represent newer settlements in the agricultural development area.

Patterns of forest clearing and agricultural development are outlined in medium gray tones on the SIR-B image. Rice, palm oil, fruit, and cloves are the crops. Nipah palms line the banks of the rivers in swampy areas. On the corresponding Landsat MSS image in the near-infrared wavelength, the cultivated areas are brighter than the uncleared forest. Recently cleared land at G3/G4, which shows low radar backscatter on the SIR-B image, is strongly reflective on the near-IR image. Areas of open wetland adjacent to the rivers appear dark on both images.

(This caption was prepared from information provided by Prof. J. Rais of the National Agency for Surveys and Mapping, Cibinong-Bogor, Indonesia, and by Dr. R. Sukamto, Geological Research and Development Centre, Bandung, Indonesia. The Landsat MSS image was provided by Dr. Wiranto Arismunandar of the Indonesian National Institute for Aeronautics and Space.)

## 29. Macomb, Illinois, U.S.A.

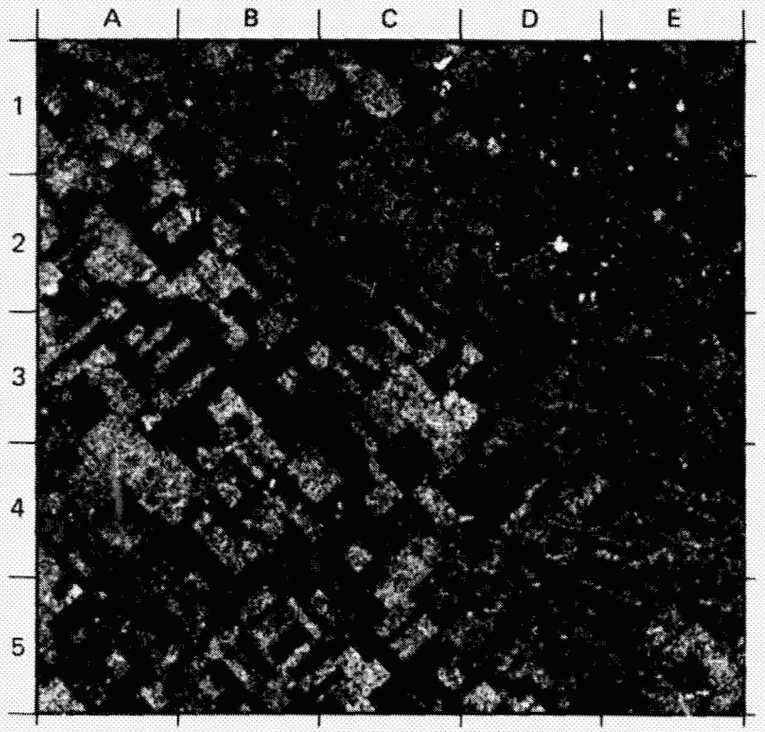


ILLUMINATION ↑

INCIDENCE ANGLE: 31.4 deg

Airborne SAR

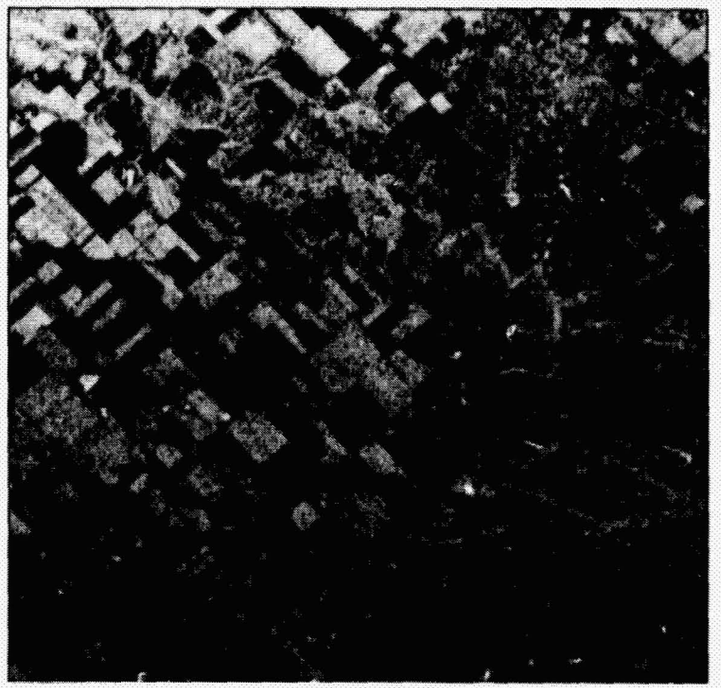

ILLUMINATION ↓

N

0 5 km

The imaged area is a largely agricultural region in Mc Donough County, west-central Illinois. The city of Macomb (D1 through D2) with a population of 20,000 is characterized by a medium-gray return with scattered specular reflectors, which include some of the larger buildings of Western Illinois University at D2 and the County Courthouse in the central square of the town. Spring Lake (D4 through E5) is a man-made recreational area. The East Fork of the La Moine River (A1 through E3) runs southwest to the illinois River It is manifest chiefly because of the mottled gray returns of the vegetated river valley; no open water is visible.

The agricultural field pattern in the northern portion of the image is generally laid out in a ½-mile grid system. Approximately 90% of the acreage is evenly divided between corn and soybeans, both of which were undergoing active harvest at the time of data acquisition. Unharvested corn fields yielded the brighter returns, harvested corn produced an intermediate return, and the darkest returns were from soybeans in various stages of harvest. The level of backscattered return is, in general, proportional to soil moisture, surface roughness, and vegetation biomass.

Compared here with the SIR-B image, which was collected on October 11, 1985, is the same area imaged by the JPL aircraft SAR on October 10 and by Landsat TM (band 4) on October 29. Both radar images are L-band and HH polarized. The SIR-B and TM scenes have approximately 30-m resolution; the aircraft image has about 11-m reso-

Landsat TM Band 4

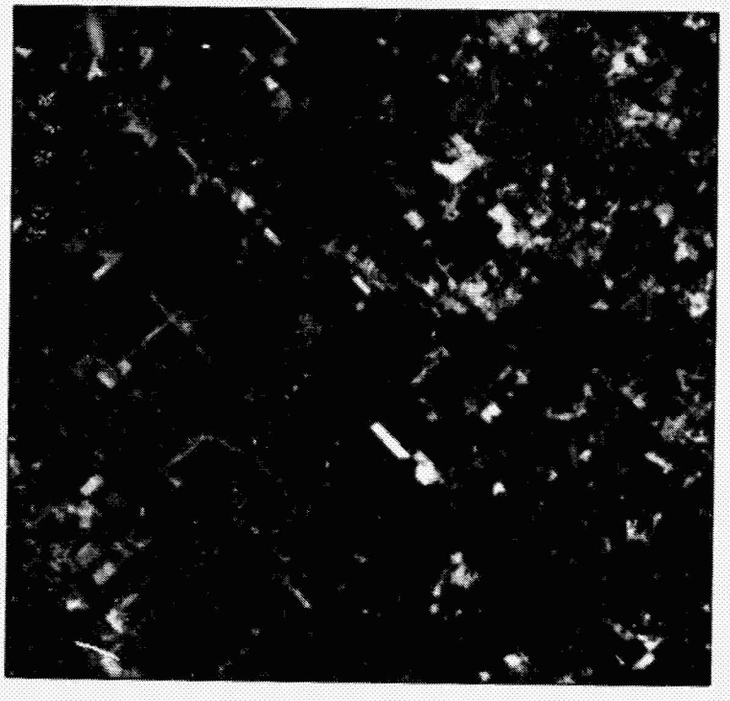

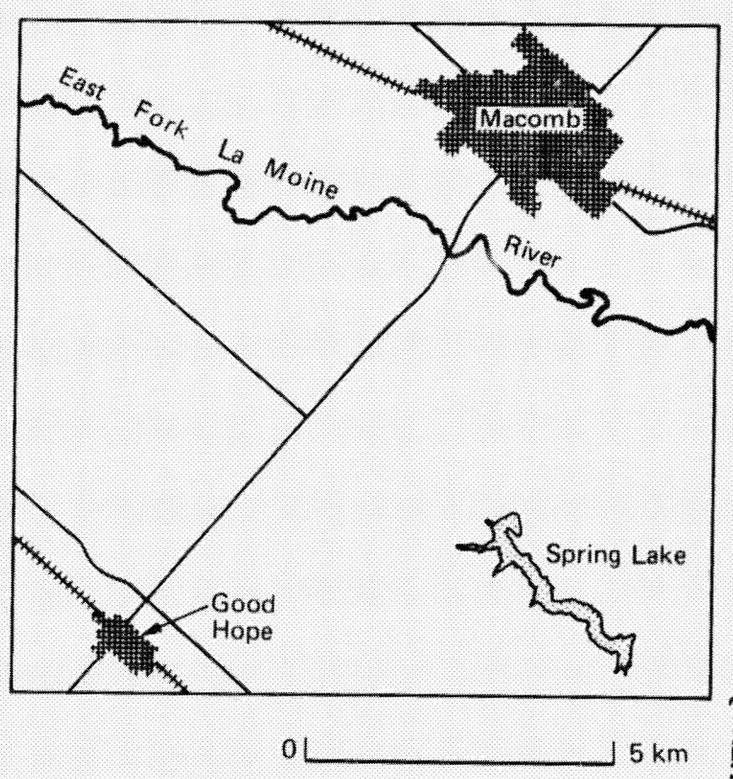




lution in the far range. Although the SIR-B image has lower resolution and dynamic range than the aircraft data, which were collected at an altitude of 10 km, the qualitative identification of features in the two images compares very well. Notice the gradation of resolution and image tone across the aircraft scene, a result of the change in incidence angle from 18 to 54 deg. No such gradation exists in the SIR-B image because of the high altitude of the sensor. Note also the corn field (arrow) at C4 which appears bright in the aircraft image but dark a day later on the SIR-B image—apparently a result of the harvest. The TM scene shows a markedly different field pattern, a result of the continuing harvest and differing albedos of the surface at infrared wavelengths.

(This caption was prepared from information provided by Mr. M. Craig Dobson of the University of Michigan.)

## (viii) Urban Areas

## 30. Montreal, Province of Quebec, Canada

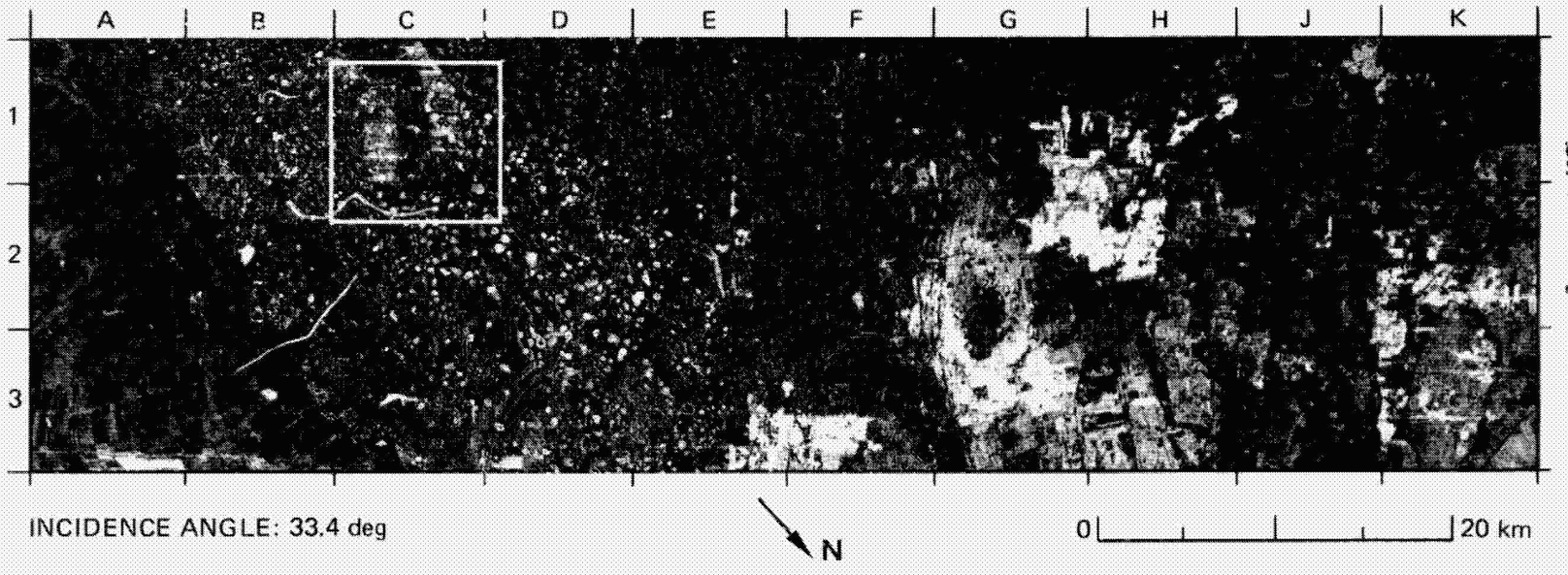




Built-up areas between the St. Lawrence River and the Rivière des Prairies in the city of Montreal (G1/H1 to G3/H3) show different levels of radar backscatter due mostly to directional effects. City blocks oriented normal to the radar illumination (parallel to the flight path) appear very bright (G2/H2). Blocks inclined by more than about 10 deg to the radar illumination appear notably darker (lower portion of G3).

In contrast to Montreal, the towns of St. Jean and Iberville (B3/C3), on opposite banks of the Richelieu River, show little effect on the levels of backscatter. Because the network of streets and blocks in these towns is highly inclined relative to the direction of radar illumination, the built-up areas yield comparatively low backscatter and appear dark on the image.

Mount Royal, the feature from which the city takes its name, is visible as a dark elliptical area just west of a wide bend in the St. Lawrence River (G2/G3). The St. Lawrence Seaway is the narrow black strip south of the main river channel in the vicinity of Heron Island and Lachine Rapids (F1/F2).

Directional effects influence the radar backscatter from cultivated fields, as well. Two groups of fields with drainage ditches oriented parallel to the flight path appear bright in the area outlined on the SIR-B image (C1). The ditches are more clearly displayed on the corresponding airborne SAR coverage of this area, shown here at a scale larger than that of the SIR-B. The airborne image was acquired by the Canada Centre for Remote Sensing 18 days after the SIR-B image, using a sensor with similar wavelength, polarization, illumination direction, and flight path, but with a 3-m spatial resolution, which is higher than that of the SIR-B image.

At the times both images were acquired, some fields in the area contained rows of standing corn and some contained corn stubble. The direction of these rows again influenced the level of radar backscatter. For example, in the area between the two groups of fields outlined on the SIR-B image, there is a small bright triangular area where uncut corn was oriented in rows parallel to the flight path; this area is indicated by an arrow on the airborne image. Adjacent to this area, where the corn rows are inclined by 13 deg to the flight path, the backscatter is notably reduced.

(The airborne SAR image and the technical analysis upon which this caption is based were provided by Dr. Lawrence Gray, Canada Centre for Remote Sensing.)

Airborne SAR

## 31. Nagoya Industrial District, Central Honshu, Japan

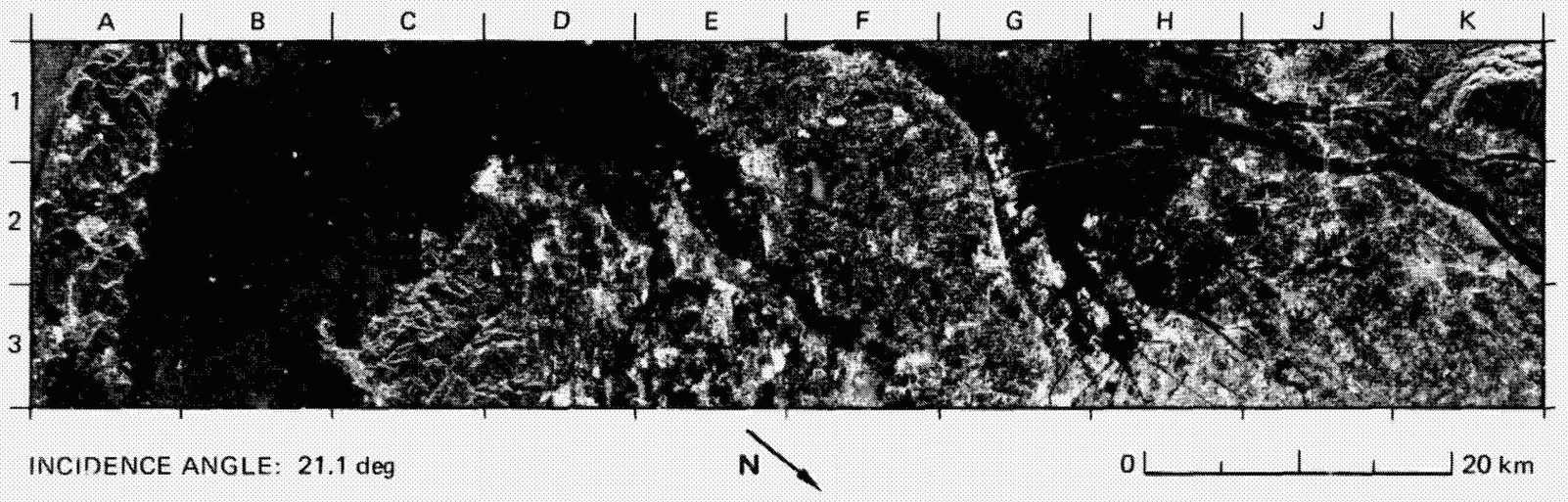


This image covers portions of a major industrial district in the vicinity of Nagoya, Central Honshu, Japan. The port of Nagoya, to the south of the city, is located from G3 to H3. Land use is intensive. Many parts of the coastline are reclaimed land used for factories, petroleum storage, and other industrial purposes. The mole that protects the port of Nagoya appears as a thin bright line that extends obliquely from G2 to H1; it was constructed in 1961 in response to the destructive effects of the 1959 Typhoon Isewan. The mole's three segments have a combined length of 7.6 km; they are 6.5 m high and taper in width from 10 m at the base to 0.4 m at the top.

On the corresponding Landsat TM image, which was obtained in the visible red wavelength (0.63 to 0.69 $\mu$m) 9 days before the radar image, the industrial areas are strongly reflective and appear very bright. The mole, however, is scarcely perceptible on this image.

Reclamation currently in progress along the coast at Kira (C1 to D1) results in geometric patterns of medium to dark-gray tones on the radar image, but it is mostly imperceptible on the TM image. The aerial photograph gives a detailed view of this area.

Intensive rice cultivation is practiced in the deltaic region between the Kiso and Ibi Rivers (J1 to K2). The bridges across these rivers and levees that protect villages against flooding are revealed as bright lines on the radar image.

The trend of Mikawa Bay along the north coast of the Atsumi Peninsula from B1 to B3 marks the trace of a tectonic lineament known as the Median Line in this part of Japan.

(The caption was prepared from information provided by Dr. N. Fugono, Radio Research Laboratories, Ministry of Posts and Telecommunications, Tokyo, Japan. The Landsat image is by courtesy of the Earth Observation Center, National Space Development Agency of Japan; the aerial photograph was provided by the Shyowa Aviation Co., Japan.)

**Landsat TM Band 3**

**Aerial Photograph**

## 32. Northern Shikoku and Seto Inland Sea, Japan

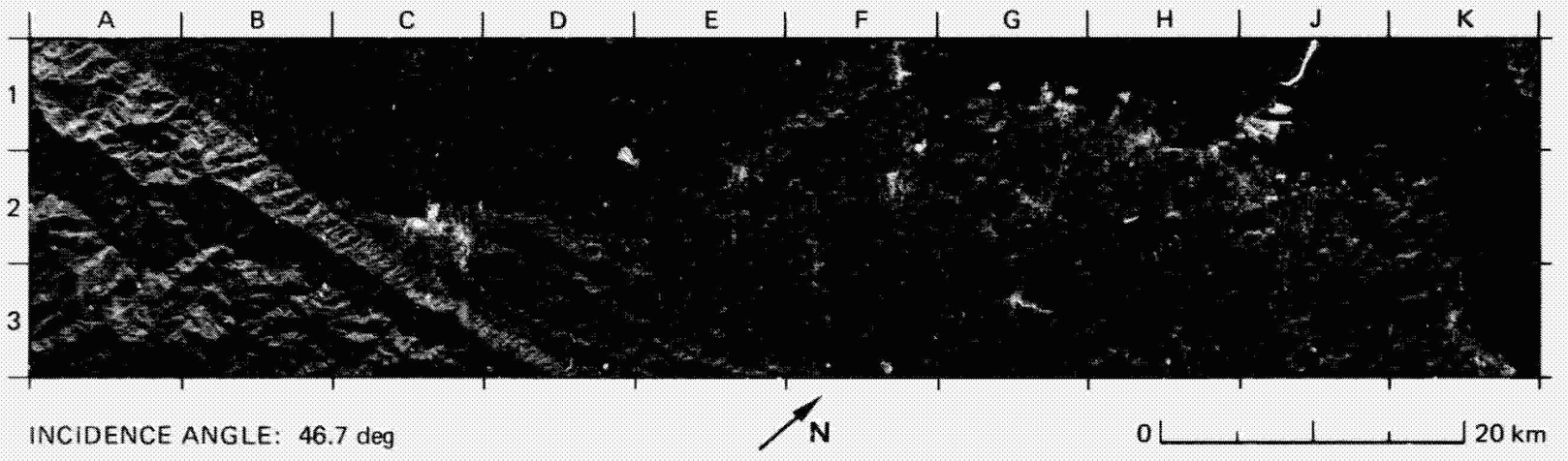


Japan is transected by two major tectonic lineaments. One is the Median Line that divides the southwest part of Japan into an Inner Zone to the north and an Outer Zone to the south. The Median Line is truncated eastward by the Itoigawa-Shizuoka Line that crosses the middle part of Honshu Island in a northerly direction. A portion of the Median Line extends across this image from A1 to D3. Faulting along the Median Line is thought to have started during the Cretaceous Period and has remained active to the present. On the corresponding Landsat TM image, taken in the middle infrared portion of the spectrum (1.55 to 1.75 $\mu$m), the linear structure is clearly contrasted by the differing reflectivity from vegetated slopes that appear dark and coastal urban areas including the town of Iyomishima (C2) that appear light.

Erosional remnants of a former lava plateau are situated in the area from H2 to K2 and H3 to K3. The sloping surfaces are clearly distinguished on the radar image, but the vegetation cover is more clearly outlined on the infrared image. The accompanying aerial photograph (a) shows in greater detail the nature of the surface and the vegetation cover between J2 and K2.

That part of the Sanuki Plain that extends from the coast at H1 to the hills at G3 shows an abundance of irrigation ponds that appear as small dark patches on the radar image. These small reservoirs supplement the relatively low annual rainfall (about 1200 mm) for irrigation in this region of intensive rice cultivation. On the infrared image, the ponds are in strong contrast to the adjacent cultivated fields.

Landsat TM Band 5

Certain cultural features in the coastal region from G1 to J1 appear very bright on the radar image. A most notable feature is the chain of three piers in the upper portion of J1. The piers will form part of the Honshu-Shikoku bridge, which is currently under construction and scheduled for completion in 1988. There is no apparent difference in brightness between the two outside piers that are constructed of steel and the center pier that is made of concrete. The very bright area to the southeast of the bridge is a petroleum storage complex, with many large tanks; it is situated on reclaimed land. The bridge and adjacent coastal region of Shikoku in the vicinity of Sakaide are shown in the aerial photograph (b).

Between the bridge and the river at the bottom margin of H1 and at the left margin of G1 are two coastal areas that appear very dark on the radar image. The corresponding areas are very bright on the TM image. The outlines and the contrasts in reflectivity suggest recently reclaimed land surfaces.

(The caption was prepared from information provided by Dr. N. Fugono, Radio Research Laboratories, Ministry of Posts and Telecommunications, Tokyo, Japan. The Landsat image is by courtesy of the Earth Observation Center, National Space Development Agency of Japan; the aerial photograph was provided by the Shyowa Aviation Co., Japan.)

# C. Oceanography

The SIR-B mission, with its range of incidence angles and orbital configurations that enabled daily viewing of selected Earth locations, provided a good opportunity to test SAR ocean theories and models with coordinated experiments based primarily on previous studies of Seasat SAR imagery.

The imagery in this section was obtained at incidence angles from about 20 deg to 26 deg. It provides an overview of ocean experiments that took place during the flight. The surface-wave experiments focused on comparing accurate in-situ measurements with directional wave spectra derived from the imagery; this allowed examination of various SAR ocean wave theories and models.

## 33. Surface Waves Off Chile, South America

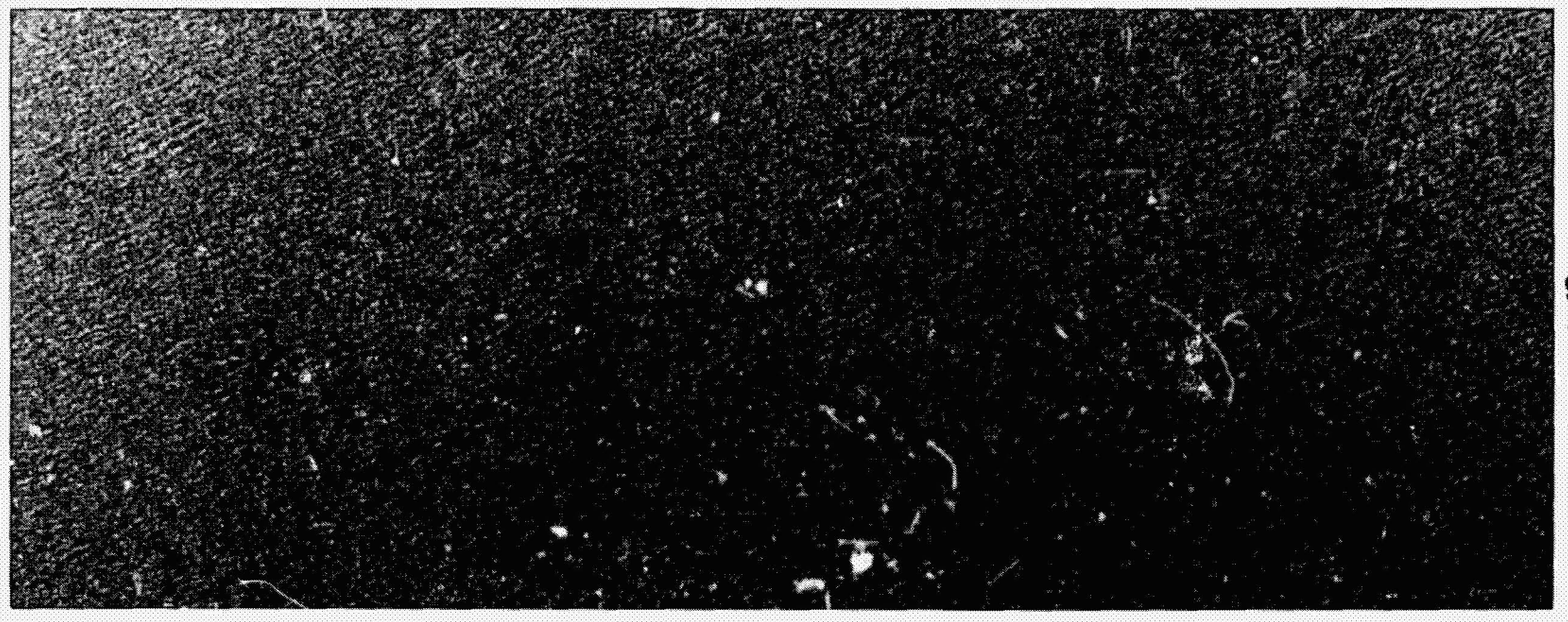

INCIDENCE ANGLE: 25.1 deg

N

0 10 km



Accurate measurement of directional wave-energy spectra over the world's oceans would provide valuable scientific knowledge of global wave climatology and practical reference data to validate, refine, and periodically update existing ocean-wave forecast models. The two-dimensional "snapshots" of ocean surface waves obtained by the Seasat SAR provided such a measure of directional wave spectra. However, a nonlinear effect was introduced into the Seasat imagery that resulted in the inaccurate measurement of waves traveling in the azimuth direction (Alpers, 1983). The shuttle's lower altitude could greatly reduce this nonlinear effect and therefore produce better estimates of wave energy and height from S imagery.

To confirm improvement in stimates of directional wave spectra from SIR-B, a series of aircraft flights off the coast of Chile obtained wave measurements coincident with the SIR-B coverage of this climatologically known region of high significant wave height ($H_s$, the average of the highest one-third of the observed waves). These independent measurements were compared to the Fleet Numerical Oceanography Center's Global Spectral Ocean Wave Model (GSOWM) (Monaldo, 1985).

Figures (a), (b), and (c) are two-dimensional wave spectra generated from the SAR image and these other wave measurements. They present wavelengths of decreasing magnitude in terms of the wavelengths' distances from the center of the spectra; wave propagation direction is determined by the angle of the wave frequency peak from north. The 180-deg ambiguity in direction is resolved by the location of the weather system that generated the waves, which, in this case, was

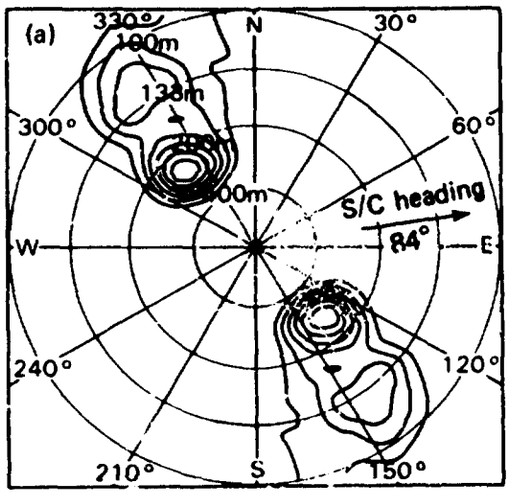


SIR-B intensity variance spectrum; October 11, 0230 GMT, with shuttle (S/C) heading indicated (coordinates: 55.5 deg S, 82.5 deg W).

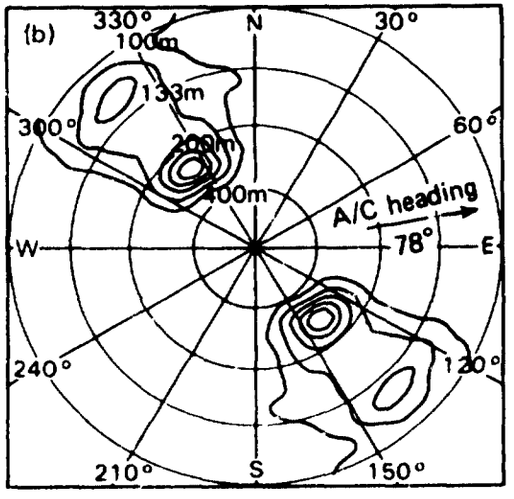


ROWS slope variance spectrum; October 11, 0230 GMT, with aircraft (A/C) heading indicated (coordinates: 55.3 deg S, 81.2 deg W).

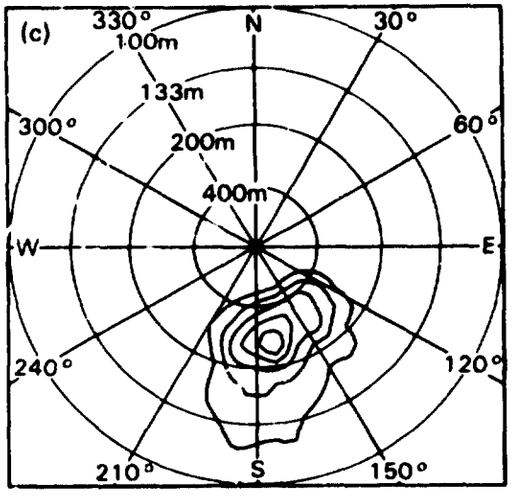


GSOWM height variance forecast; October 11, 00 GMT (coordinates: 55.0 deg, 82.5 deg W).

several hundred kilometers north-northwest of the measurement area, making the peak in the southeast quadrant a correct indicator of propagation direction.

As seen in this image taken on October 11, surface waves were detected off the coast of Chile traveling in the range direction. As figures (a) and (b) indicate, the SAR and the airborne Radar Ocean Wave Spectrometer (ROWS) measurements of the primary wave system were wavelengths of 250 m and 260 m, and propagation directions of 143 deg and 146 deg, respectively; the disparity in $H_s$, however, was significantly greater: 4.0 m for SAR and 4.8 m for ROWS. Also, each instrument showed a secondary wave system of shorter wavelength propagating in nearly the same direction as the primary system. The GSOWM forecast for 00 GMT nearest the SIR-B data location predicted a single wave system with a wavelength of 275 m, a propagation direction of 172 deg, and a $H_s$ of 3.0 m (figure (c)). The GSOWM forecast did not predict a secondary wave system and showed a much broader distribution of directional wave energy for the primary system. As these and other results from the Chile experiment indicate, the GSOWM forecast could have benefitted by incorporation of the SAR (and ROWS) estimates of directional wave spectra.

## 34. Hurricane Josephine, North Atlantic

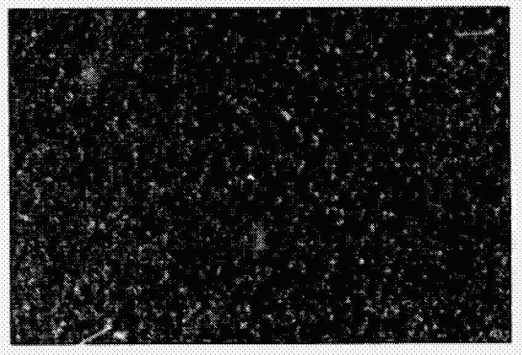

16:31:10

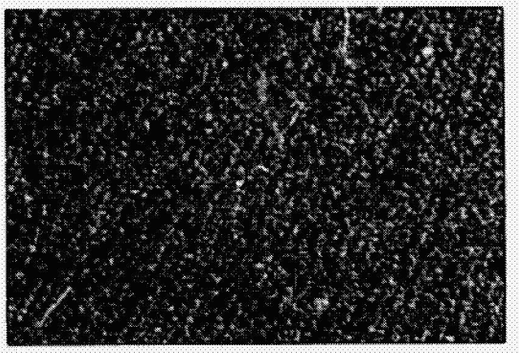

16:31:25

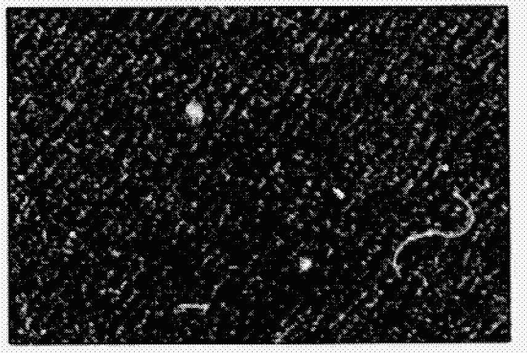

16:31:40

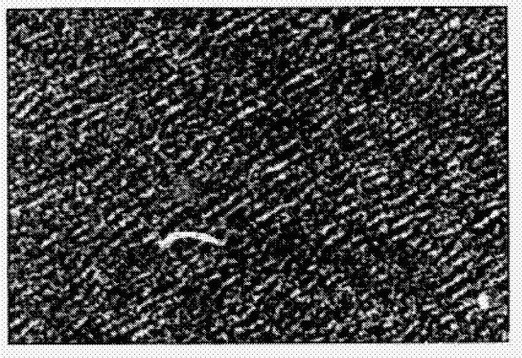

16:31:55

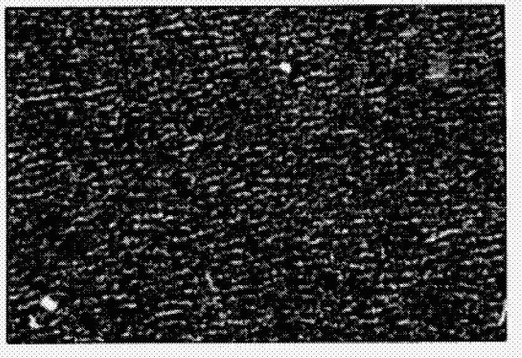

16:32:10

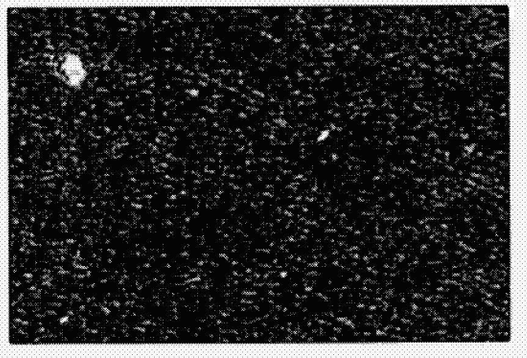

16:32:25

INCIDENCE ANGLE: 24.6 deg

N

0 5 km

ORIGINAL PAGE IS
OF POOR QUALITY

Surface waves generated by hurricane Josephine were imaged off the east coast of North America. As the image enlargements from several locations along the radar track indicate, the waves underwent considerable spatial evolution in propagation direction and wavelength.

Josephine developed from a tropical depression on October 7 to a tropical storm on October 8 and finally a hurricane on October 10 when 65-knot winds occurred (see map). Josephine moved north and east some 2500 kilometers until it dissipated south of Newfoundland on October 18. The imagery was obtained on October 12 at 16:31 GMT during the period of maximum hurricane intensity, when the wind speed was 90 knots.

A partial track of Josephine is given on the map, where maximum wind speeds in knots are indicated at 6-h intervals; the radar track with times of acquisition are also indicated.

From two-dimensional wave spectra obtained from the imagery, the dominant wavelength and direction of the wave systems have been estimated and are shown graphically on the map. The primary wave system propagated north and northeast away from the storm track and underwent a rotation in direction of over 90 deg and a change in wavelength of over 30%: the wavelengths increased from less than 200 m to greater than 300 m. These waves were generated earlier when the hurricane was further south, and they evolved into ocean swell. Secondary wave systems with shorter wavelengths were also detected moving northwest and west in the upper portion of the radar track and east in the lower portion, separated by a zone where no secondary waves were seen. The propagation directions of these secondary waves were aligned roughly in the direction of the cyclonic (counterclockwise) wind field rotating around the hurricane eye, indicating that the secondary waves were locally generated.

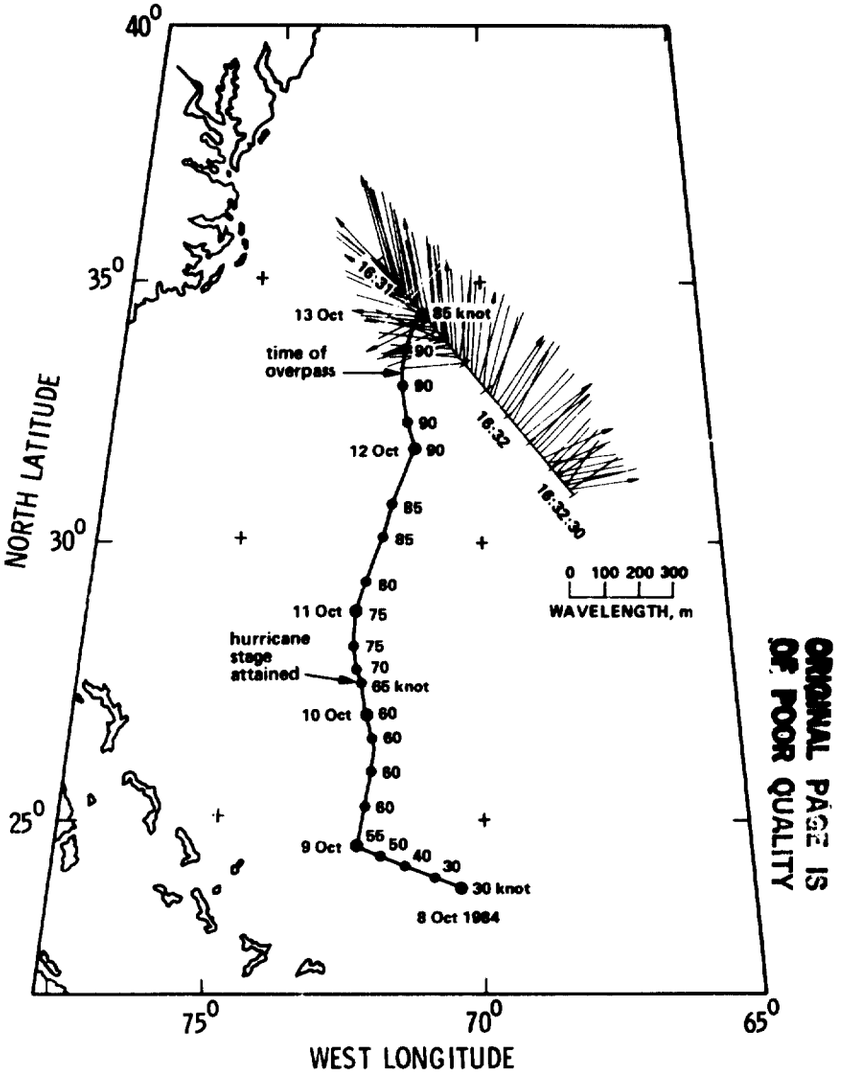

## 35. Surface Waves at Different Aspect Angles, North Atlantic

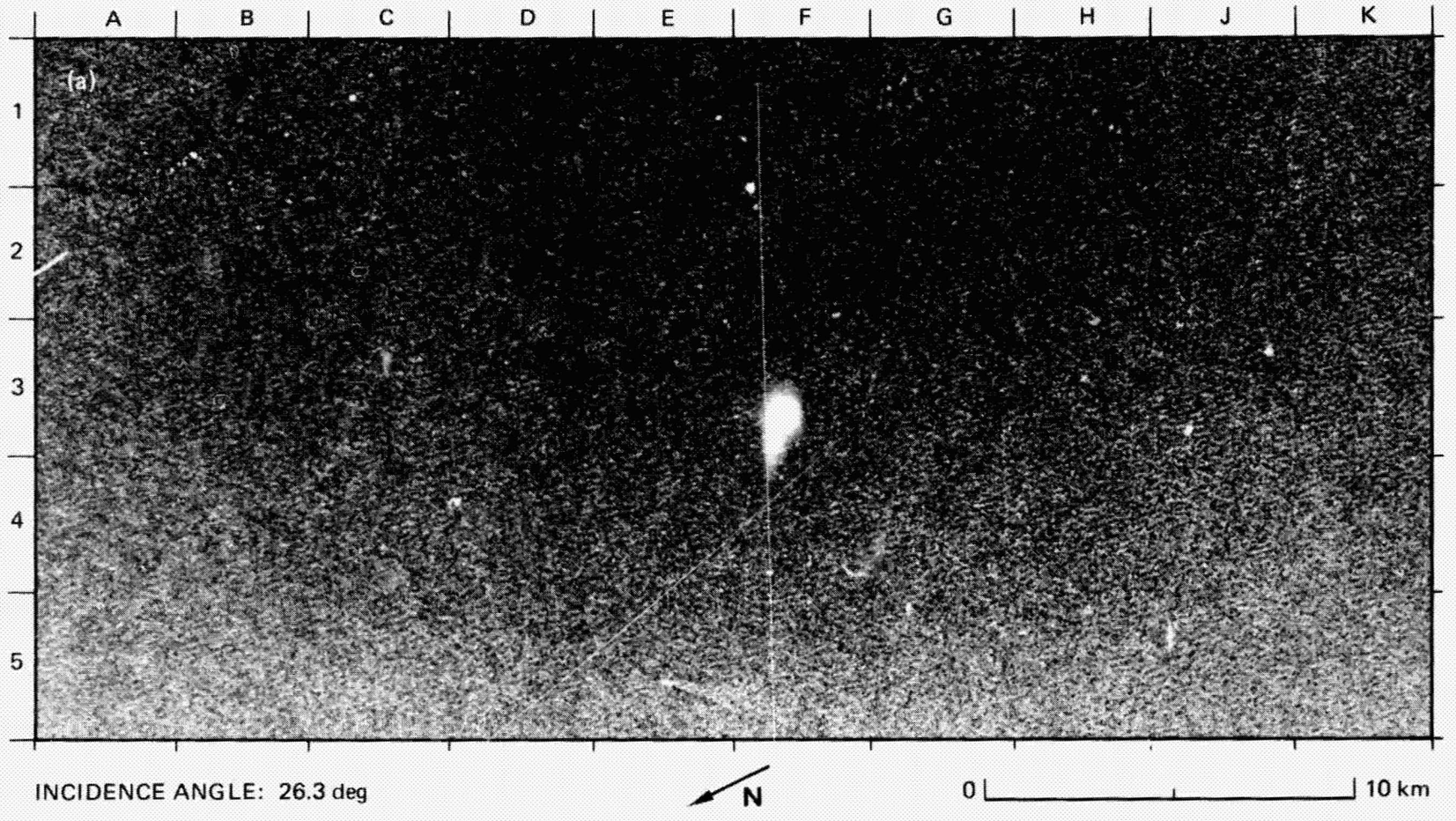


While the principal mechanisms for the SAR imaging of surface waves are fairly well known, the importance of nonlinearities in the imaging mechanisms are not well known (for example, Vesecky and Stewart, 1982; Hasselmann et al., 1985). Determining the mechanisms and their properties are particularly important in measuring ocean wave spectra from SAR imagery based on a transfer function. To test various imaging theories and the influence of environmental parameters on these theories, an experiment was conducted in the North Atlantic Ocean southwest of England to obtain highly accurate wave information from buoys. The buoy data were obtained at the intersection of two SIR-B orbits. The imagery obtained at this intersection permitted viewing one area of the ocean surface at two closely spaced intervals and at significantly different aspect angles.

These two images of the same area in the North Atlantic were taken 6 h apart on October 11, 1984 (Keyte and Macklin, 1986). Image (a) contains waves traveling in the range direction, while image (b) shows the same wave field traveling in the azimuth direction. The heading of the orbital track for image (b) rotated 50 deg clockwise from that for image (a). One of the research ships appears in both images ((a), J5; (b), E3) as a bright narrow target because a radar transponder was on board.

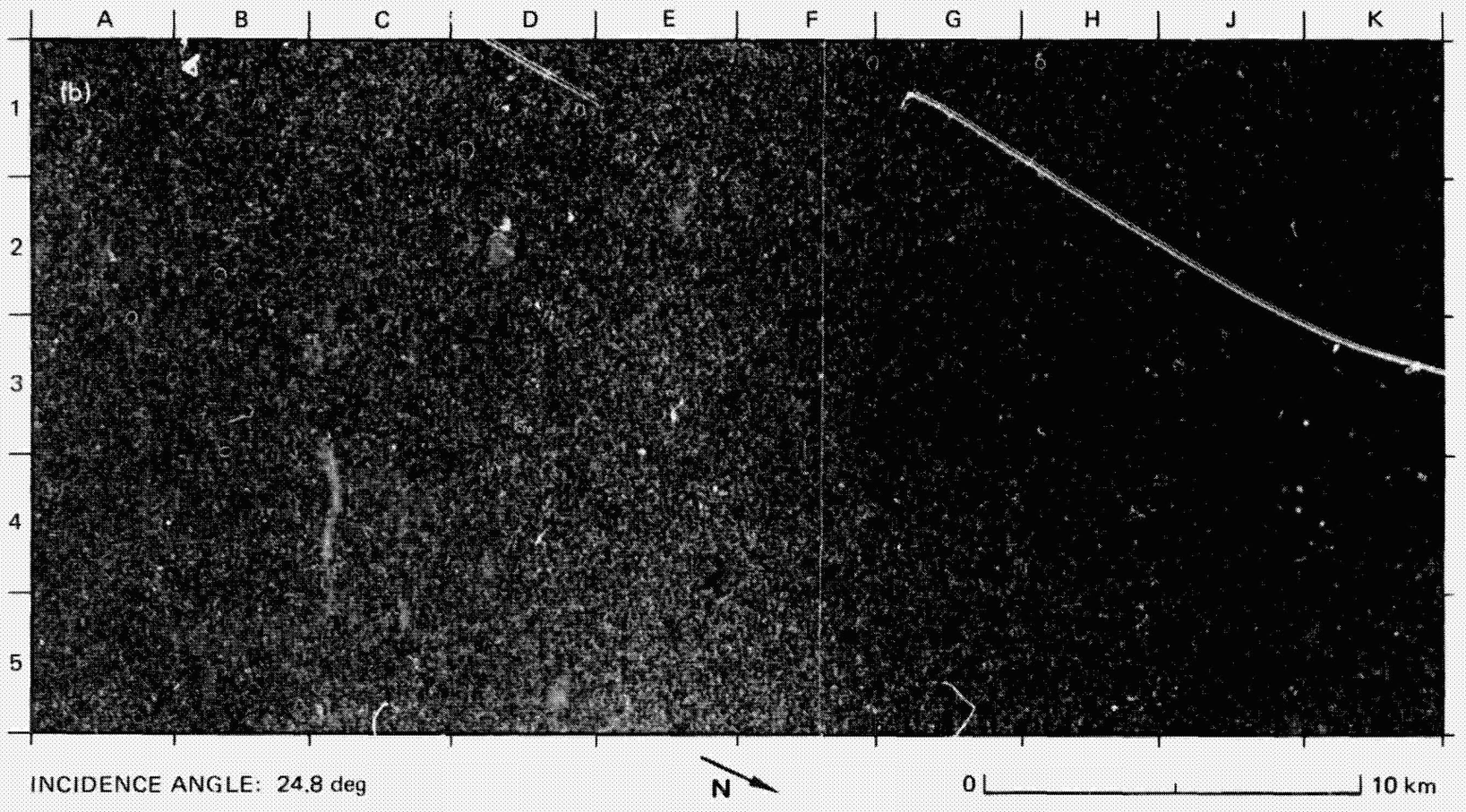




From the SAR spectra, wavelengths of 192 m and 182 m with propagation directions of 319 deg and 290 deg from north were measured for images (a) and (b), respectively. Consistent with linear imaging theories, favorable comparisons in wavelength and direction were obtained by the various deployed buoys. However, although not conclusive, a reduction in the intensities that were based on model predictions of the SAR spectra for the azimuth waves in image (b) may indicate inadequacies in the estimates of certain nonlinearities in the imaging mechanisms.

Also seen in image (a) are a moving cargo ship and its bow or Kelvin wake (E5), two small slicks side by side (A1/A2) produced by a thin surface film, and two research ships faintly visible as bright point targets (B1 and B2). The oil film was discharged by one of the nearby ships to study the dampening of short gravity waves by the film and its effect on the SAR imaging of the ocean surface. The film also indicates the presence of horizontal shear since the original slick subsequently divided into two separate slicks.

## 36. Internal Waves, New York Bight, U.S.A.

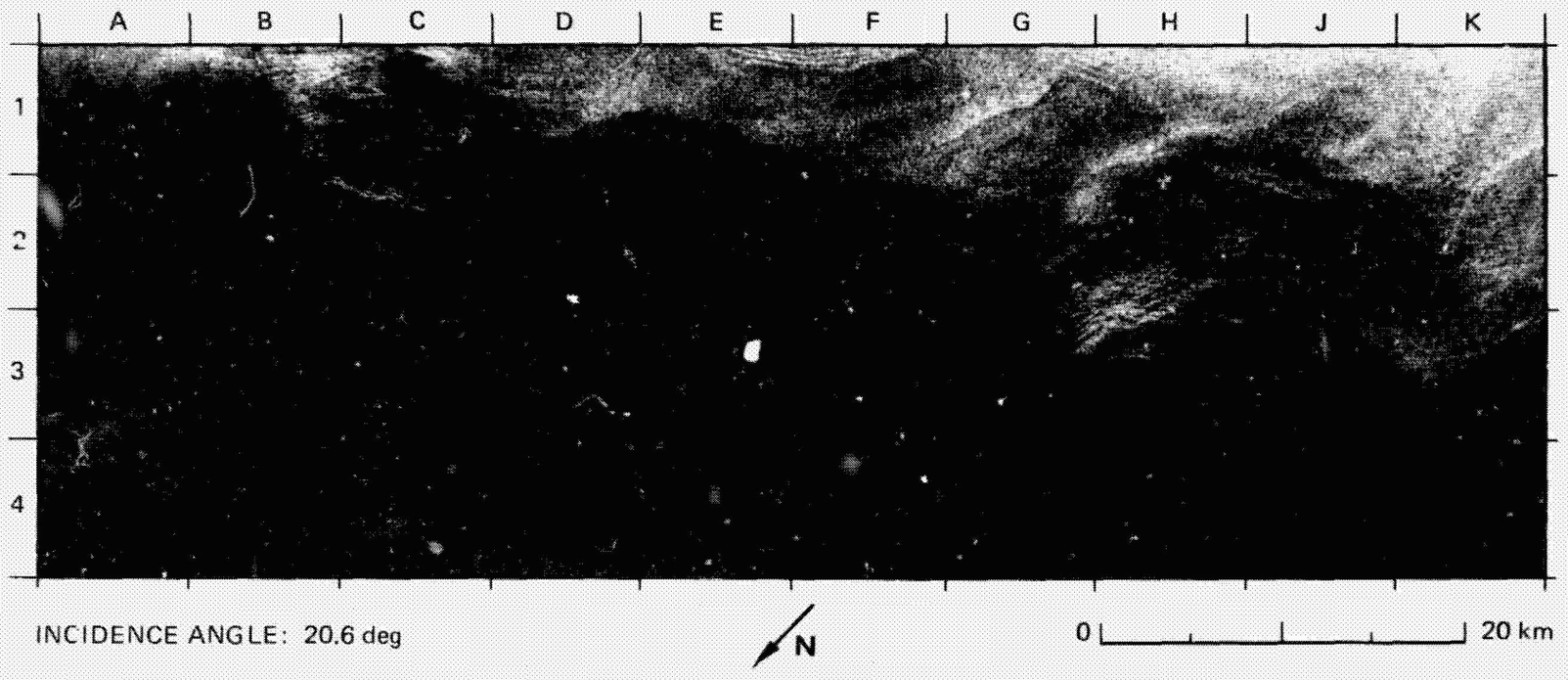




The New York Bight is located northeast of Hudson Canyon on the continental shelf at depths of 50 to 100 m. Internal waves have been extensively observed along this region, particularly in summer when they are trapped in the strong and shallow thermocline, and are believed to be locally generated by tidal interaction with sharp variations in bathymetry. In this image, internal waves are seen as alternating bands of rough and smooth sea surface; these bands result from the modulation of short surface waves by the internal waves themselves.

Within each packet (which is a discrete group of internal waves), the internal waves decrease monotonically in wavelength from a leading wave crest of 400 to 500 m to a rear wave crest of 150 to 200 m, and they are generally aligned parallel to the bathymetric contours. These are characteristic observations of internal waves in coastal waters.

Note the overall low detectability of the internal waves in the dark low-wind area (measured wind speed about 1 m/s), which forms a curvilinear boundary with the bright higher-wind area (measured wind speed about 3 m/s), perhaps indicating an interaction of water masses with slightly different temperatures. In the lower left of the image, the dark streaks are small eddies and/or surface films.

In an experiment headed by R. Gasparovic and J. Apel (SARSEX Interim Report, 1985), ship measurements of several oceanographic parameters important to the understanding of the SAR imaging of internal waves were obtained in this region simultaneously with the shuttle overpass. Specifically measured were parameters associated with the wave packet located at F1 (the ship itself is not detectable). Several temperature profiles (figure (a)) taken near the time of the overpass locate the thermocline at 40 to 45 m – a strong deepening from earlier in the summer – and indicate a cooling in the uppermost layer. The vertical excursions of three isotherms caused by an internal wave field propagating past the ship are shown in figure (b). The internal waves had a peak-to-trough amplitude of about 9 m and a period of about 6 min.

These and other in-situ measurements including surface strain rates, currents, and surface roughness will be used to help understand the hydrodynamic interaction of the short surface waves, the surface currents induced by internal waves, and the resultant modulated radar scattering. This knowledge might enable predictions of the energetics of internal waves from SAR intensity signatures.

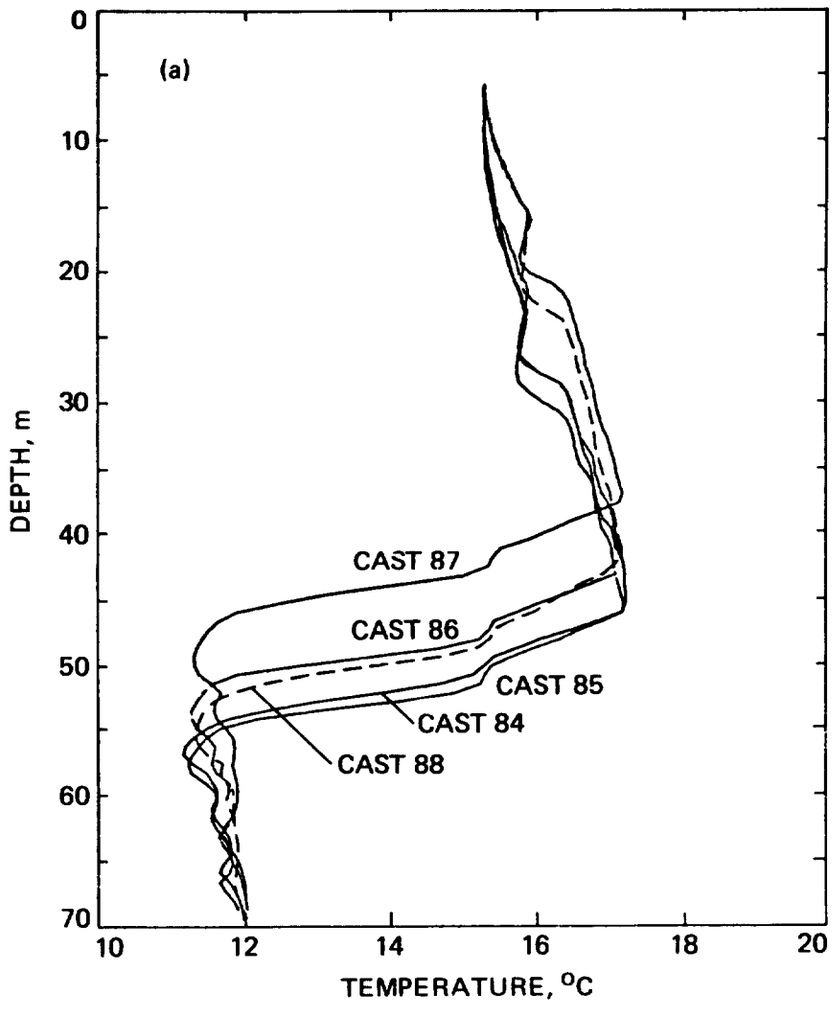
(a)
DEPTH, m
0
10
20
30
40
50
60
70
CAST 87
CAST 86
CAST 85
CAST 84
CAST 88
10
12
14
16
18
20
TEMPERATURE, °C

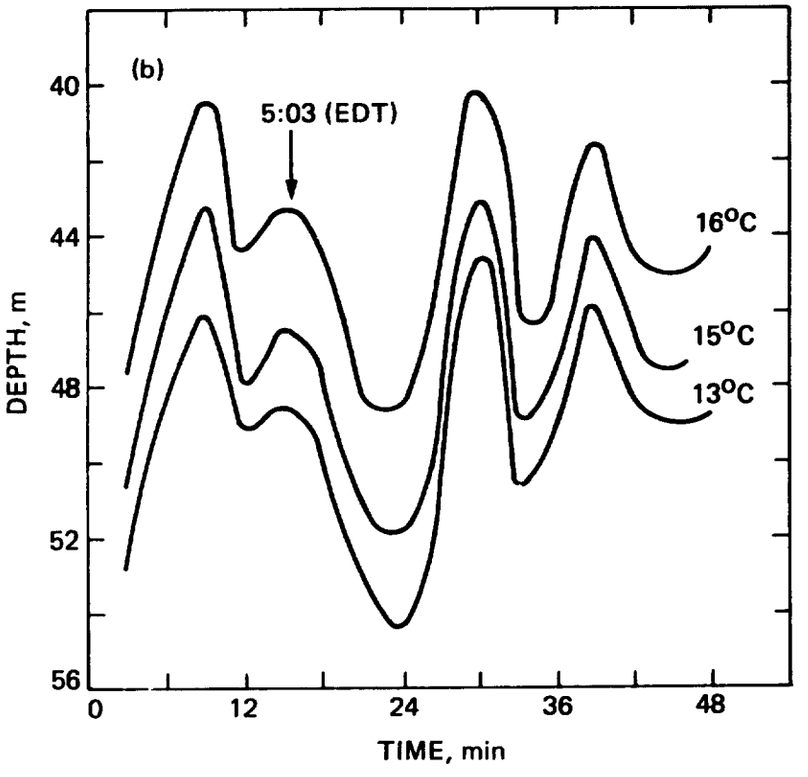
(b)
5:03 (EDT)
16°C
15°C
13°C
DEPTH, m
40
44
48
52
56
0
12
24
36
48
TIME, min

## 37. Small-Scale Eddies Off Long Island, New York, U.S.A.

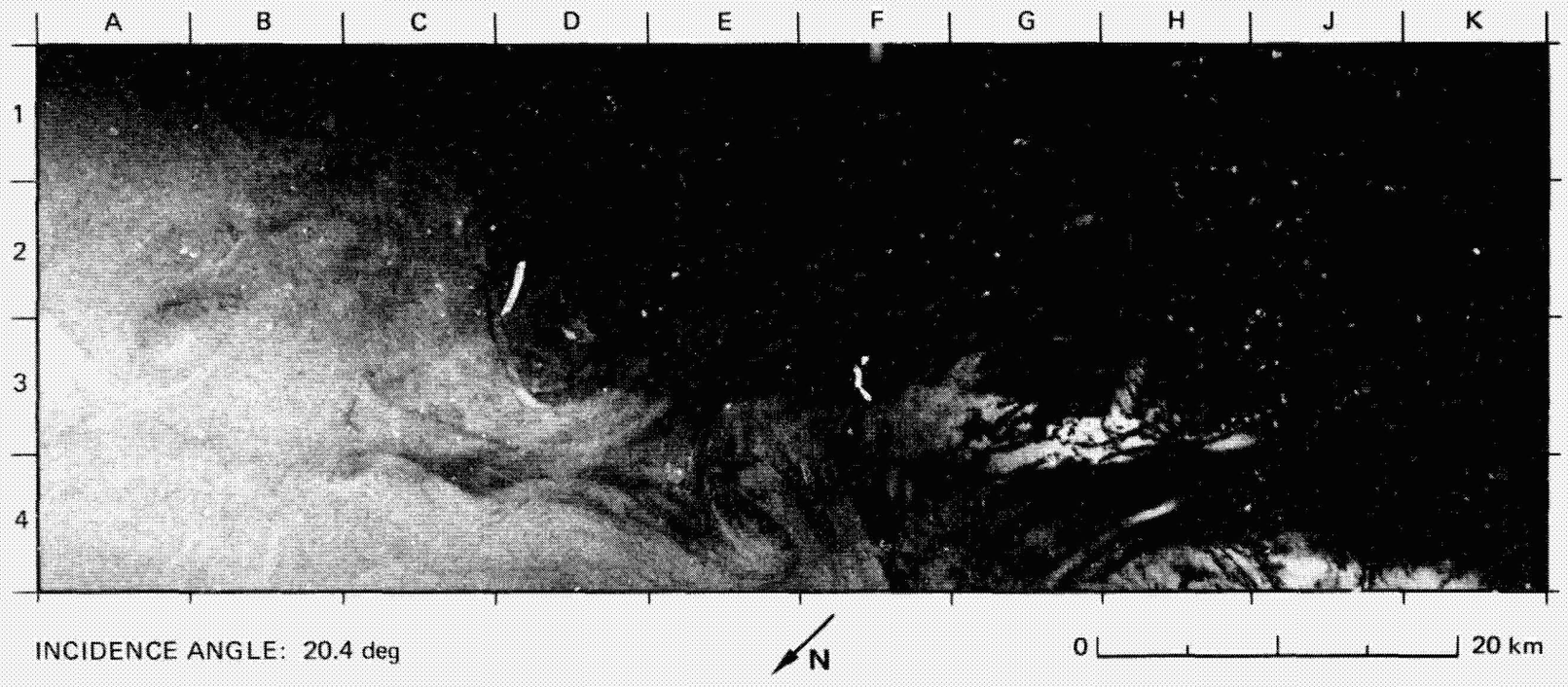




Small-scale eddies are clearly seen in this image (taken October 11, 1984) of the continental shelf east of Long Island. The two fully resolved eddies are cyclonic with diameters of 10 to 15 km and are distinguishable by very thin and dark spiraling streaks (D3 to E3; E4). Portions of other eddies are seen extending into the dark low-wind area. The mean surface currents along this part of the Middle-Atlantic Bight are not strong, flowing southward with velocities of about 10 cm/s (Beardsley and Boicourt, 1981).

During the shuttle mission, several extensive series of hand-held photographs were taken of large fields of small-scale eddies. These fields occurred repeatedly in the Mediterranean and along the East Coast of North America. One such example is given here—a photograph of the continental shelf off Delaware, taken October 9 at noon local time. The eddies show on the photograph because of a sun glitter effect, which occurs when the viewing angle of the camera is equal to the incidence angle of the sun's rays on the ocean surface. Eddies at these scales have been seen on radar imagery from Seasat and SIR-A, particularly in the Caribbean, and most commonly are adjacent to low-wind areas and away from significant surface currents. Some eddies seem to have been formed by strong coastal current shears (Fu and Holt, 1982). The extent of the repeated observations from the shuttle flight suggest that such eddy fields are commonplace in many of the world's seas.

Based on their size and numbers, the eddies in these images seem to fall into a category of phenomena termed submesoscale coherent vortices (McWilliams, 1985). These eddies are long-lived, often travel far from their origins (which are traceable by the chemical properties of the eddies' core waters), have horizontally rotating flow fields, and are most likely generated in the surface mixed layers.

## 38. Shoals Off Martha's Vineyard, Massachusetts, U.S.A.

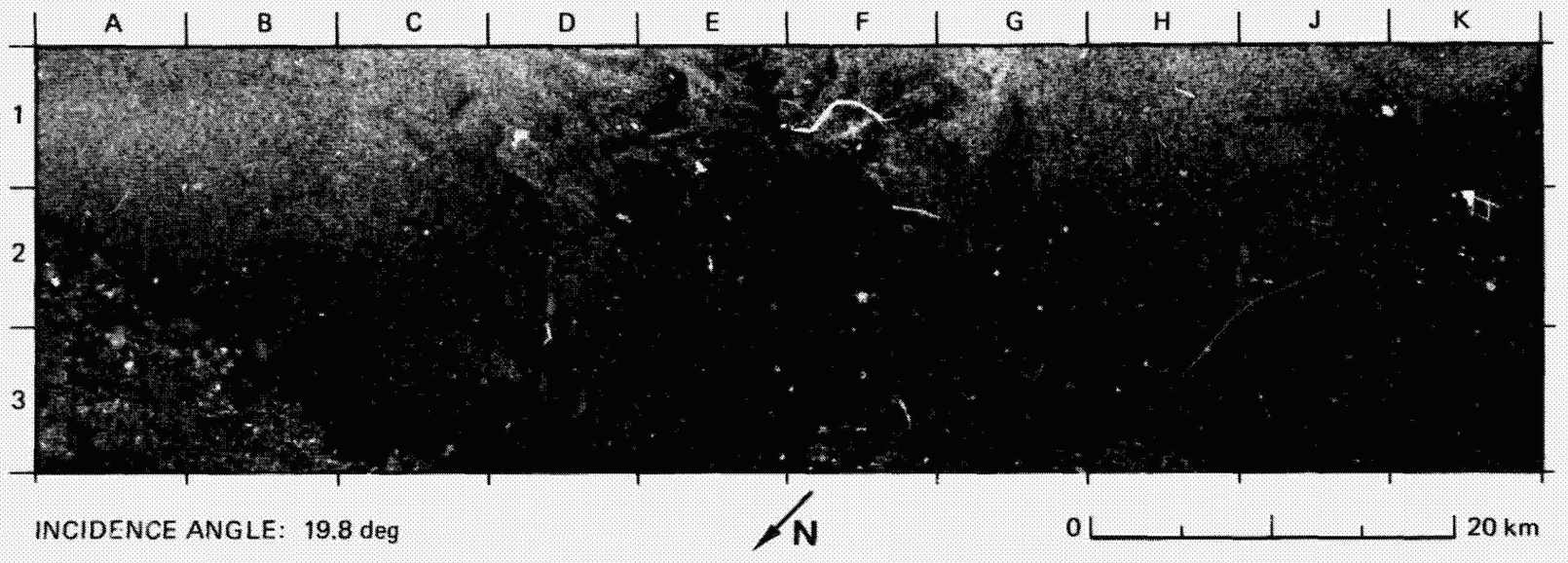


Surface expressions of the shoals off Martha's Vineyard are clearly seen in this image. The shoals are shallow sand regions that rise to within a few meters of the surface from a 10- to 25-m floor; they are part of a large shoal region that extends to nearby Nantucket Island. A comparison of this image with the corresponding bathymetry map indicates a close association of the expressions with the 5- and 10-fathom contour lines. The patterns are characterized by narrow curvilinear bands of low return adjacent to narrow bands of enhanced brightness (for example, D1 and E1). Some of the darkest expressions, such as the narrow curvy band extending off the southeast corner of Chappaquiddick Island (F1), may be shoal areas that are exposed or nearly exposed. Note the lack of surface expressions south of Martha's Vineyard where no shoals are present and off Cape Cod where shallow water *does* occur.

This area has a low tidal range of 1 to 1.3 m with fairly strong and variable tidal currents (from Tidal Current Tables, 1984). At the time of the overpass, the water at Chappaquiddick was some 40 min away from

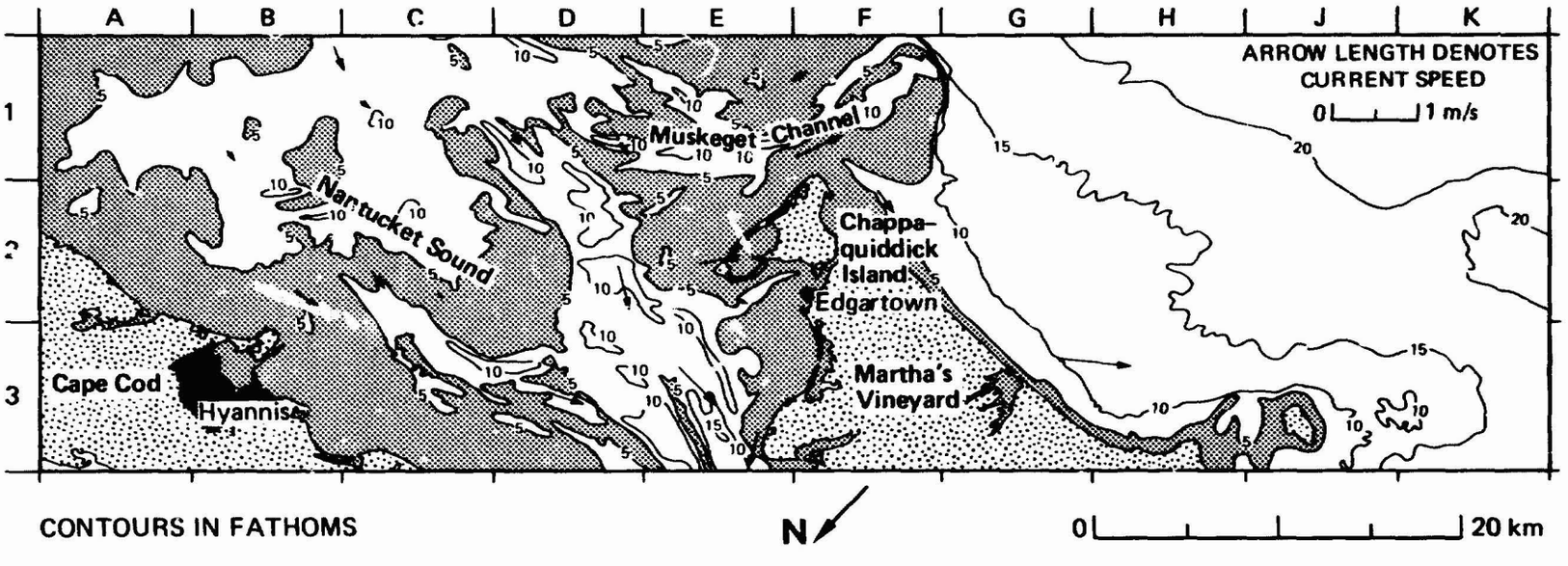


ORIGINAL PAGE IS OF POOR QUALITY

a low tide of 0.1 m; this is nearly the mean tidal level of the area. The tidal current directions and speeds shown on the bathymetry map indicate a generally west-to-southwest tidal flow across the shoal regions. The current speeds near Martha's Vineyard, where the surface expressions are strongest, are generally greater than 0.5 m/s; the speeds near Cape Cod are lower, and there is no surface expression over the shoal region.

The expression of bottom features on SAR imagery is the result of differentiated backscatter of the radar signals. These variations in backscatter are caused by the modulation of short surface waves as the tidal current flows over uneven topography. Essentially, there is no penetration of the sea by the radar signal at the SIR-B frequency. A recent theory (Alpers and Hennings 1984) predicts an enhanced image brightness downstream and reduced image brightness upstream of a subsurface feature. Qualitatively, this is an accurate description of the surface expressions seen in this image, given the direction of tidal current flow.

## 39. Pack Ice, Weddell Sea, Southern Ocean

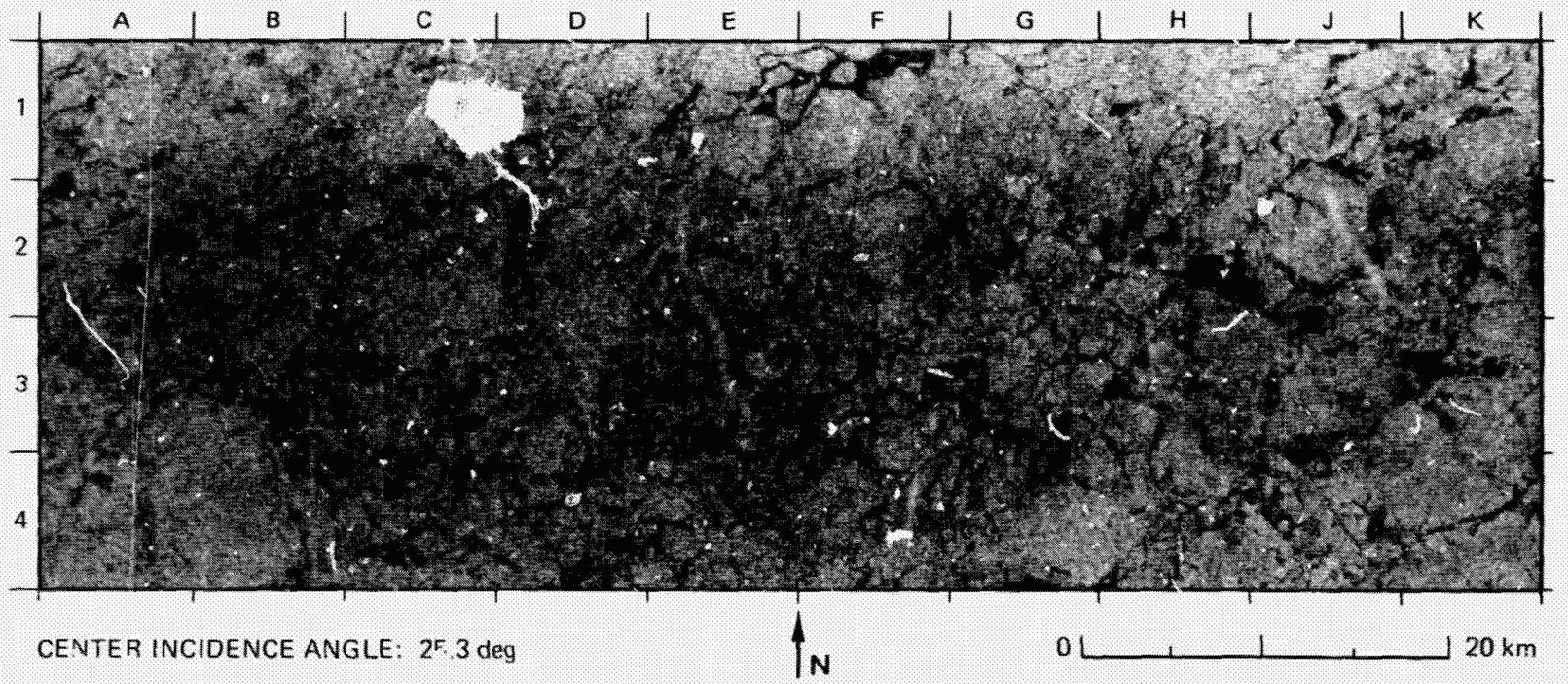


One of the original goals for the sea-ice experiment was to acquire overlapping SIR-B imagery of ice in the Weddell Sea; this imagery could then be used to extract information on ice motion. While such overlapping data was not acquired, the fortuitous coupling of launch date and maximum ice extent allowed three SIR-B data takes to be acquired over sea ice in the Weddell Sea, the first such fine-resolution radar data in the Southern Ocean. These sets are valuable for characterizing the nature of sea ice in the Weddell Sea (Carsey et al., 1986) and can be used in such further studies as the comparison of ice concentrations between SAR and microwave radiometers.

Sea ice in the Southern Hemisphere is more extensive than that in the Northern Hemisphere, but it is seasonal in nature. Whereas sea ice in the Arctic Ocean and surrounding seas decreases about 50% in extent during summer, over 85% of the sea ice in the Antarctic region melts. From this it follows that most of the sea ice in the Southern Ocean is first-year ice (up to 2 m thick) and half of the sea ice in the Arctic region is multiyear ice (between 3 to 5 m thick). In the Southern Ocean, October is typically the month of greatest ice coverage, usually extending north of 60 deg south latitude in the Weddell Sea and occasionally in the Ross Sea (Zwally et al., 1983).

As seen in this image, the sea ice has a bright appearance and the open water leads are dark, with occasional gray areas both on the ice and in the leads (F3, G3, and J3). The gray areas probably indicate thin ice. The ice return is homogeneous and few small-scale features on the ice surface are seen, indicating that either the surface is uniformly rough or volume scattering is contributing to the return, as seen in the return from Arctic winter multiyear ice (Onstott et al., 1979). The floes have both rounded and sharp edges and are considerably fragmented, ranging in size from 0.5 to 10 km, indicating a significant amount of deformation and advection of the ice cover

The accompanying figure is an infrared image of the Weddell Sea from the Advanced Very High Resolution Radiometer (AVHRR) on the

NOAA-6 satellite taken October 9, 1984. Unfortunately, this AVHRR image does not overlap the SIR-B coverage; it covers an area 800 by 1200 km that extends from near the edge of the continental ice sheet on the left (south) through the central ice pack to the marginal ice zone (see image 40). This image shows particularly well the size of the ice floes and the variation in lead formations across the ice pack.

## 40. Marginal Ice Zone, Weddell-Scotia Seas, Southern Ocean

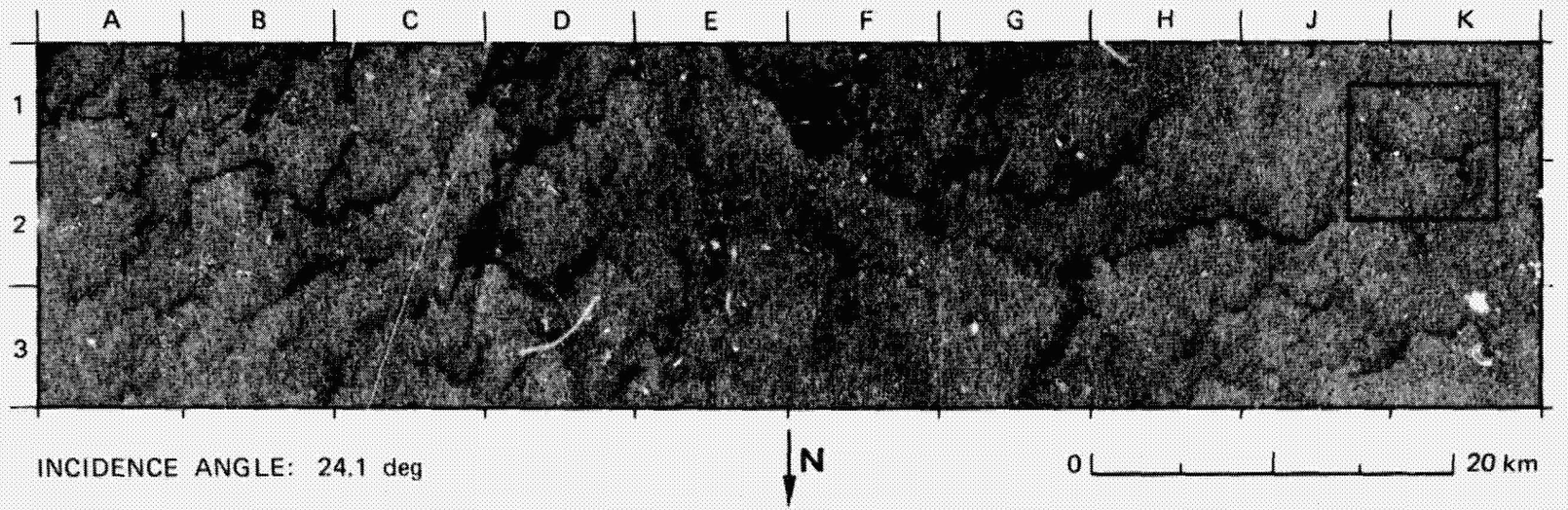


Acquired at the outermost edge of the marginal ice zone in the Weddell-Scotia Seas, this image reveals sea ice as dark wavy bands within the bright open water. Also, numerous icebergs are resolvable as small dark features (for example, J1, F2, and B1). The radar swath also passed over Zavodovski Island (E1/F1), the northernmost island in the South Sandwich chain. Several islands in the chain were first observed by Captain James Cook in 1775 and others, like Zavodovski, by the Russian explorers Bellingshausen and Lazarev in 1820.

An analysis of this image (Carsey et al., 1986) indicates that the wavy sea-ice features are composed of small floes—1 to 20 m in diameter—that have aggregated into bands. One such band has been pushed against the northern edge of Zavodovski Island. The dark appearance of the bands may be the result of upper-surface wetting of the floes. Surface waves, which break up ice at the margins into smaller floes, are detected propagating through the ice bands (see enlargement). Up to 13 icebergs with diameters from 0.1 to 1.3 km are scattered throughout the image. Their appearance is characterized by a dark upper surface and a bright line at the illuminated side of the berg. In general, the ocean around the bergs has a dark return to the south, where the sea surface is calmer (see enlargement), and compared to the surrounding ocean, an enhanced bright return to the north, where the incident wind waves interact with the waves reflecting off the iceberg.

The ice bands are very similar to bands seen at the Bering Sea ice margin (Martin et al., 1983; Wadhams, 1983; Muench et al., 1983),

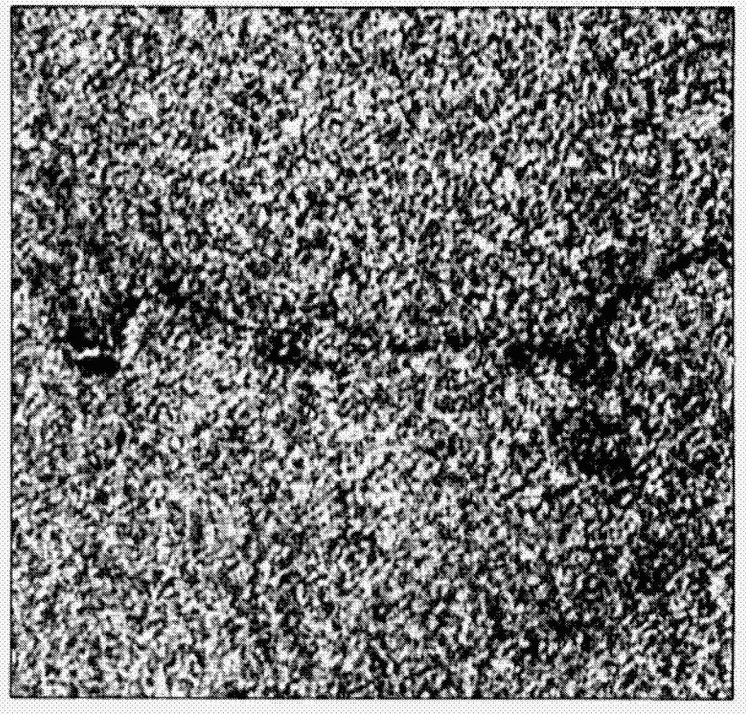

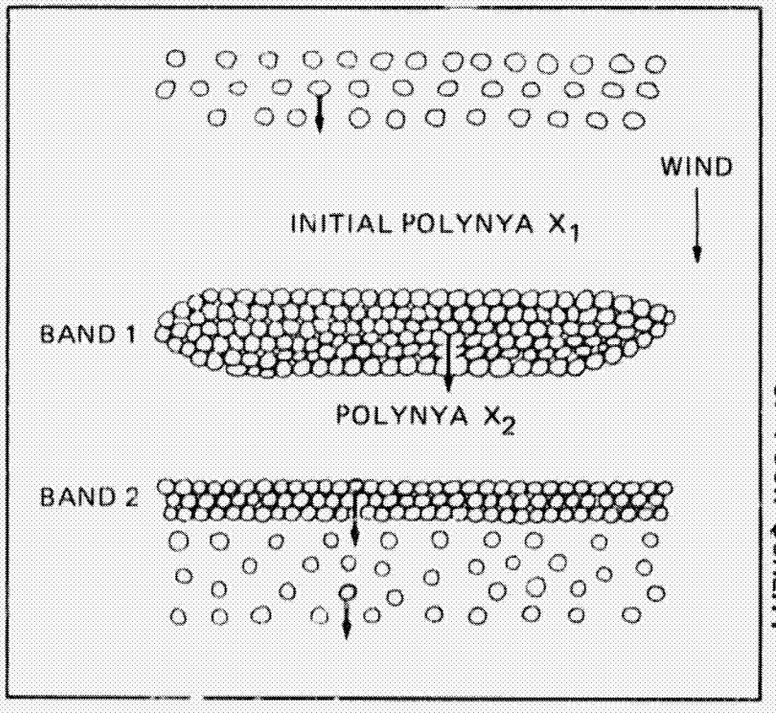




where they have been shown to form during off-ice winds, and have typical lengths of 10 km and widths of 0.1 to 1.0 km; they are oriented at approximate right angles to the wind. A diagram after Wadhams (1983) illustrates the formation, consolidation, and movement of ice bands, which are separated by open water or polynyas, during off-ice winds.

As suggested by the band forced against the island and the wind patterns around the icebergs, there was a wind from the north at the time the imagery was acquired; this is confirmed by regional weather charts. The ice bands were in fact formed three days earlier and were being driven back towards the ice pack.

# References


Alpers, W., 1985, "Monte Carlo Simulations for Studying the Relationship Between Ocean Wave and Synthetic-Aperture Radar Image Spectra," *J. Geophys. Res.*, Vol. 88, No. C3, pp. 1745–1759.

Alpers, W., and I. Hennings, 1984, "A Theory of the Imaging Mechanism of Underwater Bottom Topography by Real- and Synthetic-Aperture Radar," *J. Geophys. Res.*, Vol. 89, No. C6, pp. 10,529–10,546.

Baker, M. C. W., and P. W. Francis, 1978, "Upper Cenozoic Volcanism in the Central Andes — Ages and Volumes," *Earth Planet. Sci. Lett.*, Vol. 41, pp. 175–187.

Beal, R. C., P. S. DeLeonibus, and I. Katz, eds., 1981, *Spaceborne Synthetic-Aperture Radar for Oceanography*, Johns Hopkins University Press, Baltimore, Maryland, 215 pp.

Beardsley, R. C., and W. C. Boicourt, 1981, "On Estuarine and Continental-Shelf Circulation in the Middle Atlantic Bight," in *Evolution of Physical Oceanography*, B. A. Warren and C. Wunsch editors, MIT Press, Massachusetts Institute of Technology, Cambridge, Massachusetts.

Blom, R. G., and C. Elachi, 1981, "Spaceborne and Airborne Imaging Radar Observations of Sand Dunes," *J. Geophys. Res.*, Vol. 86, pp. 3061–3073.

Blom, R. G., and C. Elachi, 1986, "Multifrequency and Multipolarization Radar Scatterometry of Sand Dunes and Comparison with Spaceborne and Airborne Radar Images," *J. Geophys. Res.*, in press.

Blom, R. G., R. J. Crippen, and C. Elachi, 1983, "Detection of Subsurface Features in Seasat Radar Images of Means Valley, Mojave Desert, California," *Geology*, Vol 12, pp. 346–349.

Carsey, F. D., B. Holt, S. Martin, L. McNutt, D. A. Rothrock, V. A. Squire, and W. F. Weeks, 1986, "Weddell-Scotia Sea Marginal Ice Zone Observations From Space," *J. Geophys. Res.*, Vol. 91, No. C3, pp. 3920–3924.

Carver, K. R., C. Elachi, and F. T. Ulaby, 1985, "Microwave Remote Sensing From Space," *IEEE, Proc.*, Vol. 73, No. 6, pp. 970–996.

Cimino, J. B., and C. Elachi, 1982, *Shuttle Imaging Radar-A (SIR-A) Experiment*, Publication 82–77, Jet Propulsion Laboratory, Pasadena, California.

Crandell, D. R., C. D. Miller, H. X. Glicken, R. L. Christiansen, and C. G. Newhall, 1984, "Catastrophic Debris Avalanche From Ancestral Mount Shasta Volcano," *Geology*, Vol. 12, pp. 143–146.

Elachi, C., 1980, "Spaceborne Imaging Radar: Geologic and Oceanographic Applications," *Science*, Vol. 209, No. 4461, pp. 1073–1082.

Elachi, C., L. E. Roth, and G. G. Schaber, 1984, "Spaceborne Radar Subsurface Imaging in Hyperarid Regions," *IEEE, Trans., Geosci. Rem. Sens.*, Vol. GE-22, No. 4, pp. 383–388.

Elachi, C., T. Bicknell, R. L. Jordan, and C. Wu, 1982, "Spaceborne Synthetic-Aperture Imaging Radars: Applications, Techniques, and Technology," *IEEE Proc.*, Vol. 70, pp. 1174–1209.

Elachi, C., T. Farr, J. P. Ford, J. Muskat, D. L. Evans, and M. L. Bryan, 1981, "Earth Observation With the Seasat Spaceborne Imaging Radar," *Revue Photo-Inter.*, No. 4, 1–5, Editions Technip, Paris, France, 31 pp.

Elachi, C., et al., 1982, "Shuttle Imaging Radar Experiment," *Science*, Vol. 218, No. 4576, pp. 996–1003.

Engheta, N., and C. Elachi, 1982, "Radar Scattering From a Diffuse Vegetation Layer Over a Smooth Surface," *IEEE, Trans., Geosci. Rem. Sens.*, Vol. GE-20, pp. 212–216.

Ford, J. P., 1980, "Seasat Orbital Radar Imagery for Geologic Mapping: Tennessee-Kentucky-Virginia," *Amer. Assoc. Petrol. Geo. Bull.*, Vol. 64, pp. 2064–2094.

Ford, J. P., 1984, "Mapping of Glacial Landforms From Seasat Radar Images," *Quat. Res.*, Vol. 22, pp. 314–327.

Ford, J. P., J. B. Cimino, and C. Elachi, 1983, *Space Shuttle Columbia Views the World With Imaging Radar: The SIR-A Experiment*, Publication 82–95, Jet Propulsion Laboratory, Pasadena, California, 179 pp.

Ford, J. P., R. G. Bloom, M. L. Bryan, M. I. Daily, T. H. Dixon, C. Elachi, and E. C. Xenos, 1980, *Seasat Views North America, the Caribbean, and Western Europe With Imaging Radar*, Publication 80–67, Jet Propulsion Laboratory, Pasadena, California, 141 pp.

Fu, L.-L., and B. Holt, 1982, *Seasat Views Oceans and Sea Ice With Synthetic-Aperture Radar*, Publication 81-120, Jet Propulsion Laboratory, Pasadena, California, 200 pp.

Hasselmann, K., R. K. Raney, W. J. Plant, W. Alpers, R. A. Shuchman, D. R. Lyzenga, C. L. Rufenach, and M. J. Tucker, 1985, "Theory of Synthetic-Aperture Radar Ocean Imaging: A MARSEN View," *J. Geophys. Res.*, Vol. 90, No. C3, pp. 4659–4686.

Huguett, A., J. Galvis, and P. Ruge, 1979, *La Amazonia Colombiana y sus Recursos, Proyecto Radargrametrico del Amazonas*, Bogotá, Colombia, chapter 2, pp. 35–92.

Jordan, T. E., B. L. Isacks, R. W. Allmendinger, J. A. Brewer, V. A. Ramos, and C. J. Ando, 1983, "Andean Tectonics Related to Geometry of Subducted Nazca Plate," *Geo. Soc. Am. Bull.*, Vol. 94, No. 3, pp. 341–361.

Keyte, G. E., and J. T. Macklin, 1986, "SIR-B Observations of Ocean Waves in the NE Atlantic," *IEEE J. Geosci. and Rem. Sen.*, July.

Kirk, H. J. C., 1957, *The Geology and Mineral Resources of the Upper Rajang and Adjacent Areas*, Geological Survey Department, British Territories in Borneo, Memoir 8, 181 p., maps.

Martin, S., P. Kauffman, and C. Parkinson, 1983, "The Movement and Decay of Ice Edge Bands in the Winter Bering Sea," *J. Geophys. Res.*, Vol. 88, No. C5, pp. 2803–2812.

McCauley, J. F., et al., 1982, "Subsurface Valleys and Geoarcheology of the Eastern Sahara Revealed by Shuttle Radar," *Science*, Vol. 218, No. 4576, pp. 1004–1020.

McWilliams, J. C., 1985, "Submesoscale, Coherent Vortices in the Ocean," *Rev. Geophys.*, Vol. 23, No. 2, pp. 165–182.

Monaldo, F. M., 1985, "Measurements of Directional Wave Spectra by the Shuttle Synthetic Aperture Radar," *Johns Hopkins APL Tech. Digest*, October–December, Vol. 6, No. 4, pp. 354–360.

Muench, R. D., P. H. LeBlond, and L. E. Hachmeister, 1983, "On Some Possible Interactions Between Internal Waves and Sea Ice in the Marginal Ice Zone," *J. Geophys. Res.*, Vol. 88, No. C5, pp. 2819–2826.

Onstott, R. G., R. K. Moore, and W. F. Weeks, 1979, "Surface-Base Scatterometer Results of Arctic Sea Ice," *IEEE Trans. Geosci. Electron.*, GE-17, pp 78–85.

Pinheiro, S. da S., et al., 1976, *Projeto Radambrasil, Folha NA. 19, Pico da Neblina*, Departamento Nacional de Produção Mineral, Rio de Janeiro, Brazil, chapter 1, pp. 17–137.

Ranford, L. C., P. J. Cook, and J. M. Fetherston, 1968, *Rodinga Northern Territory*, Sheet SG 53-Z, Australia Scale 1:250,000 Geological Series, Bureau of Mineral Resources, Geology and Geophysics, Canberra, Australia.

Rinner, K., 1948, *Die Geometrie des Funkmessbildes*, Austrian Academy of Science. Also published in *Handbuch der Vermessunde*, edited by Jordon-Eggert-Kneissl, Vol. VI, Metzlersche Verlagsbuchhandlung, Stuttgart, Federal Republic of Germany.

Rosidi, H. M. D., S. Tjokrosapoetro, and B. Pendowo, 1976, *Geologic Map of the Painan and Northeastern Part of the Muarasiberut Quadrangles, Sumatra*, Geological Survey of Indonesia, Bandung, Indonesia, Scale 1:250,000.

Sabins, F. F., 1983, "Geologic Interpretation of Space Shuttle Radar Images of Indonesia," *Amer. Assoc. Petrol. Geo. Bull.*, Vol. 67, pp. 2076–2099.

Sabins, F. F., R. Blom, and C. Elachi, 1980, "Seasat Radar Image of San Andreas Fault, California," *Amer. Assoc. Petrol. Geo. Bull.*, Vol. 64, pp. 619–628.

*SARSEX Interim Report*, 1985, Johns Hopkins University, Applied Physics Laboratory, Report No. STD-R-1200.

Schobbenhaus, C., D. de A. Campos, G. R. Derze, and H. E. Asmus, 1984, *Geologia do Brasil*, Departamento Nacional da Produção Mineral, Brasília, Brazil, 501 pp.

Simandjuntak, T. O.; Sukardi; T. Budhitrisna; and Surono, 1981, *Geologic Map of the Muarabungo Quadrangle, Sumatra*, Geological Research and Development Centre, Bandung, Indonesia, preliminary map, Scale 1:250,000.

*SIR-B Science Plan*, 1982, Publication 82-78, Jet Propulsion Laboratory, Pasadena, California.

*The SIR-B Science Investigation Plan*, 1984, Publication 84-3, Jet Propulsion Laboratory, Pasadena, California.

*Tidal Current Tables*, 1984, *Atlantic Coast of North America*, National Ocean and Atmospheric Administration, National Ocean Survey, Rockville, Md.

Vesecky, J., and R. H. Stewart, 1982, "The Observation of Ocean Surface Phenomena Using Imagery From the Seasat Synthetic-Aperture Radar: An Assessment," *J. Geophys. Res.*, Vol. 87, No. C5, pp. 3397–3430.

Wadge, G., and T. H. Dixon, 1984, "A Geological Interpretation of Seasat-SAR Imagery From Jamaica," *J. Geo.*, Vol. 92, pp. 561–581.

Wadhams, P., 1983, "A Mechanism for the Formation of Ice Edge Bands," *J. Geophys. Res.*, Vol. 88, No. C5, pp. 2813–2818.

Zwally, H. J., J. C. Comiso, C. L. Parkinson, W. J. Campbell, F. D. Carsey, and P. Gloersen, 1983, *Antarctic Sea Ice 1973–1976: Satellite Passive Microwave Observations*, 206 pp., NASA SP-459.

# Appendix A
# Glossary of Acronyms and Technical Terms

| | |
|---|---|
| aa | basaltic lava flow with rough, splintery surfaces |
| acidic | containing over 66% $SiO_2$, as applied to igneous rocks (cf. basic) |
| A/D | analog to digital (data conversion) |
| albedo | ratio of electromagnetic radiation reflected by a body to the amount of radiation incident upon the body |
| alluvial fan | cone-shaped deposit formed where a stream issues from mountains onto lowlands |
| alluvium | stream deposits of comparatively recent time |
| andesitic | composed essentially of andesine and one or more mafic constituents, as applied to volcanic rocks |
| anticline | folded-rock structure whose limbs dip away from the fold axis |
| aspect angle | azimuth viewing angle, expressed as a compass direction |
| azimuth | bearing of a line measured clockwise from geographic north |
| azimuth (radar imaging) | along-track direction of image acquisition |
| backscatter (radar) | portion of transmitted microwave energy that is reflected back to the radar antenna to create a radar image |
| band | an interval in the electromagnetic spectrum (qv) whose boundaries are marked by a lower and an upper limiting wavelength or frequency |
| bandwidth | frequency range used to modulate a transmitted carrier frequency |
| basaltic | composed essentially of calcic plagioclase and pyroxene, as applied to fine- to medium-grain igneous rocks |
| basement | crustal rocks of deep-seated origin, generally igneous and metamorphic |
| basic | comparatively low in silica, as applied to igneous rocks (cf. acidic) |
| basin | low crustal area of tectonic origin where sediments have accumulated |
| bedding | collective term for planes dividing sedimentary rock layers |
| caldera | large circular depression in volcanic terrain that originates from collapse or explosion |
| caliche | surficial debris cemented by porous calcium carbonate |
| clastic | composed predominantly of fragments derived from preexisting rocks, as applied to sedimentary rocks |
| correlation (radar) | processes by which the Doppler phase histories recorded on tape or radar signal film are converted into radar images, using optical or digital techniques |
| craton | stable area of Earth's continental crust; includes shield and platform |
| dacitic | similar to andesitic, but having less calcic plagioclase and more quartz, as applied to volcanic rocks |
| density slice | classification of continuously variable digital image data into discrete intervals represented by different colors or gray levels |
| depression angle (radar) | angle between the horizontal plane and the line that links an imaging radar antenna to a feature on the ground; commonly used to describe the imaging geometry of airborne imaging radars |
| dike | tabular body of intrusive igneous rock that crosscuts the structure of the host rock |

| | |
|---|---|
| dip | angle at which a bed or other planar feature is inclined to the horizontal |
| dipterocarp | any of a family of tall trees of tropical Asia or Indonesia bearing two-winged fruit |
| dome | any structural deformation characterized by approximately circular local uplift (e.g., salt dome, rock dome) |
| DOMSAT | domestic satellite |
| dynamic range | sensitivity of a radar system in dB |
| electromagnetic spectrum | an ordered progression of radiations that includes cosmic, gamma, X, ultraviolet, visible, infrared, microwave, and radiowave energy |
| eolian | related to wind action, as applied to erosion, transport, and deposition of sediments |
| flatiron | pattern on remotely sensed images and photographs from which dip and strike of layered rocks may be inferred |
| floodplain | the portion of a river valley built of sediment deposited by an existing river, the plain is covered with water when the river overflows its banks |
| gneiss | coarse-grained metamorphic rock with alternating bands of granular and schistose material |
| granite | coarse-grained igneous rock composed essentially of quartz and alkalic feldspar |
| gravity wave | ocean-surface wave longer than 2 cm whose restoring force is dominated by gravity |
| graywacke | coarse-grained sandstone consisting of angular grains of quartz and feldspar, with a variety of rock and mineral fragments embedded in a compact clayey matrix |
| halophyte | plant that requires a salty or alkaline soil |
| ice floe | relatively flat piece of sea ice 20 m or more across |
| igneous rock | rock solidified from a former molten state |
| ignimbrite | volcanic rock formed by wide distribution and consolidation of ash flows |
| illumination direction (radar) | direction in which pulses of microwave energy are transmitted from an imaging-radar antenna; normally at right angles to the line of flight of the sensor |
| image | visual reproduction of a scene acquired by SAR, MSS, TM, or photographic sensor |
| incidence angle (radar) | angle between the incident radar beam at the ground and the normal to the ground surface at the point of incidence |
| inselberg | isolated residual hill rising above the general level of the erosion surface |
| internal wave | subsurface ocean wave that occurs at a density gradient within the water column |
| island arc | curved chain of islands rising from deep sea floor, near a continent |
| Kanamori scale | a scale for quantifying the energy in very large magnitude earthquakes; the scale is recalibrated from and more accurate than the Richter scale |
| karst | an irregular hummocky terrain marked by subsurface drainage and numerous sinkholes interspersed with abrupt ridges. The subsurface is characterized by caverns and features formed by the solution and collapse of limestone |
| Landsat | any of a series of five orbital imaging satellites that have measured and recorded reflectance from the Earth's surface at visible and infrared wavelengths |
| L-band | a radar operated within the interval of wavelengths from 19.3 to 76.9 cm and frequencies from 0.39 to 1.55 GHz |

| | |
|---|---|
| lead | fracture through sea ice that is navigable by surface vessels |
| loess | blanket deposit of wind-blown silt |
| look angle (radar) | angle between the vertical plane and the line that links an imaging-radar antenna to a feature on the ground |
| Mbits/s | megabits per second, used to describe rate of transmission of digital data |
| metamorphic rock | rock altered from an original condition by elevated temperature and/or pressure that produces a change of texture and mineralogy |
| metasedimentary | evidence of metamorphism, as applied to sedimentary rocks |
| microwave | any electromagnetic wave having a wavelength in the interval between one millimeter and one meter |
| migmatite | rock composed of igneous and metamorphic materials |
| MSS | multispectral scanner; a Landsat imaging system that scans a scene in four bands simultaneously |
| muscovite | mineral in the mica group |
| nadir | point or track on the ground vertically beneath an orbiter |
| NOAA | National Oceanic and Atmospheric Administration |
| node (orbit) | point at which an orbiter crosses Earth's equatorial plane on an ascending orbit |
| ophiolite | an assemblage of basic and ultrabasic igneous rocks |
| orthoquartzite | quartzite of sedimentary origin |
| pahoehoe | basaltic lava flow with smooth, ropy surfaces |
| pediment | broad erosion surface at the base of a mountain front |
| pillow (basalt) | structure characterized by discontinuous pillow-shaped masses, considered to be the product of subaqueous volcanism |
| polarization | vibration direction of electrical field in electromagnetic radiation; polarization is parallel in SAR systems when transmit and receive directions are the same |
| polynya | area of open water surrounded by sea ice |
| pumice | volcanic rock, light colored, cellular to glassy |
| pyroclastic | formed by the accumulation of fragments scattered by volcanic explosions |
| radar | radio detection and ranging; radar is used in remote sensing for measuring and mapping the Earth and planetary surfaces |
| range (radar imaging) | across-track direction of image acquisition |
| repeat cycle (of an orbit) | time required for orbiter to return to a previously occupied position relative to Earth |
| resolution (spatial) | the minimum distance between two adjacent features on the ground, or the minimum size of a feature on the ground, that can be detected by an imaging system |
| returns (radar) | backscatter (qv) |
| rhyolitic | typically composed of quartz and alkali feldspar in a glassy groundmass, as applied to volcanic rocks |
| Riedel-Shear | shear planes formed at an acute angle to the line of differential movement |
| SAR | synthetic-aperture radar (qv) |
| scarp | cliff or steep slope of some extent that may form a marked topographic boundary |

| | |
|---|---|
| scene | area covered by SAR, MSS, TM or photographic image |
| schist | metamorphic rock showing strong foliation |
| Seasat | an Earth-orbiting satellite equipped with five instruments, including a side-looking synthetic-aperture imaging radar system, for studying ocean dynamics |
| sedimentary rock | rock formed from the accumulation of particles of preexisting rock, or from chemical or biochemical precipitation |
| seif | large, tapering, sharp-crested longitudinal dune |
| seismic | relating to an earthquake or earth vibration |
| sericite | white mica occurring as alteration product in various metamorphic rocks |
| shadow (radar) | an area of no radar backscatter on an image caused by an obstruction that blocks the illuminating radar beam |
| signature (radar) | characteristics and patterns of objects that permit recognition of the objects on radar images |
| sinkhole | funnel-shaped depression, usually in a limestone region, that connects to a subterranean passage formed by solution |
| SIR-A | Shuttle Imaging Radar experiment flown on Space Shuttle Columbia in November 1981 |
| SIR-B | Shuttle Imaging Radar experiment flown on Space Shuttle Challenger in October 1984. |
| specular (reflections) | mirror-like returns of a radar signal |
| stratovolcano | cone composed of alternating layers of lava and pyroclastic materials, generally large and steep sided |
| strike | bearing of an inclined bed or structure on a level surface |
| strike-slip fault | fault in which the movement of the rocks on each side of the fault plane is predominantly horizontal. The displacement is either left-lateral or right-lateral depending on the direction of movement of the far block as viewed from either side of the fault |
| subduction | a large-scale crustal process where one lithospheric plate descends beneath another |
| suture | boundary zone, denoting margin of former crustal plates |
| syncline | folded-rock structure whose limbs dip toward the fold axis |
| synthetic-aperture radar | a side-looking airborne or spaceborne imaging system that uses the Doppler principle to sharpen the effective beamwidth of the antenna |
| tectonic | relating to major structural and deformational features of the Earth's crust |
| thermocline | a region of rapid temperature change in a body of thermally stratified water |
| thrust fault | low-angle dip-slip fault in which the block above the fault plane moves up and over the lower block |
| till | unstratified sediment deposited directly by a glacier |
| TM | thematic mapper; a Landsat imaging system that scans a scene in seven bands simultaneously, with higher spatial and spectral resolution than the Landsat MSS |
| transform fault | a plate boundary along which strike-slip motion occurs, usually offsetting segments of a spreading ridge |
| trellis (drainage) | surface pattern of parallel main streams with right-angle tributaries that are fed by secondary tributaries that parallel the main streams |
| tuff | rock formed of compacted volcanic fragments generally less than 4 mm in diameter |

| | |
|---|---|
| ultrabasic | containing less than 45% silica, as applied to igneous rocks |
| volcanic rock | igneous rock formed by uption at the Earth's surface |
| wadi | dry stream channel, common in arid lands in North Africa and Asia Minor |
| wave energy spectra | mean wave energy per unit area |

# Appendix B
# Index of Images

2 FOLDOUT FRAME

| Scene No. | SIR-B Image | Date, Oct. 1984 | Data Take; Scene No. | Center Incidence Angle, deg. | Center Coordinates | | Corresponding Coverage | Date | Reference ID | Center Incidence Angle, deg (SAR) | Sun Angle (Landsat) | |
|---|---|---|---|---|---|---|---|---|---|---|---|---|
| | | | | | Latitude | Longitude | | | | | Elevation, deg | Azimuth, deg |
| 1 | Interior Plateau, Central Kalimantan, Indonesia | 11 | 94.4; 026 | 41.4 | 0°37′N | 114°55′E | Sketch map | – | – | – | – | – |
| 2 | Dead Sea Rift Zone, Southern Israel | 8 | 43.2; 022 | 34.3 | 31°07′N | 35°19′E | Sketch map | – | – | – | – | – |
| 3 | Central Andean Cordillera, Northern Peru | 7 | 39.6; 006 | 54.4 | 4°54′S | 78°20′W | Sketch map | – | – | – | – | – |
| 4 | Precambrian Fold Mountains, Brazil and Colombia | 12 | 118.3; 084 | 35.5 | 1°59′N | 68°10′W | Sketch map | – | – | – | – | – |
| 5 | Amadeus Basin, Northern Territory, Australia | 10 | 84.6; 005 | 36.0 | 24°15′S | 134°30′E | Sketch map | – | – | – | – | – |
| 6 | Pasir Mountains and Coastal Lowlands, East Kalimantan, Indonesia | 11 | 94.4; 008 | 41.8 | 1°28′S | 116°06′E | Landsat MSS | Oct. 25, 1984 | ILS/LAPAN 5023801580-7 | – | – | – |
| 7 | Late Precambrian Suture Line, Northeast Sudan | 11 | 97.5; 009 | 52.1 | 22°07′N | 35°08′E | Landsat TM | Nov. 18, 1984 | 50262-07373, band 4 | – | 41 | 144 |
| 8 | Upper Rajang Region, Central Sarawak, Malaysia | 11 | 94.4; 001 | 41.8 | 2°43′N | 113°43′E | Sketch map | – | – | – | – | – |
| 9 | Kilauea Volcano, Hawaii, U.S.A. | 11<br>12 | 99.2; 006, 007<br>115.2; 001, 002 | 28.1<br>48.0 | 19°10′N | 155°22′W | SIR-B color composite | – | – | – | – | – |
| 10 | Mount Shasta, California, U.S.A. | 10<br>8<br>7 | 87.4; 002<br>55.4; 004<br>39.4; 001, 002 | 29.7<br>53.8<br>63.8 | 41°50′N | 122°25′W | Digital elevation model;<br>Computer-generated perspective views | –<br>– | –<br>– | –<br>– | –<br>– | –<br>– |
| 11 | Charlevoix Crater, Province of Quebec, Canada | 12 | 116.2; 002, 003 | 49.9 | 47°29′N | 70°15′W | Sketch map | – | – | – | – | – |
| 12 | Altiplano, Bolivia | 7 | 39.6; 016 | 54 | 21°00′S | 68°00′W | STS 41-G Hasselblad photograph | Oct. 5, 1984 | Roll 35, frame 24 | – | – | – |
| 13 | Tuwaiq Escarpment, Central Saudi Arabia | 11 | 105.4; 002 | 34.4 | 23°45′N | 46°45′E | Sketch map | – | – | – | – | – |
| 14 | Spring Mountains and Pahrump Valley, Nevada, U.S.A. | 10 | 87.4; 009 | 30.3 | 36°07′N | 115°51′W | Sketch map | – | – | – | – | – |
| 15 | Wind-Eroded Sandstones, Borkow Province, Northern Chad | 12 | 107.2; 006 | 52.3 | 18°29′N | 19°05′E | Sketch map | – | – | – | – | – |
| 16 | Gebel Mufta, Western Desert, Southwest Egypt | 11 | 91.2; 006 | 28.4 | 24°55′N | 26°30′E | SIR-B | Oct. 12, 1984 | DT 113.3; 039 | 42.9 | – | – |

FOLDOUT FRAME

PRECEDING PAGE BLANK NOT FILMED

| Scene No. | SIR-B Image | Date, Oct. 1984 | Data Take; Scene No. | Center Incidence Angle, deg. | Center Coordinates | | Corresponding Coverage | Date | Reference ID | Center Incidence Angle, deg (SAR) | Sun Angle (Landsat) | |
|---|---|---|---|---|---|---|---|---|---|---|---|---|
| | | | | | Latitude | Longitude | | | | | Elevation, deg | Azimuth, deg |
| 17 | Hexi Corridor, Gansu Province, China | 12 | 120.2; 021 | 25.8 | 37°37′N | 102°51′E | Sketch map | – | – | – | – | – |
| 18 | Rio Japurá, Amazonas, Brazil | 12 | 118.3; 001 | 35.5 | 1°40′S | 66°10′W | SIR-A | Nov. 13, 1981 | DT 24C | 47 | – | – |
| 19 | Sundarbans Mangrove Forest, Bangladesh | 11 | 104.2; 002 | 45.6 | 22°12′N | 89°54′E | Sketch map | – | – | – | – | – |
| 20 | Mangrove Swamp, Exmouth Gulf, Western Australia | 7 | 37.6; 033, 034 | 30.4 | 22°22′S | 114°26′E | Sketch map | – | – | – | – | – |
| 21 | Río Cisnés, Cordillera Patagónica Central, Chile | 11 | 92.8; 008, 009 | 31.4 | 44°36′S | 71°32′W | Landsat TM; | Dec. 26, 1984 | 50300-13544-1 | – | 49 | 72 |
| | | 10 | 76.8; 001 | 43.3 | | | Insets from SIR-B images | – | – | – | – | – |
| 22 | Michinmahúida Volcano, Chiloé Province, Chile | 9 | 72.4; 012, 013 | 45.2 | 42°43′S | 72°32′W | SIR-B | Oct. 10, 1984 | DT 88.4; 014, 013 | 53.7 | – | – |
| 23 | Albemarle Sound, North Carolina, U.S.A. | 11 | 96.21; 017 | 21.6 | 36°06′N | 76°28′W | Sketch map | – | – | – | – | – |
| 24 | Ocean Pond, Florida, U.S.A. | 9 | 64.2; 014 | 58.2 | 30°10′N | 82°21′W | SIR-B color composite | – | – | – | – | – |
| | | 10 | 80.2; 003 | 45.3 | | | | | | | | |
| | | 11 | 96.2; 003 | 28.4 | | | | | | | | |
| 25 | Shillong Plateau, India, and Sylhet Uplands and Lowlands, Bangladesh | 12 | 120.2; 011 | 25.8 | 24°59′N | 91°57′E | Sketch map | – | – | – | – | – |
| 26 | Cordón la Grasa, Chubut Province, Argentina | 11 | 104.4; 006 | 59.4 | 43°18′S | 71°36′W | SIR-B color composite; | – | – | – | – | – |
| | | 10 | 88.4; 008 | 53.7 | | | Vegetation map | – | – | – | – | – |
| | | 9 | 72.4; 001 | 44.7 | | | | | | | | |
| | | 8 | 56.4; 010, 009 | 33.0 | | | | | | | | |
| 27 | Gravel Terrace and Alluvial Plain, Chubut Province, Argentina | 11 | 92.8; 003 | 31.6 | 43°18′S | 69°22′W | Ground photographs | – | – | – | – | – |
| 28 | Agricultural Development, Sumatra, Indonesia | 12 | 118.6; 014 | 52.2 | 1°28′S | 102°04′E | Lansat MSS | Feb. 4, 1985 | 5039702540-7 | – | – | – |
| 29 | Macomb, Illinois, U.S.A. | 11 | 97.2; 003 | 31.4 | 40°30′N | 90°41′N | Airborne SAR; | Oct. 10, 1984 | JPL 841010 | ~44 | – | – |
| | | | | | | | Landsat TM; | Oct. 29, 1984 | 50242-16114-4 | – | 31 | 53 |
| | | | | | | | Sketch map | – | – | – | – | – |
| 30 | Montreal, Province of Quebec, Canada | 7 | 37.2; 003 | 33.4 | 45°25′N | 73°29′W | Airborne SAR image | Oct. 25, 1985 | Canada Center for Remote Sensing | – | – | – |

FOLDOUT FRAME

2 FOLDOUT FRAME

| Scene No. | SIR–B Image | Date, Oct. 1984 | Data Take; Scene No. | Center Incidence Angle, deg. | Center Coordinates | | Corresponding Coverage | Date | Reference ID | Center Incidence Angle, deg (SAR) | Sun Angle (Landsat) | |
|---|---|---|---|---|---|---|---|---|---|---|---|---|
| | | | | | Latitude | Longitude | | | | | Elevation, deg | Azimuth, deg |
| 31 | Nagoya Industrial District, Central Honshu, Japan | 10 | 76.6; 005 | 21.1 | 34°53′N | 136°57′E | Landsat TM band 3; Aerial photograph | Oct. 1, 1984 | 50214-00584-3 | – | 43 | 142 |
| 32 | Northern Shikoku and Seto Inland Sea, Japan | 7 | 39.2; 007 | 46.7 | 34°08′N | 133°44′E | Landsat TM band 5; Landsat TM band 5; Aerial photographs | May 8, 1984 May 8, 1984 | 50068-01081-5 50068-01084-5 | – – | 59 59 | 117 114 |
| 33 | Surface Waves Off Chile, South America | 11 | 91.5; 002 | 25.1 | 55°30′S | 82°30′W | Diagrams | – | – | – | – | – |
| 34 | Hurricane Josephine, North Atlantic | 12 | 117.4; 001 –008 | 24.6 | 35°25′N to 32°14′N | 72°05′W to 68°57′W | Sketch map | – | – | – | – | – |
| 35 | Surface Waves at Different Aspect Angles, North Atlantic | 11 | 94.2; 006 | 26.3 | 46°32′N | 18°26′W | SIR–B | Oct. 11, 1984 | DT 98.3; 001 | 24.8 | – | – |
| 36 | Internal Waves, New York Bight, U.S.A. | 11 | 96.21; 021 | 20.6 | 39°59′N | 72°15′W | Diagrams | – | – | – | – | – |
| 37 | Small-Scale Eddies Off Long Island, New York, U.S.A. | 11 | 96.21; 024 | 20.4 | 40°47′N | 71°16′W | STS 41-G Hasselblad photograph | Oct. 6, 1984 | Roll 41, frame 45 | – | – | – |
| 38 | Shoals Off Martha's Vineyard, Massachusetts, U.S.A. | 11 | 96.21; 019 | 19.8 | 41°25′N | 70°27′W | Diagram from bathymetric charts 0808 N and 0708N, Dept. of Commerce | – | – | – | – | – |
| 39 | Pack Ice, Weddell Sea, Southern Ocean | 9 | 70.4; 005 | 25.3 | 58°01′S | 14°44′E | NOAA-6, AVHRR GMT283:22:46:15 | Oct. 9, 1984 | Rev. 27482 | – | – | – |
| 40 | Marginal Ice Zone, Weddell-Scotia Seas, Southern Ocean | 11 | 104.5; 005 | 24.1 | 56°00′S | 27°35′W | SIR–B enlargement; Diagram | – – | – – | – – | – – | – – |